Title

Variable Angle Correlation Spectroscopy

Author

Lee, Y K

Publication Date

1994-05-01

LBL-37826
UC-404

Lawrence Berkeley Laboratory
UNIVERSITY OF CALIFORNIA

Materials Sciences Division

Variable Angle Correlation Spectroscopy

Y.K. Lee
(Ph.D. Thesis)

May 1994

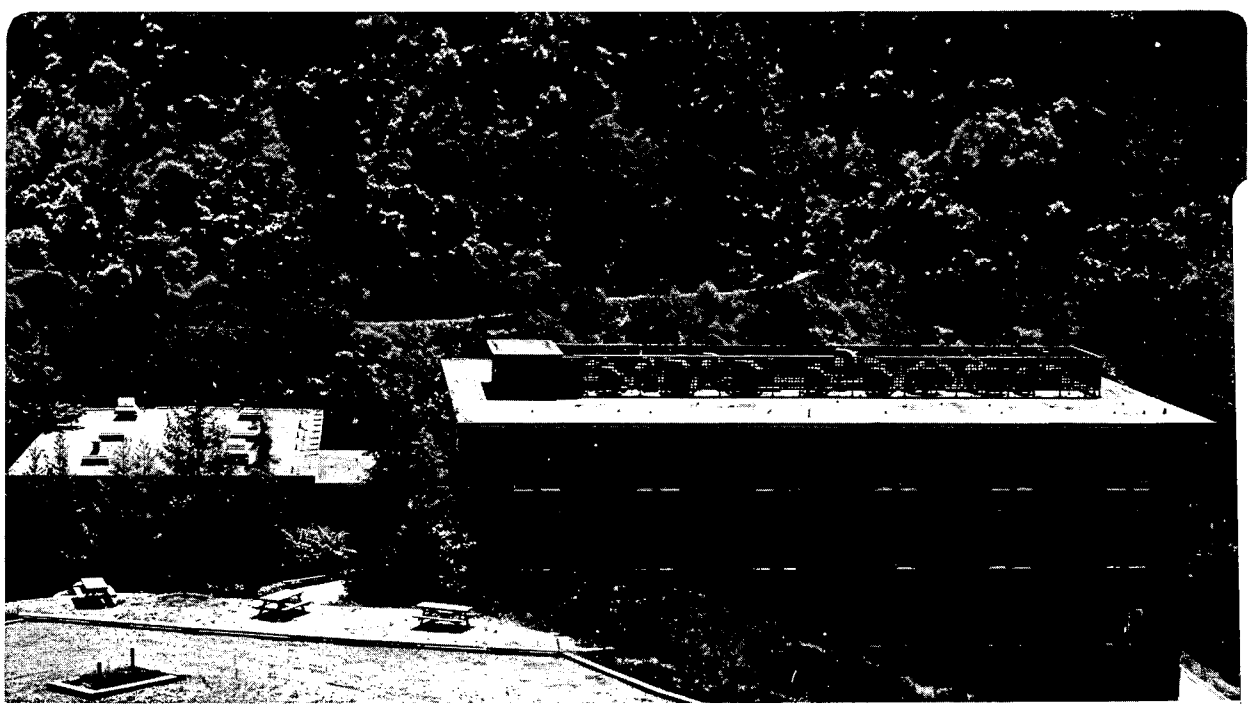

Prepared for the U.S. Department of Energy under Contract Number DE-AC03-76SF00098

DISCLAIMER

Variable Angle Correlation Spectroscopy

Young Kyo Lee

Graduate Group in Biophysics
University of California

and

Chemical Biodynamics Division
Lawrence Berkeley Laboratory
University of California
Berkeley, California 94702

May 1994

This work was supported by the Director, Office of Health and Environmental Research, Health Effects Research Division, of the U.S. Department of Energy under Contract No. DE-AC03-76SF00098.

Variable Angle Correlation Spectroscopy

by

Young Kyo Lee

Abstract

Variable Angle Correlation Spectroscopy

by

Young K. Lee

In this dissertation, a novel nuclear magnetic resonance (NMR) technique, variable angle correlation spectroscopy (VACSY) is described and demonstrated with ^{13}C nuclei in rapidly rotating samples. These experiments focus on one of the basic problems in solid state NMR: how to extract the wealth of information contained in the anisotropic component of the NMR signal while still maintaining spectral resolution. Analysis of the anisotropic spectral patterns from poly-crystalline systems reveal information concerning molecular structure and dynamics, yet in all but the simplest of systems, the overlap of spectral patterns from chemically distinct sites renders the spectral analysis difficult if not impossible. One solution to this problem is to perform multi-dimensional experiments where the high-resolution, isotropic spectrum in one dimension is correlated with the anisotropic spectral patterns in the other dimensions. The VACSY technique incorporates the angle between the spinner axis and the static magnetic field as an experimental parameter that may be incremented during the course of the experiment to help correlate the isotropic and anisotropic components of the spectrum.

The two-dimensional version of the VACSY experiments is used to extract the chemical shift anisotropy tensor values from multi-site organic molecules, study molecular dynamics in the intermediate time regime, and to examine the ordering properties of partially oriented samples. The VACSY technique is then extended to three-dimensional experiments to study slow molecular reorientations in a multi-site polymer system.

Table of Contents

List of Figures

List of Tables

Acknowledgments

There are few places in the world quite like the Alex Pines' lab—a dynamic environment with a broad spectrum of people and ideas, where we had the freedom to pursue our own goals and what seemed like unlimited resources to make these goals realities. It has been a joy and a privilege to have been associated with all the different people who have come through the lab the past five years and enriched my graduate school experience and left lasting impressions on me. I apologize for mentioning only a small handful of these people.

First special thanks must be given to Margaret Eastman and Phil Grandinetti for nurturing me during my early days in the lab and to Gerry Chingas who took my initial fascination with the exploding AR 100LP as a cue to introduce me to the strange mysteries of rf design. The work presented in this thesis would not have been possible without the brilliant insights of Lucio Frydman who initially visualized the possibility of the variable angle correlation technique and made critical contributions to every aspect of this project. Lyndon Emsley, Russ Larsen, Klaus Schmidt-Rohr, Mei Hong and Gerry Chingas also played key roles in the successful completion of the experiments in this dissertation. Yung-Ya Lin and Professors Bob Vold and Gina Hoatson were particularly helpful in developing the linear prediction methods discussed in chapter 3. Our work could not have been possible without ingenious craftsmen in the chemistry machine shop who, with their keen sense of aesthetics and attention to detail, took our abstract ideas and less-than-perfect drawings and turned them into the precision hardware that made our experiments successful.

I would like to thank Mary Pagel, Kelly Richards and a host of other two-wheeled friends for the memories of the surreal moon-light century through the deserts of southern Utah, the tests of endurance in Davis, and all the other wonderful rides through the hills

and valleys surrounding Berkeley. Special thanks must also be given to Geoff Barral who—whether battling the twisted logic of a certain commercial spectrometer, struggling up the 30% plus grades of Diablo, or trekking through canyons of the high-Sierras on our non-fishing backpacking trips—was a great friend and companion. I would also like to thank Joe Sachleben who, despite his constant complaints, I think actually enjoyed most of the adventures we shared together.

I had the good fortune of having two advisors during my stay at Berkeley. I would like to thank professor David Wemmer for his support, guidance and encouragement to pursue my scientific interests. I would like to thank professor Alex Pines for instilling into the lab his own sense of enthusiasm, love of science, and excitement that could make any student drop everything for the pursuit of "impossible" problems. And of course I cannot forget Dione Carmichael who, with her flare for philosophy, knowledge of history, and her very unique and keen insight into human nature and perhaps the plight of humanity in general, provided countless hours of fascinating and entertaining conversations.

Finally, I would like to thank my parents and my sister for their support and encouragement over the years.

Chapter 1. Background Theory

I will discuss in this chapter some of the basic principles of Fourier and NMR theory that will be used throughout this thesis.

1.1 Fourier Transformation and Theorems

Since its first introduction into NMR[1] and development of its possible applications,[2] the Fourier transformation has become the basis of modern NMR spectroscopy and imaging. Since much of this thesis is concerned with the generalizations of the Fourier transformation and uses of Fourier theorems in developing novel NMR techniques, I will first briefly review some of these theorems.

The Fourier transform of $f(x)$ is defined as

$$\int_{-\infty}^{\infty} f(x)e^{-ixy}dx. \tag{1.1}$$

To note the reversibility of Eq. 1.1, the transformation equations are usually written in pairs. In n dimensions, the Fourier transform pairs are:

$$\begin{aligned} F(\mathbf{y}) &= \int_{-\infty}^{\infty} f(\mathbf{x})e^{-i\mathbf{x}\cdot\mathbf{y}}d\mathbf{x} \\ f(\mathbf{x}) &= \frac{1}{(2\pi)^n}\int_{-\infty}^{\infty} F(\mathbf{y})e^{-i\mathbf{x}\cdot\mathbf{y}}d\mathbf{y}, \end{aligned} \tag{1.2}$$

where the vectors $\mathbf{x}$ and $\mathbf{y}$ are both n dimensional vectors and define the conjugate Fourier spaces. Generally in NMR spectroscopy, the Fourier vectors $\mathbf{x}$ and $\mathbf{y}$ are represented by

the frequency and time vectors, $\bar{\omega}$ and $\bar{t}$, and by having the time domain signal and the spectrum form the Fourier transform pair, all of the mathematical properties and theorems associated with the Fourier transformation may be used to extract precisely the information desired from the experimental data. In the following, $f(\mathbf{x})$ and $F(\mathbf{y})$ are a Fourier transform pair obeying Eq. 1.2.

The similarity theorem

If the Fourier variable x is scaled by a constant factor a then $f(ax)$ will have the Fourier transform $|a|^{-1}F(y/a)$:

$$\begin{aligned}\int_{-\infty}^{\infty} f(ax)e^{-ixy}dx &= \frac{1}{|a|}\int_{-\infty}^{\infty} f(ax)e^{i(ax)(y/a)}d(ax) \\ &= \frac{1}{|a|}F(y/a).\end{aligned} \tag{1.3}$$

Generalized to higher dimensions, Eq. 1.3 becomes

$$f(\mathbf{Ax}) = \frac{1}{|\mathbf{A}|}F(\mathbf{y}^{\mathrm{T}}\mathbf{A}^{-1}), \tag{1.4}$$

where **A** is a matrix that creates a general transformation of the vector **x**, "T" represents transpose, and $|\mathbf{A}|$ is the determinant of the matrix. For the special case of orthogonal transformations,

$$|\mathbf{A}| = 1 \quad \text{and} \quad \mathbf{A}^{-1} = \mathbf{A}^{\mathrm{T}}. \tag{1.5}$$

This leads to the important conclusion that if the coordinates of one Fourier space are rotated,

$$\mathbf{x}' = \mathbf{A} \cdot \mathbf{x}, \tag{1.6}$$

the conjugate Fourier space coordinates are rotated in the identical manner:

$$\mathbf{y}' = \mathbf{A} \cdot \mathbf{y}. \tag{1.7}$$

The shift theorem

Displacements in one Fourier dimension correspond to phase shifts in the conjugate dimension:

$$\begin{aligned} \int_{-\infty}^{\infty} f(x-a)e^{-ixy}dx &= \int_{-\infty}^{\infty} f(x-a)e^{-i(x-a)y}e^{-iay}d(x-a) \\ &= e^{-iay}F(y). \end{aligned} \tag{1.8}$$

Equation 1.8 easily generalizes to higher dimensions as

$$f(\mathbf{x}-\mathbf{a}) = e^{-i\mathbf{a}\cdot\mathbf{y}}F(\mathbf{y}). \tag{1.9}$$

The shift theorem is most commonly applied as first order phase correction to NMR spectra.

The convolution theorem

Given that $g(x)$ and $G(y)$ also form a Fourier transform pair, the convolution

theorem states:

$$f(x)*g(x) = F(y)G(y), \tag{1.10}$$

where the convolution of f(x) and g(x) is defined by the integral

$$f(x)*g(x) = \int_{-\infty}^{\infty} f(x')g(x-x')dx'. \tag{1.11}$$

This can be seen by Fourier transforming the right hand side of Eq. 1.11:

$$\begin{aligned} &\int_{-\infty}^{\infty}\left[\int_{-\infty}^{\infty} f(x')g(x-x')dx'\right]e^{-ixy}dx \\ &\qquad = \int_{-\infty}^{\infty} f(x')\left[\int_{-\infty}^{\infty} g(x-x')e^{-ixy}dx\right]dx'. \end{aligned} \tag{1.12}$$

Then using the shift theorem (Eq. 1.3), the integral becomes

$$\int_{-\infty}^{\infty} f(x')G(y)e^{-ix'y}dx' = F(y)G(y). \tag{1.13}$$

Equation 1.13 may easily be generalized to higher dimensions by defining a multi-dimensional convolution:

$$\begin{aligned} f(\mathbf{x})*g(\mathbf{x}) &= \int_{-\infty}^{\infty} f(\mathbf{x}')g(\mathbf{x}-\mathbf{x}')d\mathbf{x}' \\ &= F(\mathbf{y})G(\mathbf{y}). \end{aligned} \tag{1.14}$$

Projection slice theorem

Given that $f(\mathbf{x})$ and $F(\mathbf{y})$ form a 2D Fourier transform pair, the Fourier transformation of a cross sectional slice in one Fourier space is equal to the projection onto an axis of the same orientation in the conjugate Fourier space. First consider a projection of a 2D function $f(x_1, x_2)$ onto the x_1 axis:

$$p_{x_1}(x_2) = \int_{-\infty}^{\infty} f(x_1, x_2) dx_1 . \tag{1.15}$$

Its Fourier transformation then becomes the slice of $F(y_1, y_2)$ at $y_1 = 0$:

$$\begin{aligned} P_{x_1}(y_2) &= \int_{-\infty}^{\infty} p_{x_1}(x_2) e^{-ix_2 y_2} dx_2 \\ &= \int_{-\infty}^{\infty}\int_{-\infty}^{\infty} f(x_1, x_2) e^{-ix_2 y_2} dx_1 dx_2 \\ &= F(y_1, y_2)\big|_{y_1 = 0}. \end{aligned} \tag{1.16}$$

The result of Eq. 1.16 may be generalized to projections onto an axis of arbitrary orientation by considering the same equations for a new set of coordinates,

$$\begin{aligned} \mathbf{x}' &= \mathbf{A}\mathbf{x} \\ \mathbf{y}' &= \mathbf{A}\mathbf{y}, \end{aligned} \tag{1.17}$$

where

$$\mathbf{A} = \begin{bmatrix} \cos\theta & \sin\theta \\ -\sin\theta & \cos\theta \end{bmatrix}. \tag{1.18}$$

The theorem may then be quickly generalized to higher dimensions by writing **x'**, **y'** as n dimensional vectors and **A** as an $n \times n$ orthogonal rotation matrix.

1.2 Classical Theory of NMR

All the experiments discussed in this thesis have been performed on isolated spin $\frac{1}{2}$ systems and may be described purely by classical means. Thus I will only discuss the classical theory of spin evolution; the complete quantum mechanical description of NMR may be found in several books[3-5].

The equation of motion describing a classical spin system is given by the phenomenological Bloch equation:

$$\frac{d\mathbf{M}}{dt} = \gamma_n \mathbf{M} \times \mathbf{B}, \tag{1.19}$$

where **M** is the macroscopic magnetization vector due to the alignment of the nuclear spins, γ_n is the nuclear gyromagnetic ratio, and **B** is the magnetic field.

Equation 1.19 may be more conveniently expressed in a rotating coordinate system. Such a transformation can be understood by considering infinitesimal changes in the magnetization vector. The change in the magnetization vector as seen from the laboratory frame, $(d\mathbf{M})_L$, is due to the change in the magnetization seen from the rotating frame, $(d\mathbf{M})_R$, plus the change in the magnetization due to the rotation of the coordinate system $(d\mathbf{M})_{RCS}$.

$$(d\mathbf{M})_L = (d\mathbf{M})_R + (d\mathbf{M})_{RCS}. \tag{1.20}$$

The last term in Eq. 1.20 can be simply expressed as[6]

$$(d\mathbf{M})_{RCS} = d\varphi\hat{\mathbf{n}} \times \mathbf{M}, \tag{1.21}$$

where $\hat{\mathbf{n}}$ is the direction of the rotation axis, and $d\varphi$ is the infinitesimal change in the angle due to the rotation of the coordinate system. Equation 1.20 may then be written in terms of time derivatives as

$$\left(\frac{d\mathbf{M}}{dt}\right)_L = \left(\frac{d\mathbf{M}}{dt}\right)_R + \vec{\omega}_{RCS} \times \mathbf{M}, \tag{1.22}$$

where $\vec{\omega}_{RCS}$ is the frequency vector of the rotating coordinate system. Substituting Eq. 1.19 for the left hand side, we obtain

$$\left(\frac{d\mathbf{M}}{dt}\right)_R = \mathbf{M} \times \left(\gamma_n \mathbf{B} + \vec{\omega}_{RCS}\right). \tag{1.23}$$

The magnetization, evolves under the influence of main static magnetic field, $\mathbf{B_0}$, and a smaller field $\mathbf{B}_{Int}$ due to local interactions. Equation 1.23 then becomes

$$\left(\frac{d\mathbf{M}}{dt}\right)_R = \mathbf{M} \times \left(-\vec{\omega}_0 - \vec{\omega}_{Int} + \vec{\omega}_{RCS}\right), \tag{1.24}$$

where $\vec{\omega}_0 = -\gamma_n \mathbf{B_0}$ (the Larmor frequency) and $\vec{\omega}_{Int} = -\gamma_n \mathbf{B}_{Int}$. When $\vec{\omega}_{RCS} = \vec{\omega}_0$, the Larmor frequency cancels and Eq. 1.23 becomes

$$\left(\frac{d\mathbf{M}}{dt}\right)_R = \vec{\omega}_{Int} \times \mathbf{M}. \tag{1.25}$$

In NMR experiments, the rf signal is generally mixed down to audio frequencies before it is detected, which corresponds to recording of the signal in the rotating frame. In addition,

since the information desired from the experiment is contained in $\vec{\omega}_{Int}$, from both the experimental and theoretical viewpoint, it is more convenient to discuss the NMR signal in the rotating frame. For the rest of the thesis, evolution in the rotating frame at the Larmor frequency will be assumed and all subscripts will be dropped.

The equation of motion takes on a simple form for magnetization transverse to a constant magnetic field. For $\vec{\omega} = (0,0,\omega)$ and $\mathbf{M}(t) = (M_0,0,0)$ Eq. 1.25 becomes

$$\begin{aligned} \dot{M}_x &= \omega M_y \\ \dot{M}_y &= \omega M_x. \end{aligned} \tag{1.26}$$

which may be readily solved as

$$\begin{aligned} M_x(t) &= M_0 \cos(\omega t) \\ M_y(t) &= -M_0 \sin(\omega t). \end{aligned} \tag{1.27}$$

Since quadrature detection records both the M_x and M_y components of the magnetization, it is convenient to superimpose the two components onto a complex plane and define

$$M_+(t) = M_x(t) + iM_y(t). \tag{1.28}$$

Then the signal or free induction decay (FID) of the magnetization evolving with a single frequency becomes

$$S(t) = M_0 \exp[-i\omega t], \tag{1.29}$$

In NMR we are not usually dealing with single isochromats but rather systems evolving with a distribution of frequencies. The key relationship of the NMR signal and the spectrum through a Fourier transformation is due to the fact that a spin system may be

considered a linear system where the signal from each isochromat may be added to form the total signal.

For a frequency distribution $I(\omega)$, Eq. 1.29 for the NMR signal becomes

$$S(t) = \int_{-\infty}^{\infty} I(\omega)\exp[-i\omega t]d\omega, \tag{1.30}$$

which may be inverted to obtain

$$I(\omega) = \frac{1}{2\pi}\int_{-\infty}^{\infty} S(t)\exp[i\omega t]dt; \tag{1.31}$$

thus $S(t)$ and $I(\omega)$ form a Fourier transform pair.

1.3 NMR Hamiltonians

The physical origin of the interaction frequency introduced in the previous section is the NMR Hamiltonian which has the general structure:

$$\begin{aligned} \mathrm{H} &= C\mathbf{I}\cdot\mathbf{R}\cdot\mathbf{S} \\ &= C\sum_{i,j=1}^{3} I_i R_{ij} S_j \,, \end{aligned} \tag{1.32}$$

where **I** and **S** are two vectors coupled to each other by a second rank tensor, **R**, and the coupling constant, C, is determined by the physical origin of the Hamiltonian. The vector **I** represents the nuclear spin vector; **S** may represent the same nuclear vector (quadrupole interaction), another nuclear vector (J and dipole coupling), or a static field (chemical shift). The same Hamiltonian may also be written as a product of two second rank Cartesian tensors

$$\mathrm{H} = \sum_{i,j=1}^{3} C R_{ij} T_{ij}, \tag{1.33}$$

where T_{ij} is a dyad product of the vectors **I** and **S**,[7] or in terms of irreducible spherical tensors[8]

$$\mathrm{H} = C \sum_{l=0,2} \sum_{m=-l}^{l} (-1)^m R_{l-m} T_{lm}. \tag{1.34}$$

1.3.1 Coordinate Rotations

The Cartesian tensor **R** represents the physical interaction that couples the two vectors. The coupling tensor has its simplest form in the principle axis system (PAS) frame where **R** becomes diagonal[4]

$$\mathbf{R}_{\mathrm{PAS}} = \begin{bmatrix} R_{xx} & & \\ & R_{yy} & \\ & & R_{zz} \end{bmatrix}. \tag{1.35}$$

The components of the tensor in Eq. 1.35 are labeled with the convention

$$|R_{zz} - R| \geq |R_{xx} - R| \geq |R_{yy} - R|, \tag{1.36}$$

where $R = \frac{1}{3}\mathrm{Tr}\,\mathbf{R}$. The interaction tensor in an arbitrary frame can be obtained through orthogonal coordinate transformations

$$\mathbf{R}' = \mathbf{D}(\Omega)\mathbf{R}_{\mathrm{PAS}}\mathbf{D}(\Omega)^{\mathrm{T}}, \tag{1.37}$$

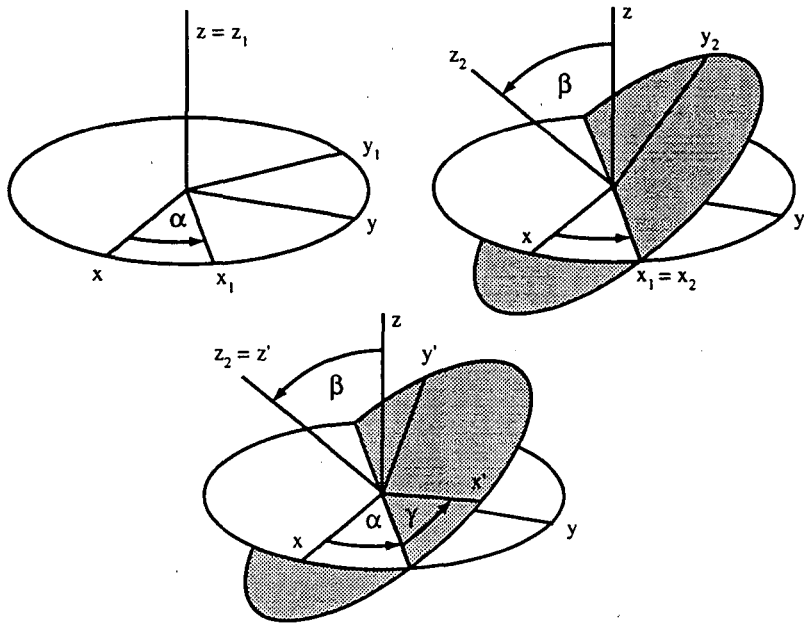

Figure 1.1. Euler angle rotations in transforming from the (x,y,z) coordinate axes system to the (x', y', z') coordinates. The sequence of rotations starts with a rotation of angle α about the z axis, transforming the system in to a set of intermediate coordinates (x_1, y_1, z_1). Next the system rotates through the angle β about the x_1 axis into the second intermediate coordinates (x_2, y_2, z_2). Finally, a rotation of angle γ about the z_2 axis completes the transformation into the (x', y', z') coordinate axes system.

where $\mathbf{D}(\Omega)$ orthogonal rotation matrices and Ω represents the set of Euler angles α, β, and γ (Fig. 1.1). Likewise the spherical tensor R_{lm} also takes on a simple form in the PAS frame with only the $m = 0, \pm 2$ terms being nonzero. The tensor components R_{lm} in the PAS frame are usually represented by ρ_{lm} and are related to the Cartesian tensor components by

$$\begin{aligned} \rho_{00} &= \tfrac{1}{3}\left(R_{xx} + R_{yy} + R_{zz}\right) = R \\ \rho_{20} &= \sqrt{\tfrac{3}{2}}\left(R_{zz} - R\right) = \sqrt{\tfrac{3}{2}}\delta \\ \rho_{2\pm2} &= \tfrac{1}{2}\left(R_{yy} - R_{xx}\right) = \tfrac{1}{2}\eta\delta. \end{aligned} \tag{1.38}$$

For spherical tensors, coordinate rotation from the PAS frame to an arbitrary frame is obtained by Wigner rotation matrices

$$R_{lm} = \sum_{m=-l}^{l} D^{l}_{m'm}(\Omega)\rho_{lm'}$$
$$D^{l}_{m'm}(\Omega) = e^{-im'\alpha} d^{l}_{m'm}(\beta) e^{-im\gamma}, \tag{1.39}$$

The reduced Wigner rotation matrix elements, $d^{l}_{m'm}(\beta)$, are tabulated in several books[8,9] and will not be presented here.

Often, consecutive rotations are required, for example to connect the PAS, rotor, and lab frames. Such coordinate rotations, shown in Fig. 1.2, can be represented using the addition theorem of Wigner rotation matrices:[8,9]

$$D^{l}_{m'm}(\alpha,\beta,\gamma) = \sum_{m''=-l}^{l} D^{l}_{m'm''}(\alpha_1,\beta_1,\gamma_1) D^{l}_{m''m}(\alpha_2,\beta_2,\gamma_2). \tag{1.40}$$

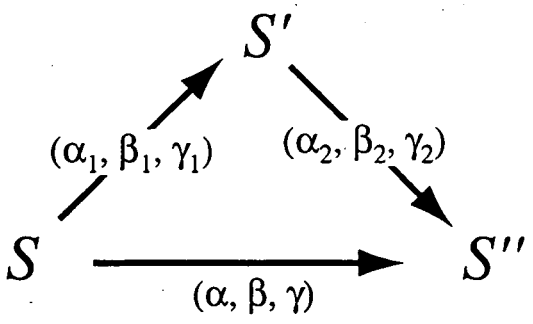

Figure 1.2. Consecutive coordinate transformations relating the S frame with the S'' frame. The sets of Euler angles $(\alpha_1, \beta_1, \gamma_1)$ and (α, β, γ) define the relative orientations of the S' and S'' frames with respect to the S frame. The set of Euler angles $(\alpha_2, \beta_2, \gamma_2)$ define the orientation of the S'' frame with respect to the S' frame.

The consecutive coordinate rotations are demonstrated in Fig. 1.2. The Euler angles (α,β,γ) and $(\alpha_1,\beta_1,\gamma_1)$ are defined with respect to the original S frame while $(\alpha_2,\beta_2,\gamma_2)$ are defined with respect to the intermediate S' frame.

1.3.2 Chemical Shift Hamiltonian

The experiments presented in this thesis take into account only the chemical shift (CS) interaction. Thus none of the other NMR Hamiltonians will be discussed here; a more complete discussion can be found elsewhere.[5] There are two physical origins of the CS Hamiltonian. First is the diamagnetic effect from the electrodynamic interaction due to the motion of the electrons. The diamagnetic effect acts to decrease the overall magnetic field at the nuclei. The second is the paramagnetic effect from the alignment of excited electrons with the static field; this effect acts to increase the overall magnetic field at the nuclei. The CS Hamiltonian can be obtained by defining the tensor terms for the general Hamiltonian given in Eq. 1.34 with the static magnetic field placed along the z axis, $\mathbf{B_0} = B_0\hat{\mathbf{z}}$. Following Haeberlen's notation, the spin tensor terms are:[4]

$$\begin{aligned} T_{00}^{CS} &= B_0 I_z \\ T_{20}^{CS} &= \sqrt{\tfrac{2}{3}} B_0 I_z \\ T_{2\pm1}^{CS} &= \tfrac{1}{\sqrt{2}} B_0 I_{\pm1} \\ T_{2\pm2}^{CS} &= 0, \end{aligned} \tag{1.41}$$

and the coupling tensor terms in the PAS frame are:

$$\begin{aligned} \rho_{00}^{CS} &= \tfrac{1}{3}\left(\sigma_{xx} + \sigma_{yy} + \sigma_{zz}\right) = \sigma \\ \rho_{20}^{CS} &= \sqrt{\tfrac{3}{2}}\left(\sigma_{zz} - \sigma\right) = \sqrt{\tfrac{3}{2}}\delta \\ \rho_{2\pm2}^{CS} &= \tfrac{1}{2}\left(\sigma_{yy} - \sigma_{xx}\right) = \tfrac{1}{2}\eta\delta. \end{aligned} \tag{1.42}$$

In addition, C is defined as he nuclear gyromagnetic ratio, γ_n. Keeping only the first order terms in the CS Hamiltonian that commutes with the Zeeman Hamiltonian,

$$\mathrm{H} = \gamma_n B_0 I_Z, \tag{1.43}$$

and using Eq. 1.39 for the coordinate transformation from the CS PAS frame to an arbitrary reference frame, the CS frequency becomes

$$\omega_{CS} = \omega^i + \sqrt{\tfrac{2}{3}}\omega_0 \sum_m D^2_{m0}(\alpha,\beta,\gamma)\rho_m, \tag{1.44}$$

where ω^i is the isotropic frequency and is defined as $\omega^i = \gamma_n B_0 \sigma$, while $\omega_0 = \gamma_n B_0$.

1.4 Multi-Dimensional NMR

1.4.1 Experimental Procedure

The general scheme for 2D experiments are shown in Fig. 1.3. After the initial excitation, the spin system evolves during the t_1 evolution period with a frequency distribution in ω_1. The system is then altered through combinations of rf pulses, time delays, or sample reorientations. In the final step, the FID is detected during t_2 with the spin system evolving (in general) with a different frequency distribution in ω_2. Several FIDs are acquired for different t_1 delays. The complete signal may then be represented as

$$S(t_1,t_2) = \int_{-\infty}^{\infty}\int_{-\infty}^{\infty} I(\omega_1,\omega_2)\exp\left[i\left(\omega_1 t_1 + \omega_2 t_2\right)\right]d\omega_1 d\omega_2, \tag{1.45}$$

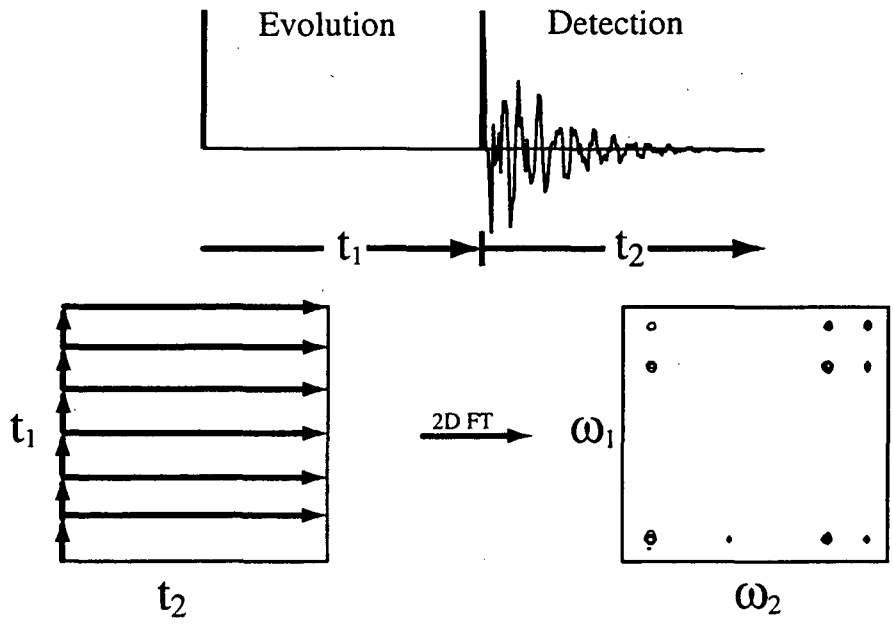

Figure 1.3. Experimental procedure for conventional 2D NMR experiments. The spin system is manipulated so that the signal is governed by two different frequency distributions during the evolution and detection periods. The signal is acquired in t_2 for varying increments of t_1. The final 2D spectrum correlates the two frequency distributions.

where $I(\omega_1,\omega_2)$ is the 2D spectrum correlating the frequency distributions in ω_1 and ω_2. If the complete 2D signal is acquired using fixed time increments (dwell times) in both t_1 and t_2, the entire data set may be placed on a regular 2D grid as shown in Fig. 1.3. This effectively corresponds to evolving the signal orthogonally along each Fourier dimension defined by the Cartesian coordinates (t_1,t_2). The main advantage of having signal data points form a regular grid of evenly spaced points is that a fast Fourier transform (FFT) algorithm may be used to invert Eq. 1.45 and obtain the 2D spectrum $I(\omega_1,\omega_2)$.

This same procedure easily generalizes to higher dimensions by defining additional time evolution periods where the spin system evolves with different frequency distributions. For an n-dimensional experiment there are $n-1$ evolution periods; the FID

is then detected during t_n. The complete multi-dimensional data set is acquired by incrementing each time variable independently. The signal may then be written as

$$S(t_1,t_2,\ldots,t_n)=\int_{-\infty}^{\infty} I(\omega_1,\omega_2,\ldots,\omega_n)\mathrm{e}^{i(\omega_1 t_1+\omega_2 t_2+\cdots\omega_n t_n)}d\omega_1 d\omega_2\ldots d\omega_n \qquad (1.46)$$

and placed on evenly spaced grid points of an n-dimensional matrix.

1.4.2 Lineshapes

The complete spectral information may not always be available in an NMR experiment due to truncation of the signal and relaxation of the spin system; the final experimental spectrum is the convolution of the spectral intensity distribution and a point spread function (PSF) that takes into account truncation and line broadening effects (I will only consider Lorentzian line broadening here).

First, consider the 1D NMR signal in Eq. 1.30. If we assume causality and only allow signal for $t>0$ and also assume that all spectral components have the same Lorentzian line broadening, the signal may be considered to have been multiplied by a function h

$$h(t)=\begin{cases}0, & t<0\\ \exp[-\lambda t], & t\geq 0\end{cases}. \qquad (1.47)$$

According to the convolution theorem, this corresponds to a convolution of the ideal spectrum in the frequency domain by a Lorentzian point spread function (PSF), $P(\omega)$:

$$I'(\omega)=I(\omega)*P(\omega), \qquad (1.48)$$

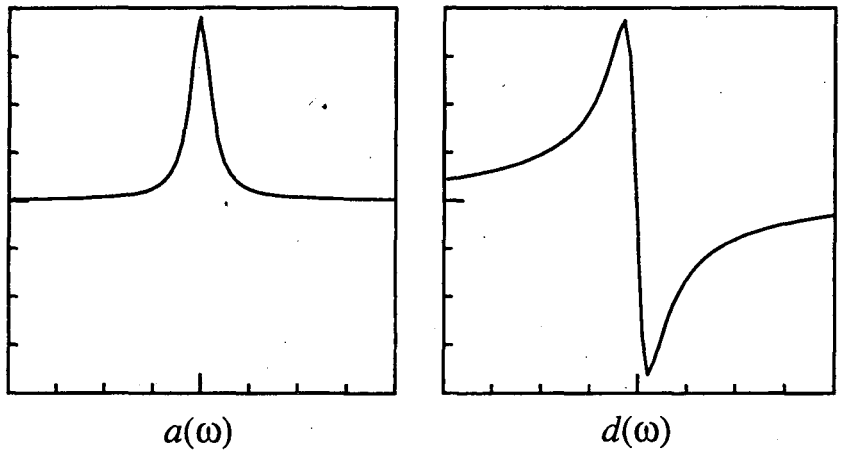

Figure 1.4. Absorption, $a(\omega)$, and dispersion, $d(\omega)$, Lorentzian lineshapes.

The PSF is given by

$$\begin{aligned} P(\omega) &= \int_0^\infty \exp[(-\lambda - i\omega)t]dt \\ &= a(\omega) - id(\omega). \end{aligned} \tag{1.49}$$

where

$$\begin{aligned} a(\omega) &= \frac{\lambda}{\lambda^2 + \omega^2} \\ d(\omega) &= \frac{\omega}{\lambda^2 + \omega^2}. \end{aligned} \tag{1.50}$$

The functions $a(\omega)$ and $d(\omega)$ are referred as the absorption and dispersion Lorentzian lineshapes[5] (Fig. 1.4). Both these function contain the same information and may be transformed into one another through Kramer-Kronig relationships;[5] however their functional forms are completely different. The dispersive component, $d(\omega)$, is a broad antisymmetric function, while $a(\omega)$ is a symmetric function. $a(\omega)$ is identical in form to

the lineshape obtained when no truncation is assumed and the time integral in Eq. 1.47 extended from $-\infty$ to $+\infty$, since then the asymmetric, dispersive term cancels and

$$\int_{-\infty}^{\infty} \exp[(-\lambda - i\omega)|t|]dt = 2a(\omega). \tag{1.51}$$

Thus we see that in 1D experiments, the same information may be obtained by truncating the signal for positive time. This is due to the redundancy of half of the time domain signal

$$S(t) = S(-t)^*. \tag{1.52}$$

However, in 2D experiments, if we truncate the signal for positive t_1 and t_2, the signal will only span $\frac{1}{4}$ of the Fourier space. In this case the complete information available from spanning the entire Fourier space is no longer available. The final 2D spectrum can be written as a 2D convolution of the ideal spectrum with a 2D Lorentzian PSF:

$$I'(\omega_1, \omega_2) = I(\omega_1, \omega_2) ** P(\omega_1, \omega_2). \tag{1.53}$$

Defining the functions

$$\begin{aligned} a_1(\omega_1) &= \frac{\lambda_1}{\lambda_1^2 + \omega_1^2} & a_2(\omega_2) &= \frac{\lambda_2}{\lambda_2^2 + \omega_2^2} \\ d_1(\omega_1) &= \frac{\omega_1}{\lambda_1^2 + \omega_1^2} & d_2(\omega_2) &= \frac{\omega_2}{\lambda_2^2 + \omega_2^2}, \end{aligned} \tag{1.54}$$

the 2D PSF may be calculated as

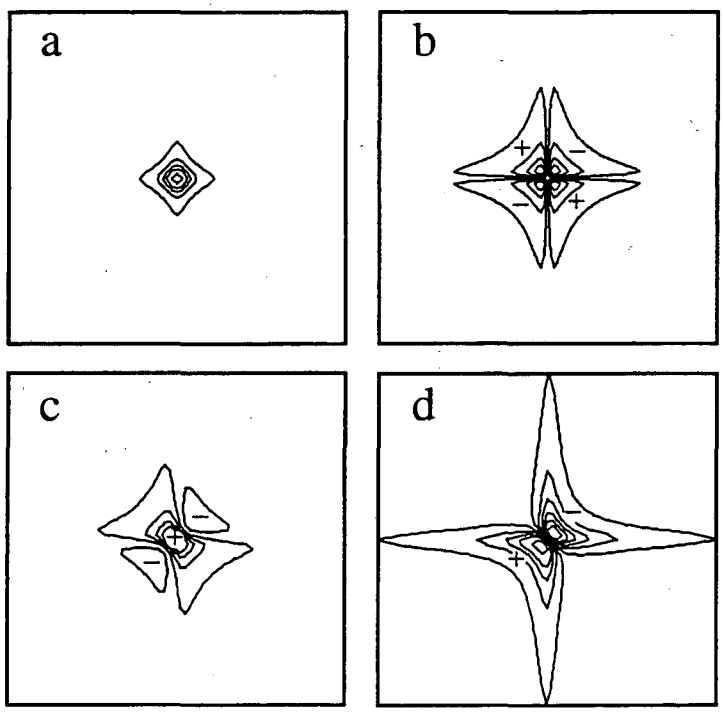

Figure 1.5. 2D Lorentzian lineshapes. (a) and (b) are the pure absorption and dispersion lineshapes, $a_1(\omega_1)a_2(\omega_2)$ and $d_1(\omega_1)d_2(\omega_2)$. (c) and (d) are the mixed phase lineshapes, $a_1(\omega_1)a_2(\omega_2)-d_1(\omega_1)d_2(\omega_2)$ and $a_1(\omega_1)d_2(\omega_2)+d_1(\omega_1)a_2(\omega_2)$.

$$
\begin{aligned}
P(\omega_1,\omega_2) &= \int_0^\infty \exp[(-\lambda_1 - i\omega_1)t_1]dt_1 \int_0^\infty \exp[(-\lambda_2 - i\omega_2)t_2]dt_2 \\
&= [a_1(\omega_1) - id_1(\omega_1)][a_2(\omega_2) - id_2(\omega_2)] \\
&= [a_1(\omega_1)a_2(\omega_2) - d_1(\omega_1)d_2(\omega_2)] \\
&\quad - i[a_1(\omega_1)d_2(\omega_2) + a_2(\omega_2)d_1(\omega_1)].
\end{aligned}
\tag{1.55}
$$

Equation 1.55 shows that by truncating both the t_1 and t_2 dimensions, a pure absorptive lineshape, $a_1(\omega_1)a_2(\omega_2)$, is not possible; both the real and imaginary components of $P(\omega_1,\omega_2)$ contain absorption and dispersion terms and are often called "mixed phased" or "phase twist" lineshapes (Fig. 1.5). Such lineshapes can create severe distortions in the final spectrum, and thus the problem has been thoroughly studied in multi-dimensional NMR and several methods have been developed to remove these distortions and obtain

"pure-phase" lineshapes.[10-12] Similar lineshape distortion in relation to the VACSY experiments will be discussed in chapter 3.

References

1. I. J. Lowe, and R. E. Norberg, Phys. Rev., **107**, 46 (1957).

2. R. R. Ernst, and W. A. Anderson, Rev. Sci. Instrum., **37**, 93 (1966).

3. A. Abragam, *Priciples of Nuclear Magnetism*; Clarendon Press, Oxford, 1961.

4. U. Haeberlen, *High Resolution NMR in Solids: Selective Averaging, Advances in Magnetic Resonance, Supplement 1*; Academic, New York, 1976.

5. R. R. Ernst, G. Bodenhausen, and A. Wokaun, *Principles of Nuclear Magnetic Resonance in One and Two Dimensions*; Clarendon Press, Oxford, 1987.

6. H. Goldstein, *Classical Mechanics*; Addison-Wesley, Reading MA, 1950.

7. G. Arfken, *Mathematical Methods for Physicists*; Academic Press Inc., Orlando, 1985.

8. M. E. Rose, *Elementary Theory of Angular Momentum*; Wiley and Sons, New York, 1957.

9. D. A. Varshalovich, A. N. Moskalev, and V. K. Khersonskii, *Quantum Theory of Angular Momentum*; World Scientific, Singapore, 1988.

10. P. Bachmann, W. P. Aue, L. Muller, and R. R. Ernst, J. Magn. Reson., **28**, 29 (1977).

11. D. J. States, R. A. Haberkorn, and D. J. Ruben, J. Magn. Reson., **48**, 286 (1982).

12. D. Marion, and K. Wutthrich, Biochem. Biophys. Res. Commun., **113**, 967 (1983).

Chapter 2 2D VACSY

2.1 Introduction

Much of the success in interpretation of NMR experiments relies upon the ability to resolve distinct resonant frequencies for each chemical site. The high resolution provided by technical advances in high-field superconducting magnets and the development of multi-dimensional techniques has made possible NMR studies of increasingly complex biological molecules in solution.[1] High resolution NMR in solids has similarly led to studies of more complex systems. However, unlike liquid-state NMR, where the fast tumbling motions of molecules provide a high resolution spectrum naturally, solid-state NMR requires experimental averaging techniques to remove the broad, orientation-dependent components of the spectrum.[2,3] The removal of these anisotropic components, however, has the unfortunate consequence of also removing structural and dynamical information, which makes the ability to selectively reintroduce anisotropic spectral information an important aspect of solid-state NMR. Experiments may be designed to yield both the high resolution needed to study complex systems and the anisotropic information needed to characterize the structural and dynamical properties of molecules. Useful techniques of this type include 2D and 3D experiments where high resolution, isotropic frequencies along one dimension are correlated with broad, anisotropic frequency distributions in the other dimensions.[4-10]

An alternative 2D technique, variable angle correlation spectroscopy (VACSY),[11] is presented in this and the following chapters. An important feature of VACSY is its experimental simplicity; no synchronized multiple pulse sequences or rapid sample reorientations are required for correlating isotropic and anisotropic frequencies. Figure 2.1 shows the basic principle behind the VACSY technique: the anisotropic frequency scales

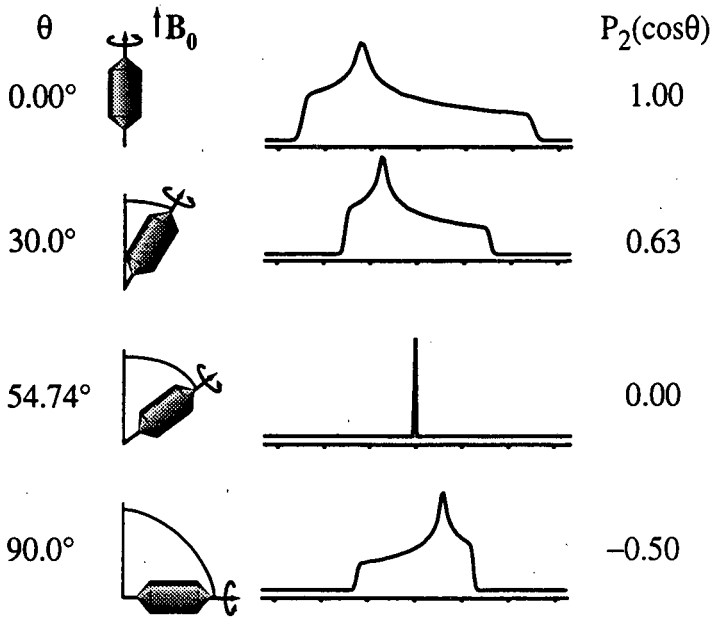

Figure 2.1. Rotation axis angle dependent scaling of an anisotropic pattern with $\eta = 0.5$. As θ, the angle between the spinning axis and the static magnetic field changes, the isotropic shift remains invariant while the anisotropic pattern scales by the second Legendre polynomial, $P_2(\cos\theta)$.

with the change in the rotation axis angle, θ, while the isotropic frequency is left invariant. This allows a set of variable-angle-spinning (VAS) FIDs to be rearranged on a 2D grid such that a Fourier transformation directly yields the isotropic to anisotropic correlations.

The general theory and methodology of 2D VACSY will be discussed in this chapter; linear prediction with singular value decomposition to remove phase artifacts in 2D VACSY will be presented in chapter 3; and applications of 2D VACSY will be presented in chapter 4. Extension of the 2D VACSY technique to three dimensions for the study of slow molecular exchange will be presented in chapter 5.

2.2. General VACSY Theory

VACSY experiments are based on the generalization of the Fourier transformation and data acquisition in NMR spectroscopy. As discussed in chapter 1,

conventional multi-dimensional NMR spectroscopy methods involve incrementing n time variables independently and placing the acquired signal, $S(t_1,t_2,\ldots,t_n)$, on evenly spaced Cartesian grid points in an n-dimensional matrix. An FFT routine may then be used to obtain the spectrum, $I(\omega_1,\omega_2,\ldots,\omega_n)$. This method of using time increments and Cartesian data acquisition has been extended and generalized in NMR imaging. For example, it is often advantageous in NMR imaging to evolve the Fourier phase by incrementing the magnitude of the magnetic field gradient rather than time.[12] There are also several NMR imaging methods that take advantage of non-Cartesian data acquisition where experimental data points no longer fall a rectangular grid, but where gradients are manipulated so that the signal forms radial,[13,14] skewed[15] or even spiral[16] trajectories in the signal Fourier space. Non-Cartesian sampling of the Fourier space, however, usually requires subsequent interpolation in order to use the FFT or to display the image.

Therefore, while the usual methods of incrementing time and acquiring data orthogonally along each Fourier dimension are often experimentally convenient and facilitate the use of the FFT, *they are not fundamental requirements for multi-dimensional NMR experiments*. The important requirement is that the phase which the system acquires during the experiment must be separable as a sum of individual terms, each expressible as a product of two variables:[17]

$$\Phi = \sum_{i=1}^{n} \Phi_i = \sum_{i=1}^{n} \omega_i \tau_i . \qquad (2.1)$$

Each Φ_i represents the phase acquired by the system along one Fourier dimension. The frequency variables, ω_i, define the coordinate axes for the spectral intensity distribution, and the "generalized time" variables, τ_i, have units of time and define the coordinates for the signal acquisition Fourier space. These latter variables are under experimental control

and are varied during signal evolution and detection. The signal for an n-dimensional experiment is now redefined as

$$S(\tau_1, \tau_2, \ldots, \tau_n) = \int_{-\infty}^{\infty} I(\omega_1, \omega_2, \ldots, \omega_n) e^{i\Phi} d\omega_1 d\omega_2 \ldots d\omega_n, \qquad (2.2)$$

and integrating over the variables τ_i, the spectrum $I(\omega_1, \omega_2, \ldots, \omega_n)$ can be obtained through a Fourier transformation. This generalization of time variables and signal acquisition phase space can become a powerful tool, allowing the use of new experimental parameters and procedures to extract precisely the information desired in the spectrum. The coordinates in ω space determine the variables to be correlated in the spectrum, while the coordinates in τ space specify how the FIDs should be placed in the signal acquisition phase space. An n-dimensional experiment still requires n experimental parameters that must be incremented independently to allow the signal phase space to be densely filled with data, but there is considerably more latitude in how they are chosen.

In the VACSY experiments, the angle of the spinning axis with respect to the static magnetic field, $\mathbf{B}_0$, is one of the variables that controls the phase that the signal acquires. The pulse sequences and the angle profiles for three different VACSY experiments are shown in Fig. 2.2; the Fourier variables and phases relevant to each experiment are listed in Table 2.1. The design of all three experiments follows the same procedure. First, the frequency variables must be chosen to provide the desired correlation information from the multi-dimensional spectrum. For the VACSY experiments, isotropic frequencies in one dimension are correlated with anisotropic frequencies in other dimensions, as shown in Column 4 of Table 2.1. Next, the phase acquired by the spin system during the time evolution periods is written in the same form as Eq. 2.1 by partitioning the phase along different dimensions (Column 2) such that the phase for each dimension may be factored

a 2D VACSY

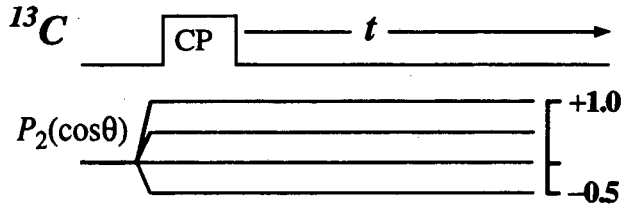

b 3D VACSY-S Exchange

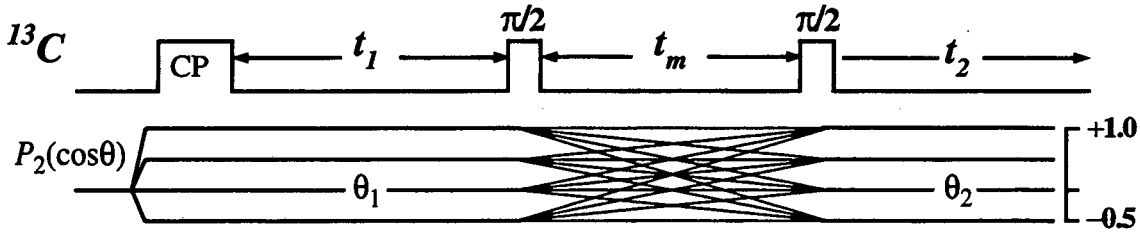

c 3D VACSY-T Exchange

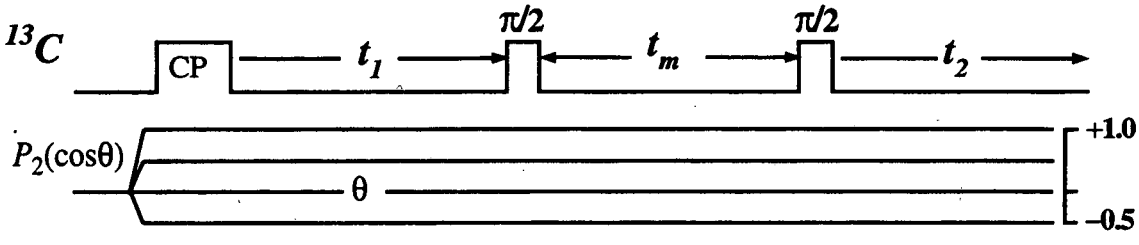

Figure 2.2 Pulse sequences for three different VACSY experiments. Below each pulse sequence is a graph of how $P_2(\cos\theta)$ is varied. (a) 2D VACSY experiment, used to correlate isotropic frequencies with 1D anisotropic frequency distributions. FIDs are acquired at different $P_2(\cos\theta)$ values. (b) 3D VACSY-S exchange experiment, used to correlate the isotropic frequencies with the anisotropic frequency distributions measured before and after the t_m mixing delay. The angles θ_1 and θ_2 are varied independently during the experiment. (c) 3D VACSY-T exchange experiment that obtains the same correlations as VACSY-S but without the need for rapid sample reorientation. 2D exchange experiments are acquired at different $P_2(\cos\theta)$ values. Experiments (b) and (c) will be discussed in chapter 5.

Experiments	Components of the Signal Phase $\Phi = \vec{\omega}\cdot\vec{\tau}$	Adjustable Parameters	Correlated Frequencies	Data Coordinates in τ Space
2D VACSY	$\Phi_1 = \omega^a P_2(\cos\theta)t$ $\Phi_2 = \omega^i t$	θ, t	$\begin{bmatrix}\omega_1\\ \omega_2\end{bmatrix} = \begin{bmatrix}\omega^a\\ \omega^i\end{bmatrix}$	$\begin{bmatrix}\tau_1\\ \tau_2\end{bmatrix} = \begin{bmatrix}P_2(\cos\theta)t\\ t\end{bmatrix}$
3D VACSY-S Exchange	$\Phi_1 = \omega_1^a P_2(\cos\theta_1)t_1$ $\Phi_2 = \omega_2^a P_2(\cos\theta_2)t_2$ $\Phi_3 = \omega^i t_2$	θ_1, θ_2, t_2	$\begin{bmatrix}\omega_1\\ \omega_2\\ \omega_3\end{bmatrix} = \begin{bmatrix}\omega_1^a\\ \omega_2^a\\ \omega^i\end{bmatrix}$	$\begin{bmatrix}\tau_1\\ \tau_2\\ \tau_3\end{bmatrix} = \begin{bmatrix}P_2(\cos\theta_1)t_1\\ P_2(\cos\theta_2)t_2\\ t_2\end{bmatrix}$
3D VACSY-T Exchange	$\Phi_1 = \omega_1^a P_2(\cos\theta)pt_1$ $\Phi_2 = \omega_2^a P_2(\cos\theta)t_2$ $\Phi_3 = \omega^i(pt_1 + t_2)$	θ, t_1, t_2	$\begin{bmatrix}\omega_1\\ \omega_2\\ \omega_3\end{bmatrix} = \begin{bmatrix}\omega_1^a\\ \omega_2^a\\ \omega^i\end{bmatrix}$	$\begin{bmatrix}\tau_1\\ \tau_2\\ \tau_3\end{bmatrix} = \begin{bmatrix}P_2(\cos\theta)pt_1\\ P_2(\cos\theta)t_2\\ (pt_1 + t_2)\end{bmatrix}$

Table 2.1 The partitioned Fourier phases and the conjugate Fourier variables for three VACSY experiments. The variables designated as ω^a are the anisotropic frequencies; ω^i is the isotropic frequency; θ, θ_1, θ_2 are the rotation axis angles with respect to the static magnetic field; $P_2(\cos\theta)$ is the second Legendre polynomial; t, t_1, and t_2 are the time variables; and p is the sign of the t_1 coherence pathway (discussed in chapter 5).

into the desired frequency variables, ω_i, and the generalized time variables, τ_i, (Column 5). Each τ_i must be distinguished from the others through different combinations of independently adjustable parameters to ensure that the signal spans a significant portion of the multi-dimensional Fourier space. These parameters, listed in Column 3, are either time variables (t, t_1, t_2) or the rotation axis angles ($\theta, \theta_1, \theta_2$). Finally, the FIDs are placed in τ space according to coordinates that are linear functions of time, so that the FIDs form linear trajectories whose orientations in τ space are determined by the rotation axis parameters. The data points are then interpolated onto a Cartesian grid and Fourier transformed. I will now discuss the specific experimental procedure of the 2D VACSY experiment. The two 3D VACSY experiments will be presented in chapter 5.

2.3 2D VACSY Theory

2D VACSY will first be described for rapidly spinning samples evolving under the chemical shift interaction. When the sample is rotated, the Euler angles for the chemical shift frequency in Eq. 1.44 gain a time dependence

$$\omega_{cs} = \omega^i + \sqrt{\frac{2}{3}}\,\omega_\circ \sum_m D^2_{m0}(\Omega(t))\rho_m. \tag{2.3}$$

Using the addition theorem of Wigner rotation Matrices (Eq. 1.40), the overall motion of the CSA tensor may be decomposed into two consecutive rotations:

$$\omega_{cs} = \omega^i + \sqrt{\frac{2}{3}}\,\omega_\circ \sum_{m,m'} D^2_{mm'}(\alpha,\beta,\gamma) D^2_{m'0}(\omega_r t,\theta)\rho_m, \tag{2.4}$$

where ω_r is the rotational frequency of the rotor. The first set of Euler angles, (α,β,γ), rotates the coordinate axes from the CSA tensor PAS frame to the rotor frame; the second

set of Euler angles rotates the coordinate axes from the rotor frame to the lab frame. Under rapid sample rotation, Eq. 2.4 simplifies to[2]

$$\begin{aligned}\omega_{cs} &= \omega^i + P_2(\cos\theta)\sqrt{\tfrac{2}{3}}\,\omega_0 \sum_m D^2_{m0}(\alpha,\beta)\rho_m \\ &= \omega^i + P_2(\cos\theta)\omega^a(\alpha,\beta),\end{aligned} \tag{2.5}$$

where $\omega^a(\alpha,\beta)$, the anisotropic frequency defined with respect to the rotor axis frame, has the identical functional form as the anisotropic frequency of a static sample. The phase acquired by the system under VAS conditions may then be written as

$$\Phi = \omega^i t + P_2(\cos\theta)\omega^a(\alpha,\beta)t. \tag{2.6}$$

The signal may be written in the same form as Eq. 2.1 if the phase along the two dimensions is partitioned as

$$\begin{aligned}\Phi_1 &= \omega^a(\alpha,\beta)P_2(\cos\theta)t \\ \Phi_2 &= \omega^i t,\end{aligned} \tag{2.7}$$

$$\begin{pmatrix}\tau_1 \\ \tau_2\end{pmatrix} = \begin{pmatrix}P_2(\cos\theta)t \\ t\end{pmatrix}. \tag{2.9}$$

The two experimental parameters that are varied independently in 2D VACSY are the angle θ and time t, i.e., FIDs are acquired at different θ angles. Unlike conventional 2D NMR experiments where the signal $S(t_1,t_2)$ is acquired by incrementing the time variables t_1 and t_2 independently, τ_1 and τ_2 for 2D VACSY are linearly dependent on each other. Thus VAS FIDs acquired for 2D VACSY will evolve along both the τ_1 and τ_2 dimensions simultaneously, forming linear trajectories in τ space whose slopes are determined by

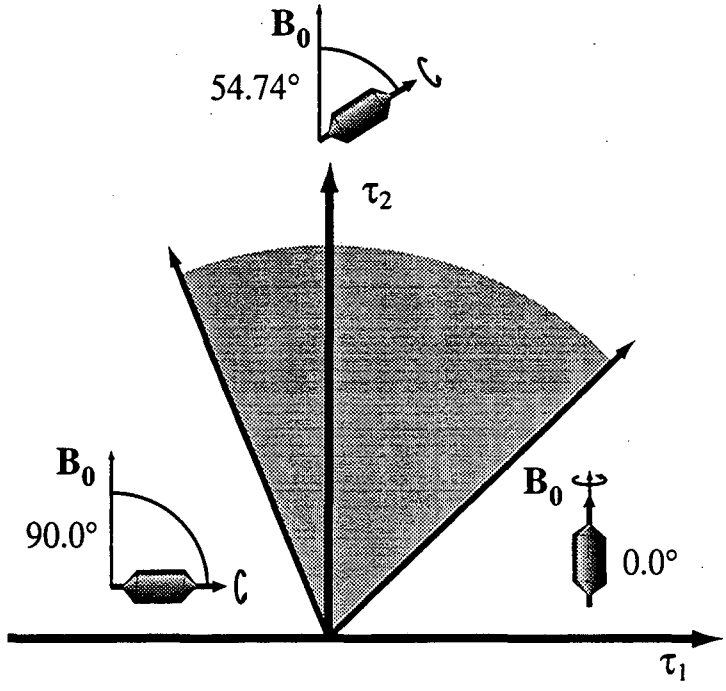

Figure 2.3. Placement of FIDs according to the τ space coordinates defined for the 2D VACSY experiment.

$P_2(\cos\theta)$ (Fig. 2.3). As a result, the data acquired in 2D VACSY will no longer necessarily fall on vertices of a Cartesian coordinate grid. Incrementing different values of θ scales the evolution along the τ_1 dimension by $P_2(\cos\theta)$ while having no affect on the evolution along τ_2; this allows the data acquired at different values of θ and t to span the 2D Fourier space.

All of the VAS FIDs are acquired using the same dwell time, t_d. The spectral width along the isotropic ω_2 dimension is then set by t_d, while the spectral width along the anisotropic ω_1 dimension can be varied by placing the FIDs at different orientations in τ space. Let δ_1 and δ_2 represent the discrete grid increments along the τ_1 and τ_2

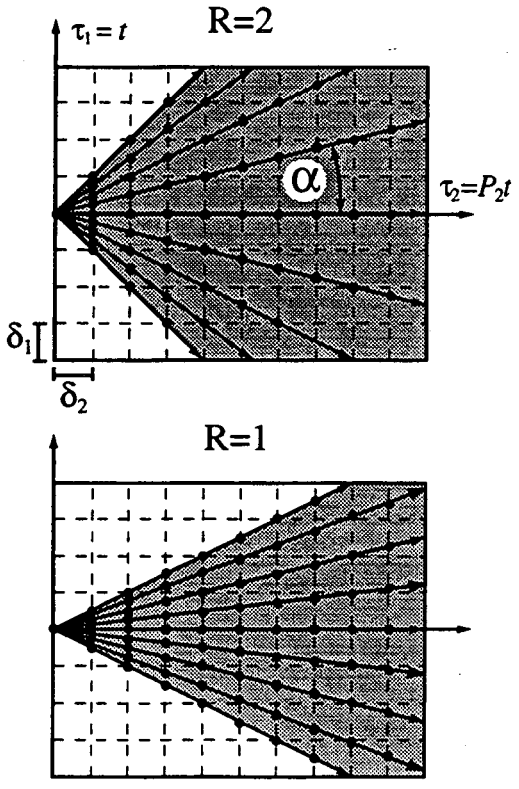

Figure 2.4. Two different coordinate mappings for the 2D VACSY data with the condition, $-0.5 \le P_2(\cos\theta) \le 0.5$. The dark lines represent the trajectory of the FIDs, with each FID inclined at an angle $\alpha = \tan^{-1}\left[RP_2(\cos\theta)\right]$. The dots represent the experimental data points. The variables δ_1 and δ_2 are unit grid increments in the τ_1 and τ_2 dimensions.

dimensions, as shown in Fig. 2.4. If the spectral widths along the two dimensions are chosen the same, then both δ_1 and δ_2 represent time values of t_d, and the slopes of the FIDs placed in τ space are determined only by $P_2(\cos\theta)$. If the spectral width in the anisotropic ω^a dimension is chosen to be different, each δ_2 increment will still represent a time value of t_d, but δ_1 will represent a scaled time of t_d/R, where R is ratio of the anisotropic to isotropic spectral widths, $R = sw^a/sw^i$. Taking into account this scaling, Eq. 2.9 may be written in discrete index form as

$$\tau_1 = P_2(\cos\theta)Rnt_d$$
$$\tau_2 = nt_d, \tag{2.10}$$

where n is an integer that indexes the grid increments. The orientation of each FID in the τ space is then determined by the angle

$$\alpha = \tan^{-1}\left[RP_2(\cos\theta)\right], \tag{2.11}$$

as shown in Fig. 2.4. The figure also shows that for any given range of $P_2(\cos\theta)$, the experimental data spans a larger area of τ space for larger values of R. Since the dwell time for each FID is the same, all of the data points will map directly onto one of the evenly space grid lines perpendicular to the τ_2 dimension. As shown in Fig. 2.4, interpolation is only required along the τ_1 dimension to obtain data on a Cartesian grid required for the FFT. Only the grid points within the shaded boundary set by the FIDs with the maximum and minimum slopes (Fig. 2.4) will be interpolated. Each grid vertex, g, within this shaded region is bound by two experimental data points, e_1 and e_2, as shown in Fig. 2.5.

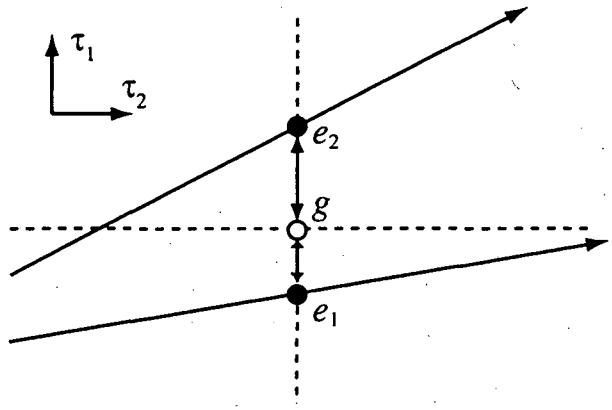

Figure 2.5. Interpolation procedure in 2D VACSY. The solid lines are the FIDs; the dashed lines are the lines of the Cartesian grid. The two solid dots labeled e_1 and e_2 are the nearest experimental points to the grid vertex g. All experimental data points lie on one of the grid lines parallel to the τ_1 aixs; thus interpolation is only required along the τ_1 dimension. The experimental points e_1 and e_2 are used to interpolate g.

Linear or cubic spline interpolation along the τ_1 dimension using the two nearest experimental data points usually suffices to obtain accurate intensities of for all of these grid points. The grid points outside of the shaded region are no longer bounded by experimental data points, and their intensities must either be set to zero or be extrapolated from the experimental data. Setting these grid points to zero will lead to phase distortions and other artifacts in the spectrum. The removal of these artifacts through extrapolation by linear prediction routines will be discussed in chapter 3. Figure 2.6 shows the three experimental stages of 2D VACSY data: first, the directly acquired VAS FIDs; next the interpolated data in τ space; finally, the 2D correlation spectrum obtained by Fourier transformation.

2.4 Experimental

The 2D VACSY technique is demonstrated by ^{13}C NMR experiments on some simple organic molecules. All experiments in this section were conducted with a home-built spectrometer, using a 4.2 T superconducting magnet with a ^{13}C resonance frequency of 45.2 MHz. The probe employed a double tuned circuit and a single coil wrapped around a moveable stator. The orientation of the stator is set by a stepper motor, located at the base of the magnet, and controlled by a computer. All the hardware designed for these experiments are described in chapter 6.

A conventional CP sequence with phase inversion of the initial decoupler 90° pulse and flip-back pulse was used to acquire the signals. Hartmann-Hahn match condition was achieved at a nutation rate of 80 kHz, using 200 W in the ^{13}C channel and 100 W in the ^{1}H channel. The rotation axis angle was referenced to the magic angle by maximizing the rotational echoes of the ^{81}Br FID of solid KBr. Since the rf coil is fixed around the stator,

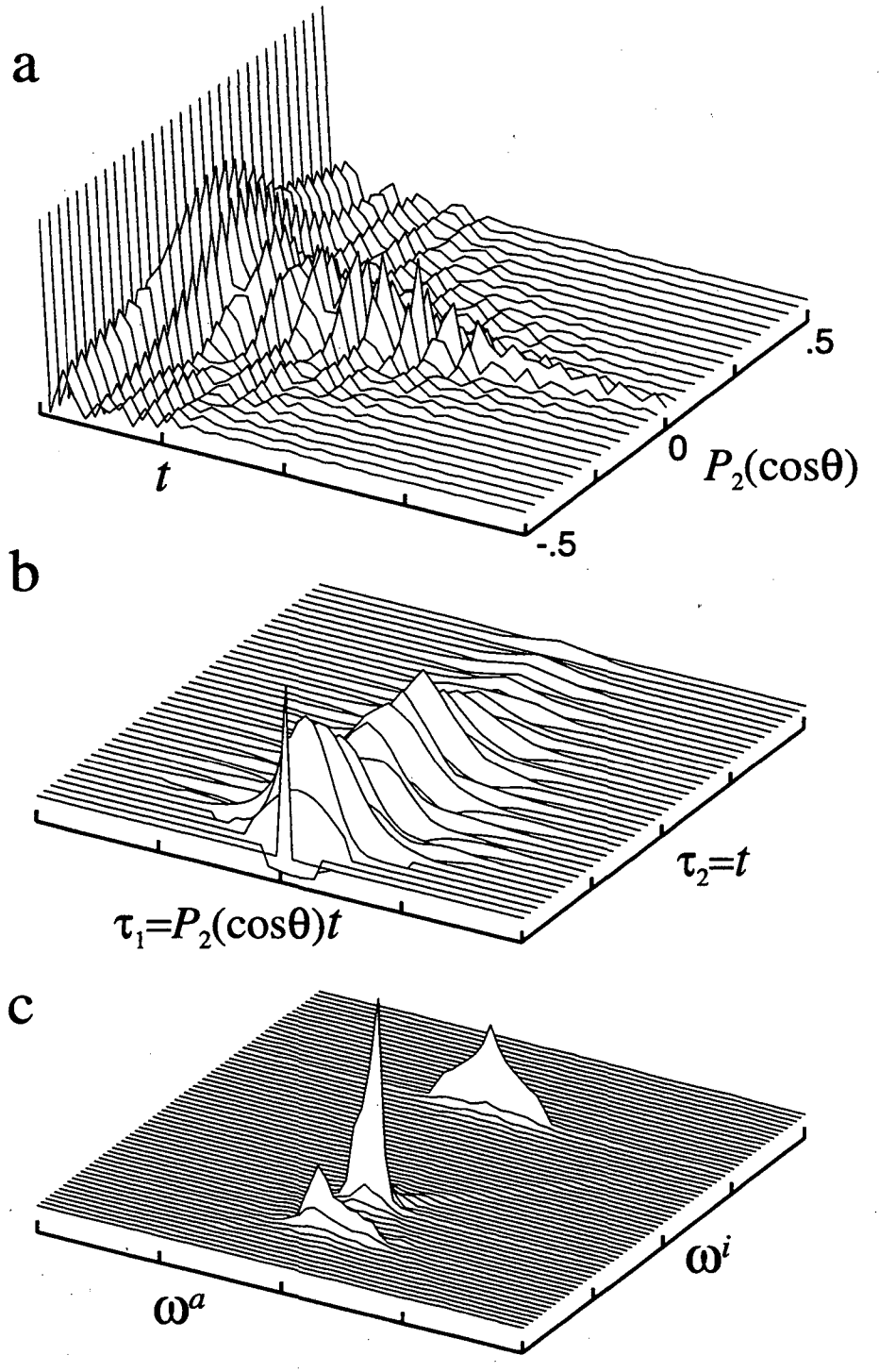

Figure 2.6 Simulated data showing the three stages of processing for 2D VACSY. (a) Series of variable angle spinning FIDs for $P_2(\cos\theta)$ in the range of +0.5 and -0.5. (b) VACSY data after interpolation onto the τ space coordinates. (c) Isotropic- anisotropic correlated spectrum after Fourier transforming the τ space data in (b).

the strength of the excitation field scales as $\sin(\theta)$. Thus the range of angles used in the experiment is restricted to $-0.5 < P_2(\cos\theta) < 0.5$.

Figure 2.7 shows the results of a 2D VACSY experiment on glycine. Altogether 75 different rotation axis angles were sampled from 90° to 35.3°, and 256 points were acquired in each FID. The data were then interpolated and zero-filled onto a 512x512 grid as described earlier. A Fourier transformation and a magnitude calculation were then used to obtain the final spectrum. Figure 2.7a shows a normal CPMAS spectrum of glycine, and figure 2.7b shows a slice from the 2D VACSY spectrum at $\omega^a = 0$. Some resolution has been lost along the isotropic dimension due to the introduction of dispersive terms from the magnitude calculation. Figure 2.7c shows the slices from the 2D VACSY spectrum taken parallel to the ω^a axis at the three different sites of glycine. All three of the powder patterns reveal sharp singularities of the traceless CSA interaction. Note that even with the magnitude calculation, each of these sites appears to be in pure-absorption mode with sharp singularities. This will be discussed further in chapter 3.

Fig. 2.8 shows the 2D correlation spectrum of a more complex system, p-anisic acid. Although in solution the ^{13}C NMR spectrum displays six inequivalent carbon peaks, solid-state effects introduce an additional splitting for the aromatic carbon resonances ortho to the $-OCH_3$ group. The resulting seven resonances are clearly resolved, and the anisotropic spectrum for each site is shown in Fig. 2.9. The CSA tensor elements can be obtained by measuring the singularities of each experimental powder pattern; these parameters are then used to simulate the powder patterns. The nonprotonated carbon sites, f, d, and g show the largest deviations from ideal powder lineshapes. Thus we attribute these distortions to cross polarization efficiency rather than the experimental technique. The tensor parameters are listed in Table 2.2.

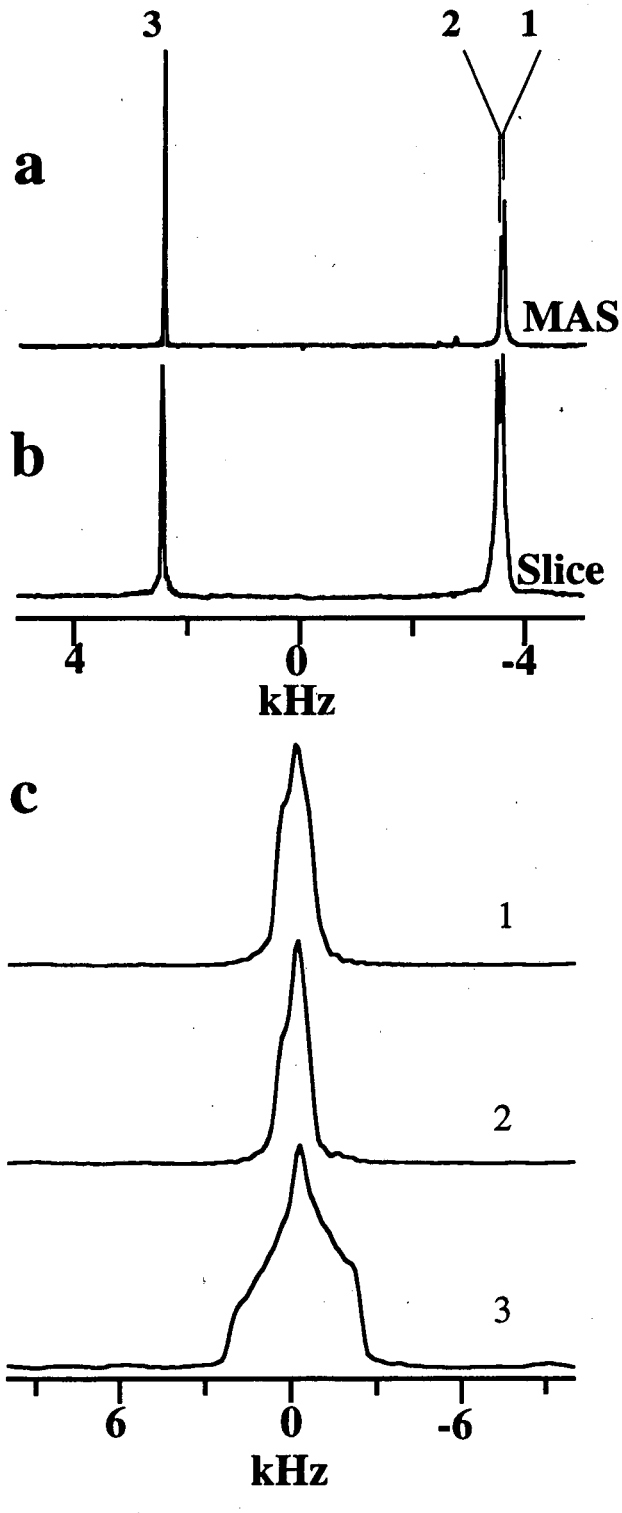

Figure 2.7 (a) MAS spectrum of glycine. (b) Slice taken along the isotropic axis from the 2D VACSY spectrum. (c) Anisotropic slices taken from the 2D VACSY spectrum.

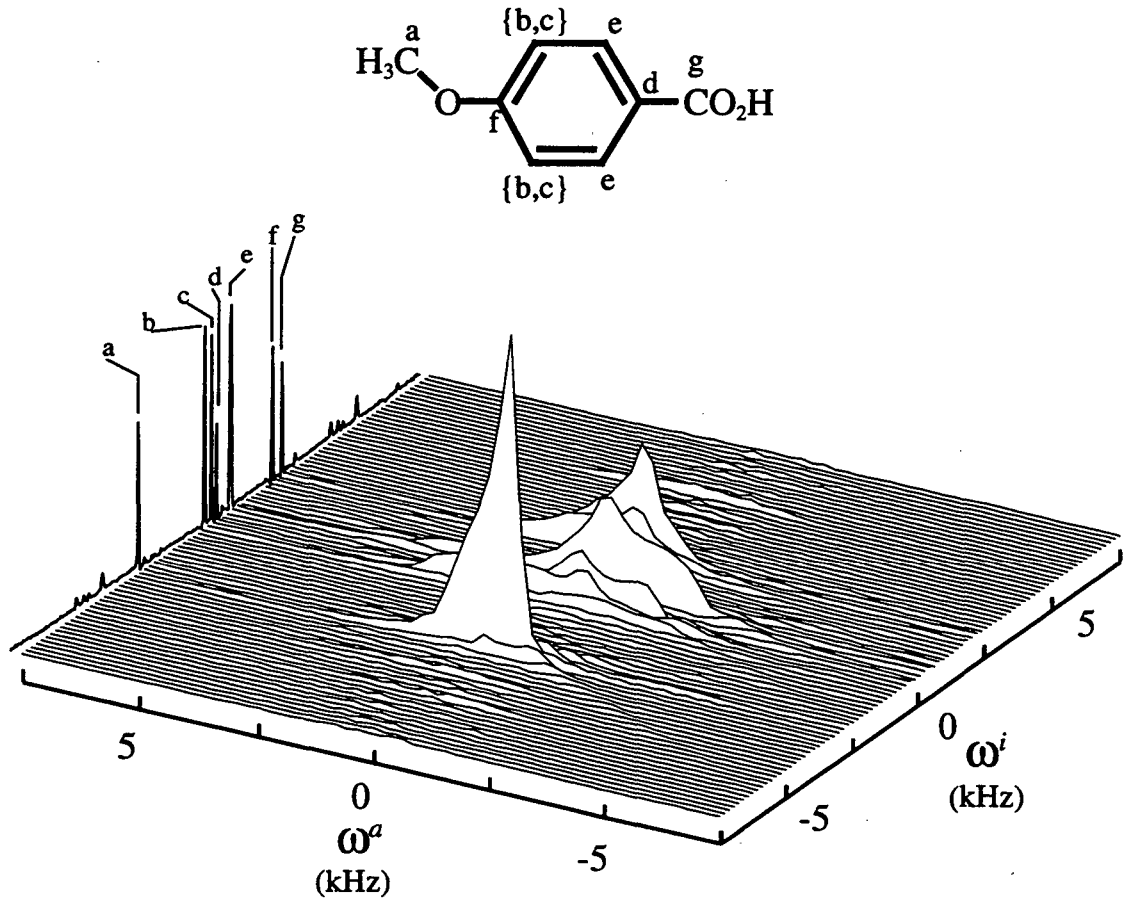

Figure 2.8 2D isotropic-anisotropic correlation spectrum of p-anisic acid, showing the isotropic projection and the assignment of the peaks for each site of the molecule

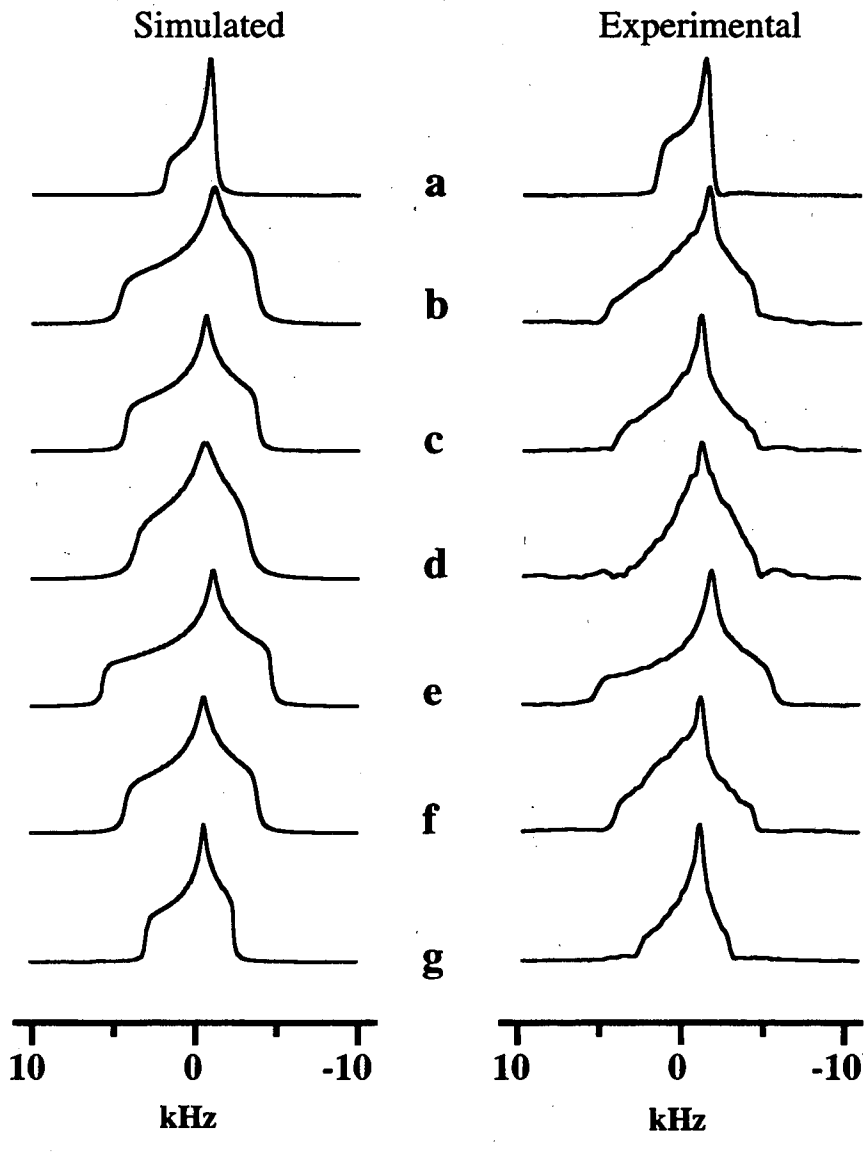

Figure 2.9 Experimental and simulated line shapes of anisotropic slices from the 2D VACSY spectrum of p-anisic acid. Each pair of spectra corresponds to the carbon labeled with the same letter in Figure 2.8.

Carbon atom	δ (ppm)	η
a	-42	0.16
b	-104	0.55
c	-46	0.72
d	-83	0.71
e	-126	0.63
f	-95	0.77
g	-65	0.63

Table 2.2. ^{13}C traceless CSA parameters of p-anisic acid

2.5 Analysis of experimental errors

Due to the unconventional data processing in 2D VACSY, several new sources of experimental errors may degrade the quality of the 2D spectrum. Some of these errors will be analyzed with simulations in the following sections.

2.5.1 Slow Spinning Effects

Equation 2.5 for the CSA frequency assumes $\omega_r >> \delta_{csa}$. When this condition no longer holds then all of the terms in Eq. 2.4 must be included in calculating the phase acquired by the system:

$$\Phi = \omega^i t + P_2(\cos\theta)\omega^a t + \int_0^t \sum_{m'=\pm1,\pm2} A_{m'}(\alpha,\beta,\gamma)\exp(-im'\omega_r t')dt', \tag{2.12}$$

where

$$A_{m'}(\alpha,\beta,\gamma) = \sqrt{\tfrac{2}{3}}\,\omega_{\circ} \sum_{m=-2}^{2} D^{2}_{mm'}(\alpha,\beta,\gamma)\rho_{m}. \qquad (2.13)$$

However, one of the dimensions may still be defined as a "high-resolution" dimension by partitioning the phase as

$$\begin{aligned} \Phi_1 &= P_2(\cos\theta)\omega^a t \\ \Phi_2 &= \omega^i t + \int_0^t \sum_{m'=\pm1,\pm2} A_{m'}(\alpha,\beta,\gamma)\exp(-im'\omega_r t')dt'. \end{aligned} \qquad (2.14)$$

Now, the ω_2 dimension can no longer be considered an isotropic dimension since Φ_2 depends on the Euler angles (α,β,γ), but Φ_2 is simply the phase acquired in an MAS experiment with rotational echoes. Thus by using the same definition of τ coordinates and the same interpolation procedure, the high resolution MAS spectrum in the ω_2 dimension is correlated with the broad frequency distributions in ω_1. The resolution of a 2D VACSY experiment in the ω_2 dimension is degraded by the addition of the time dependent terms in Φ_2 which contributes spinning sidebands to the spectrum, but this is the same resolution available in an MAS experiment at the same spinning speed. Figure 2.10 shows simulations of 2D VACSY spectra at different rotational frequencies. Figure 2.11 shows that despite the lineshape deformations, the CSA tensor values may still be obtained from the spectrum.

2.5.2 Interpolation Error

The number of VAS FIDs required for 2D VACSY depends on the width of the anisotropic patterns. As the number of sampled rotation axis angles decreases, the average distance from each grid point to the nearest experimental data points increases, resulting in

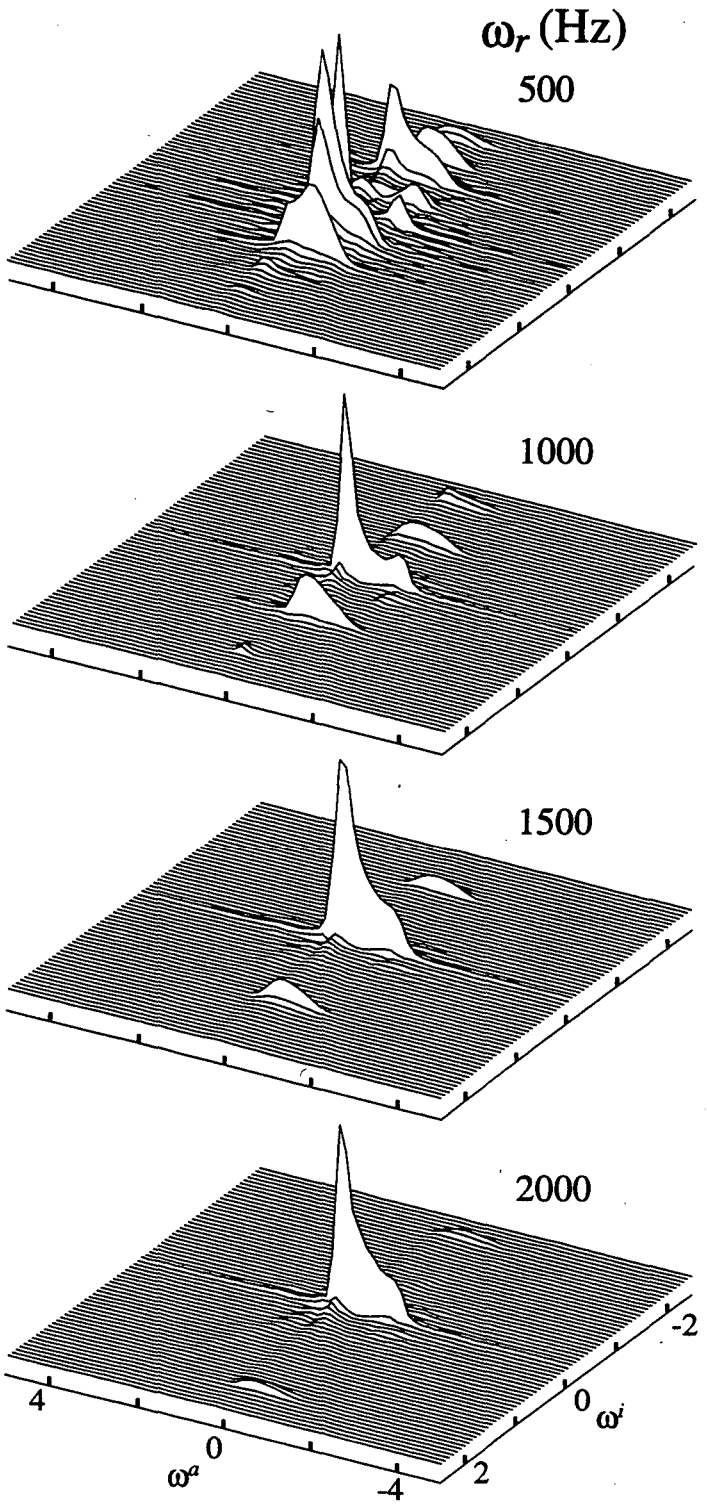

Figure 2.10 Simulations of 2D VACSY spectra at different spinning speeds. All simulations were made with $\delta = -2$ kHz and $\eta = 0$. The axes are labeled in kHz.

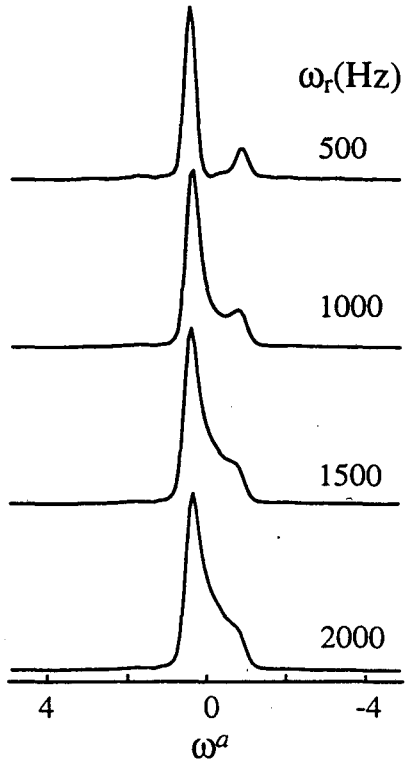

Figure 2.11. Anisotropic slices from the 2D VACSY spectra in Fig. 2.10.

interpolation errors. Figure 2.12 shows the lineshape distortions that can appear when the number of acquired FIDs becomes too small. A general "rule-of thumb" in doing the VACSY experiments is to use at least 31 different angles when the largest anisotropic pattern in the spectrum is about half of the isotropic spectral width.

2.5.3 Random Angle Missettings

As discussed above, the placement of each FID in τ space is determined by $P_2(\cos\theta)$, so any error in the angle settings will degrade the spectrum. Both systematic and random errors can occur. Systematic angle errors may come about from the initial

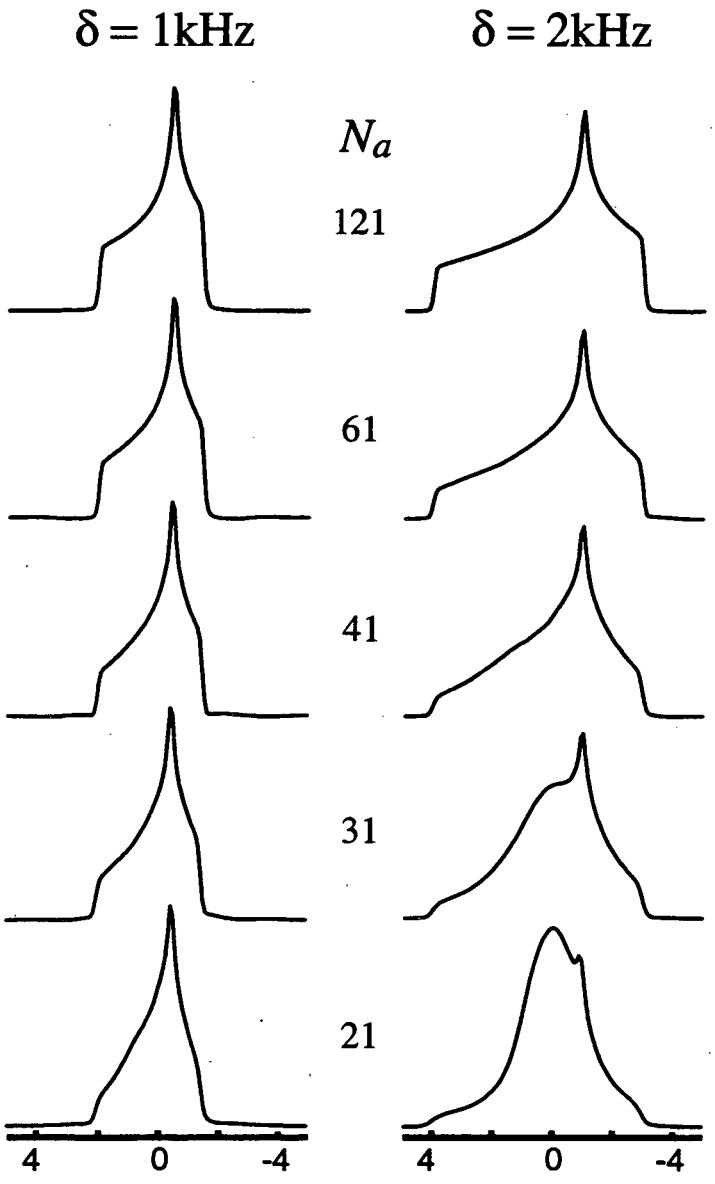

Figure 2.12 2D VACSY simulations with different numbers of sampled angles, N_a. The two sets of simulations are for δ = 1 kHz and 2 kHz, both with η = 0.5. Each simulated data set corresponds to an even sampling of P_2 values in the range of +0.5 and -0.5. The line shape distortions for decreasing N_a become much more severe for the set of simulations with the larger anisotropy.

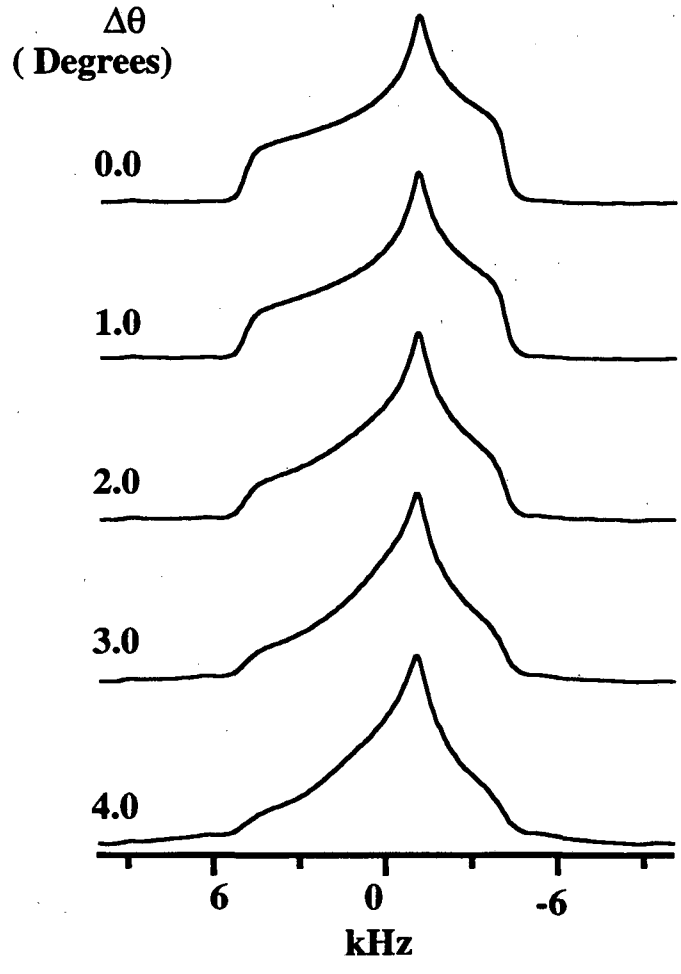

Figure 2.13 Line shape distortions caused by random angle error, $\Delta\theta$. The simulations were made for a CSA tensor characterized by δ=5 kHz and η = 0.6. Errors in the spinning angles for each of the 64 FIDs were introduced using a random-number generator.

missetting of the magic-angle. However, by using standard references for setting the magic angle, this error can be minimized to less than 0.1° and should be insignificant. Random errors in the angle settings are introduced because of the inability of the apparatus to reproduce the required discrete angle increments. With the system used in our experiments, this error is again minimized to about 0.1°. Figure 2.13 shows the results of random angle missettings using simulations. Lineshapes distortions can be seen when angle errors exceed 2°; however, the positions of the singularities remain constant.

2.5.4 Random Phase Error

Equation 2.6 assumes the phase contains terms only due to the dynamic evolution of the spin system under the CSA Hamiltonian. Thus in principle, each VAS FID must be first Fourier transformed into ω space where the zero and first order phase effects may be corrected and then inverse Fourier transformed back into τ space for interpolation. Correct phasing is especially important when a pure-phase (chapter 3) spectrum is desired. If a magnitude calculation is used to obtain the final spectrum, a constant phase applied to all of the FIDs will have no effects on the spectrum, and a first order phase shift due to one or two missing points in the FID will have minimal effects.

References

1. G. M. Clore, and A. M. Gronenborn, Prog. NMR Spectrosc., **23**, 43 (1991).

2. U. Haeberlen, *High Resolution NMR in Solids: Selective Averaging, Advances in Magnetic Resonance, Supplement 1*; Academic, New York, 1976.

3. E. W. Wooten, K. T. Mueller, and A. Pines, Accounts of Chemical Research, **25**, 209 (1992).

4. E. Lipmaa, M. Alla, and T. Turherm, Proceedings of the 19th Congress Ampere, Heidelberg, 1976, p. 241.

5. Y. Yarim-Agaev, P. N. Tutunjian, and J. S. Waugh, J. Magn. Reson., **47**, 51 (1982).

6. T. Nakai, J. Ashida, and T. Terao, J. Chem. Phys., **88**, 6049 (1988).

7. A. Bax, N. M. Szeverenyi, and G. E. Maciel, J. Magn. Reson., **52**, 147 (1983).

8. R. Tycko, G. Dabbagh, and P. A. Mirau, J. Magn. Reson., **85**, 265 (1989).

9. Z. Gan, J. Am. Chem. Soc., **114**, 8307 (1992).

10. J. Z. Hu, D. W. Alderman, C. Ye, R. J. Pugmire, and D. M. Grant, J. Magn. Reson. A, **105**, 82 (1993).

11. L. Frydman, G. C. Chingas, Y. K. Lee, P. J. Grandinetti, M. A. Eastman, G. A. Barrall, and A. Pines, J. Chem. Phys., **97**, 4800 (1992).

12. W. A. Edelstein, J. M. Hutchison, G. Johnson, and T. W. Redpath, Phys. Med. Biol, **25**, 751 (1980).

13. D. B. Twieg, J. Katz, and R. M. Peshock, Magn. Reson. Med., **5**, 32 (1987).

14. D. G. Cory, J. B. Miller, A. N. Garroway, and W. S. Veeman, J. Magn. Reson., **85**, 219 (1989).

15. L. Frydman, J. S. Harwood, D. N. Garnier, and G. C. Chingas, J. Magn. Reson. A, **101**, 240 (1993).

16. C. B. Ahn, J. H. Kim, and Z. H. Cho, IEEE Trans. Med. Imaging, **5**, 2 (1986).

17. G. C. Chingas, L. Frydman, G. A. Barrall, and J. S. Harwood, In *Magnetic Resonance Microscopy Methods and Applications in Materials Science, Agriculture and Biomedicine*VCH: Weinheim, Germany, 1992; p 373.

Chapter 3 Absorption-Mode 2D VACSY Using Linear Prediction with Singular Value Decomposition

As discussed in the previous chapter, one disadvantage of conventional 2D VACSY is that pure-absorption-mode spectra cannot be obtained because of phase-twist artifacts inherent to the experiment; the resulting loss of resolution and lineshape distortions may impede spectral analysis.[1] The removal of such artifacts becomes especially important when there are partially overlapping or a continuous distribution of isotropic shifts, or when accurate lineshape analysis is required as in the study of intermediate dynamics or partial molecular ordering. In this chapter, linear prediction with singular value decomposition (LPSVD) is used to obtain absorption-mode 2D VACSY free of spectral artifacts.

3.1 Phase artifacts in conventional 2D NMR Spectroscopy

Phase artifacts in an NMR spectrum can be seen as truncation effects due to incomplete sampling of the time domain Fourier space. In chapter 1, I discussed some of the problems associated with truncating the 2D time domain signal. Equation 1.55 shows that a pure-absorption Lorentzian lineshape, $a_1(\omega_1)a_2(\omega_2)$, cannot be obtained from a 2D Lorentzian point spread function (PSF), $P(\omega_1,\omega_2)$, when both t_1 and t_2 are truncated for negative times. This corresponds to acquiring data in only one of the four quadrants in the 2D Fourier space (Fig. 3.1b). If, however, half the Fourier space is acquired by truncating the signal only for $t_2 < 0$, $P(\omega_1,\omega_2)$ becomes:

$$\begin{aligned} P(\omega_1,\omega_2) &= 2a_1(\omega_1)[a_2(\omega_2)+id_2(\omega_2)] \\ &= 2[a_1(\omega_1)a_2(\omega_2)+ia_1(\omega_1)d_2(\omega_2)], \end{aligned} \tag{3.1}$$

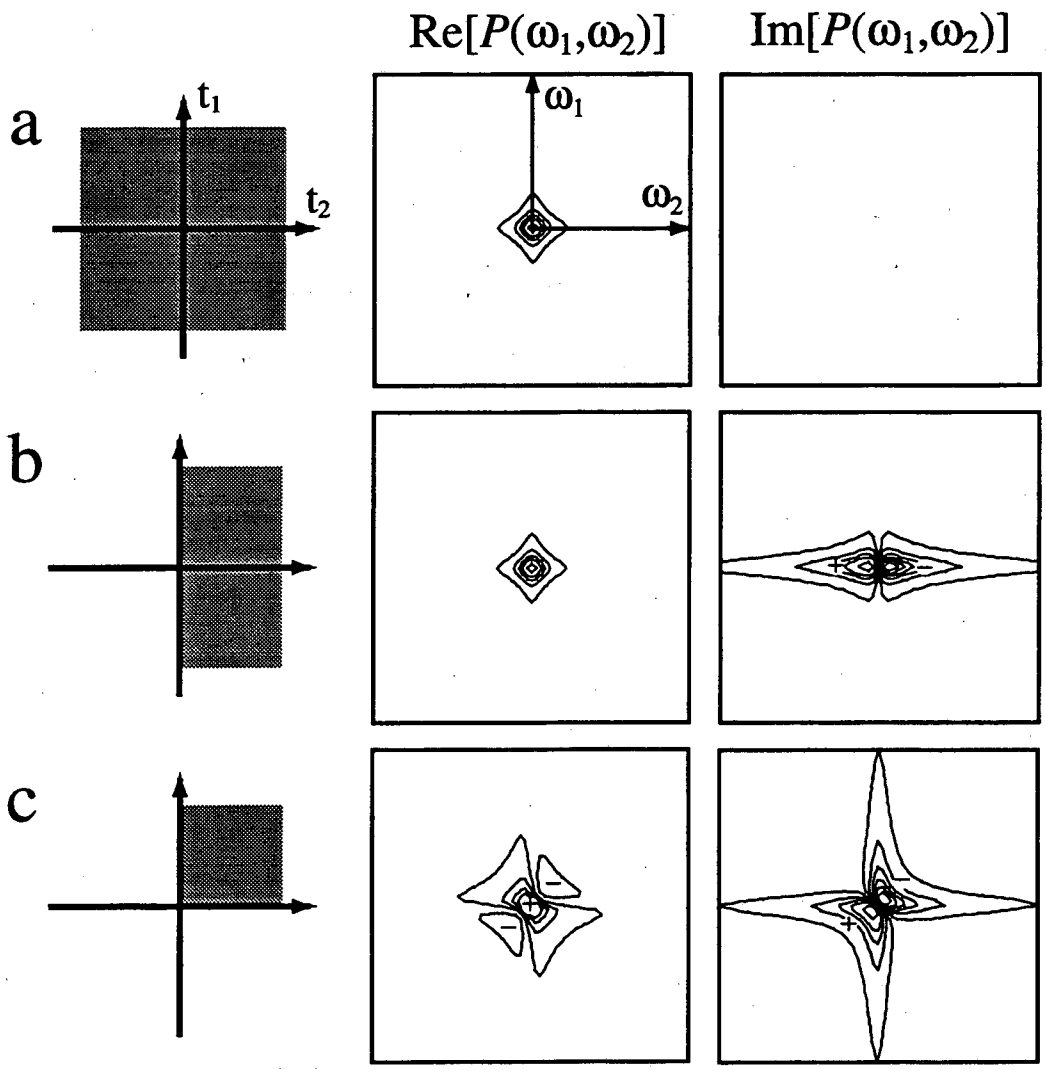

Figure 3.1 2D Lorentzian point spread function (PSF), $P(\omega_1,\omega_2)$. (a) The signal acquired for all four quadrants of the time domain Fourier space. $P(\omega_1,\omega_2)$ is a real absorption 2D Lorentzian lineshape. (b) The signal acquired in two of the four quadrants. The real component of $P(\omega_1,\omega_2)$ remains an absorption Lorentzian lineshape, while the imaginary compontent is a dispersion Lorentzian lineshape. (c) The signal acquired for only one of the quadrants. $P(\omega_1,\omega_2)$ contains a mixture of absorptive and dispersive terms in both the real and imaginary components.

Thus just as in the example of the 1D signal the pure-absorption lineshape, $a_1(\omega_1)a_2(\omega_2)$, can be obtained by sampling only half of the full Fourier space (Fig. 3.1c). This is again due to the redundancy in half of the 2D NMR signal:

$$S(t_1,t_2) = S(-t_1,-t_2)^*. \tag{3.2}$$

Of course similar results may be obtained by truncating the signal along the t_1 dimension rather than t_2. Conventional methods of obtaining pure-absorption-mode 2D spectra include acquiring echoes in either the t_1 or t_2 dimension[2], or acquiring both the +1 and -1 coherence pathways in the t_1 dimension[1,3]. Both these methods ensure that the signal effectively spans two of the four quadrants in the 2D Fourier space.

3.2 Phase Artifacts in 2D VACSY

With the τ space coordinate definitions in Eq. 2.9 two of the quadrants may be partially acquired since $P_2(\cos\theta)$ can take on both positive and negative values. However with the trajectories of the FIDs restricted to the angles given in Eq. 2.11, the two quadrants can never be completely filled with data since that would require $R \to \infty$. Artifacts inherent to the 2D VACSY spectrum are due to data missing from these two quadrants. Consider the PSF, $P(\omega_1,\omega_2)$, for $R = 2$, and $-0.5 \le P_2 \le +0.5$. Since α then ranges from -45° to $+45^\circ$, the total area of the Fourier space spanned by the VACSY signal is equivalent to one quadrant. Thus $P(\omega_1,\omega_2)$, shown in Fig. 3.2a, is similar in form to the PSF of Fig. 3.1c but rotated by 45°. The difference between the two PSFs is due to the star shape of the 2D Lorentzian function. Had we used a cylindrically symmetric lineshape function, such as a 2D Gaussian function, the two PSFs would differ only by the

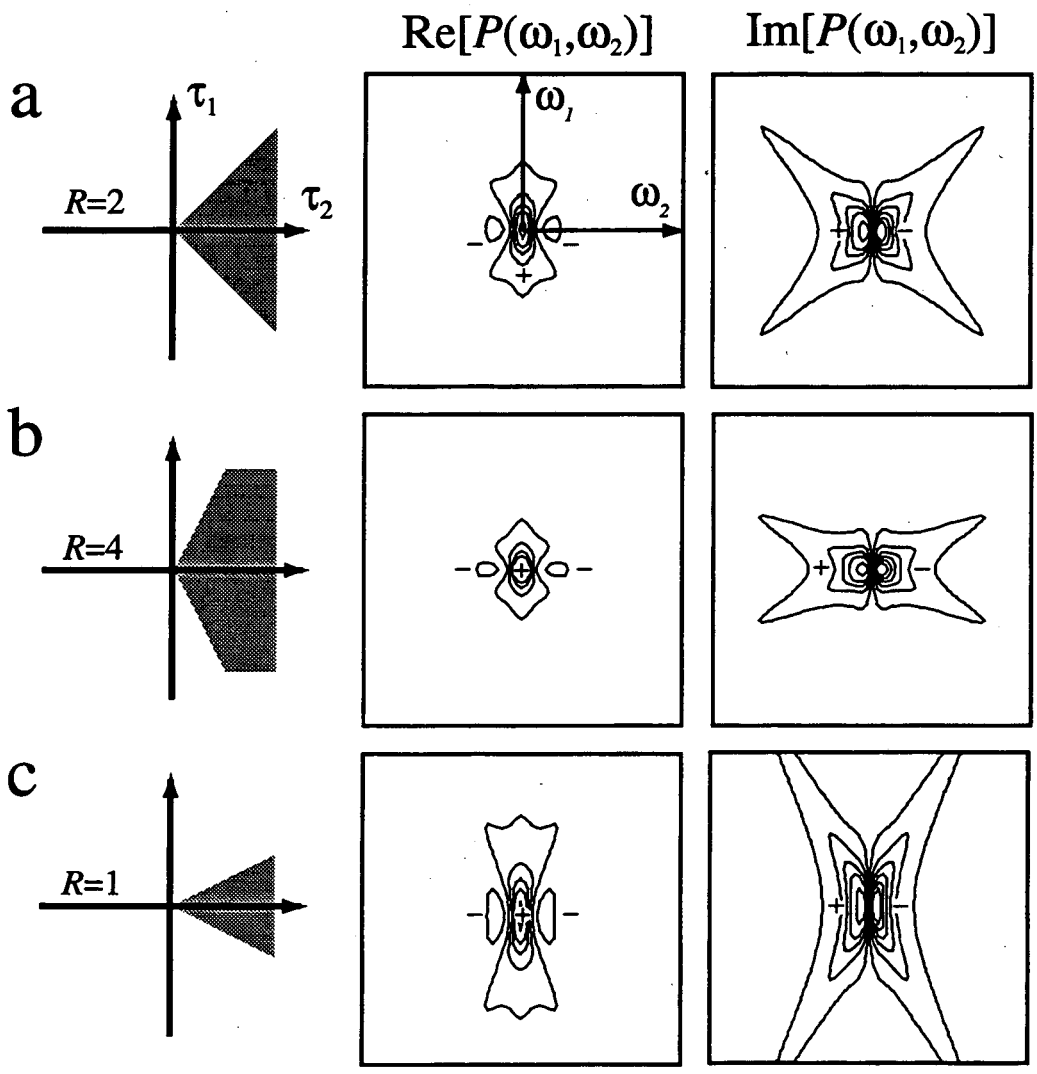

Figure 3.2 2D Lorentzian PSF, $P(\omega_1,\omega_2)$ for 2D VACSY experiments. (a) All functions are caluclated using $-0.5 \leq P_2 \leq +0.5$. The different values for R determine the overall area of the time domain Fourier space covered by the data, as shown by the shaded regions. (a) VACSY PSF with $R = 2$. The total area containing data is equivalent to one quadrant. The VACSY PSF is similar in form to the PSF in Fig. 3.1c but rotated by 45°. (b) VACSY PSF with $R = 4$. The intensity of the ridge artifacts decrease as a larger area of the time domain Fourier space is filled with data. (c) VACSY PSF with $R = 1$. The PSF shows more intense artifact ridges.

rotation. The artifact ridges, become less intense when R increases and a larger area of the Fourier space contains data, as shown in Fig. 3.2b. Unfortunately this is achieved at cost of spectral resolution in the anisotropic dimension, and increased interpolation error. In addition, rearrangement of the FIDs will never completely remove the phase artifacts, since according to the Fourier projection slice theorem (Eq. 1.16), the projection of the 2D VACSY spectrum onto the anisotropic ω_1 axis is equal to the Fourier transformation of the slice along the τ_1 axis. The τ_1 axis, however, contains only one data point at $\tau_1 = 0$, and its Fourier transformation is a constant function. Figure 3.3 shows that a 2D VACSY spectrum must contain negative lobes to cancel out all spectral features in the projection onto the anisotropic ω_1 axis. Similarly, the projection on to the isotropic ω_2 axis will result in a pure absorption MAS spectrum despite the phase artifacts.

These spectral artifacts are unique to 2D VACSY experiments due to the unconventional truncation of the interpolated time domain data. Since the FIDs are placed symmetrically about the τ_2 axis, the slice of the VACSY PSF along the ω_1 axis contains no dispersive terms, while the width of the lineshape varies depending on the level of truncation determined by R (Fig. 3.2). Thus even with a magnitude calculation, each anisotropic pattern appears absorptive provided there is no significant interference of the ridge artifacts from the different isotropic sites in the spectrum. Often these artifacts may be ignored, particularly when the spectrum is dominated by broad anisotropic patterns; since then the artifacts also broaden, and the interference between different sites becomes small. This explains the success of 2D VACSY despite the artifacts inherent to the technique. However, these artifacts can become a serious problem when the spectrum contains closely spaced isotropic shifts with small anisotropies. The ridge artifacts emerging from a narrow site may interfere with the anisotropic patterns of neighboring sites, causing lineshape distortions.

Artifacts in 2D VACSY spectra can be minimized if the missing points in the signal

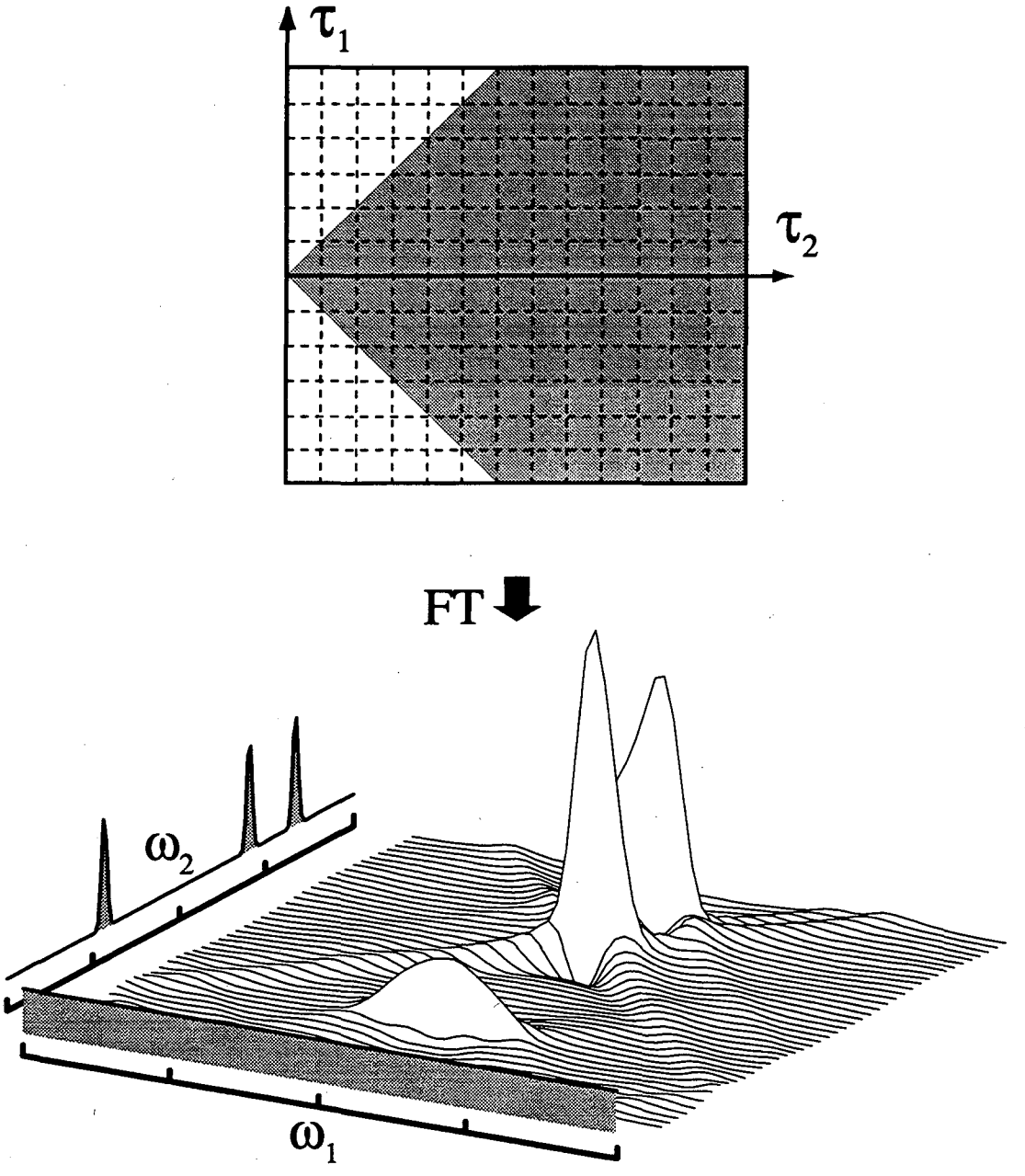

Figure 3.3 Simulation of 2D VACSY spectra. The simulations are made using $R = 2$, $t_d = 200$ μs, $-0.5 \leq P_2 \leq +0.5$ and three sites with the chemical shift tensors: $(\sigma_{xx}, \sigma_{yy}, \sigma_{zz}) = (0.3,1.0,2.3), (-0.5,-0.5,-1.5), (-2.5,-2.0,-1.0)$ (kHz). The area outside the shaded region is set to zero. The 2D spectrum reveals the phase artifacts inherent to the normal 2D VACSY experiment. The projection onto the anisotropic ω_1 axis yields a constant function, while the projection onto the isotropic ω_2 axis yields a pure-absorption MAS spectrum.

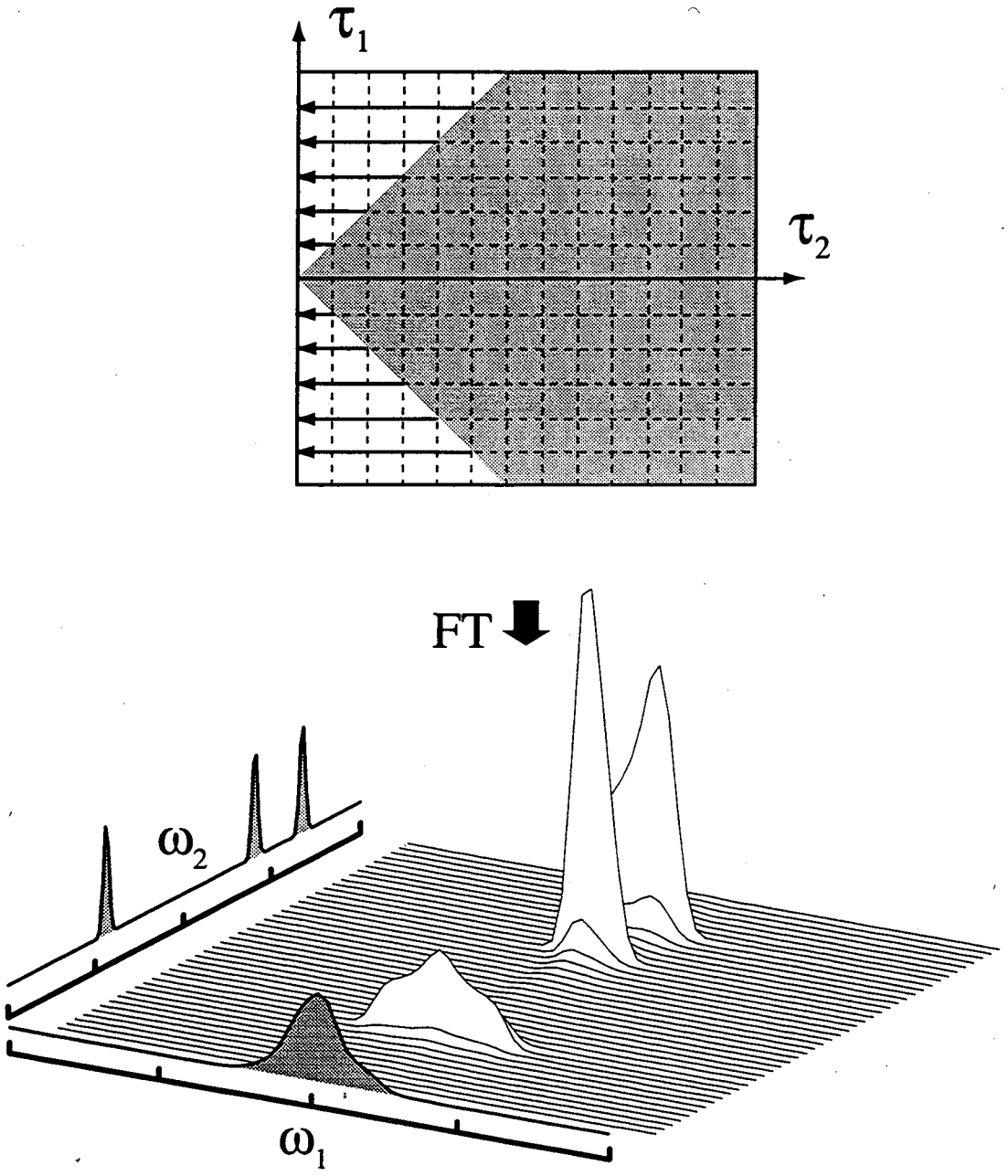

Figure 3.4 2D VACSY spectrum obtained by using LPSVD extrapolation and Fourier transformation of the same time domain data used for Fig. 3.3. The shaded region of τ space corresponds to the interpolated experimental data, while the dark arrows correspond to the extrapolated data for each slice parallel to the τ_2 axis. The phase artifacts are eliminated from the 2D spectrum, and the projection onto the ω_1 axis gives an overlap of the traceless anisotropic patterns.

Fourier space can extrapolated from the experimental data. However, due to the large number of missing data points, the extrapolation technique must maintain accuracy over several cycles of the signal. Linear prediction with singular value decomposition (LPSVD) is one such technique which has been used for extrapolation and spectral estimation in NMR to improve resolution and signal to noise.[4,5] Figure 3.4 shows the spectrum after using LPSVD on the same time domain VACSY data as in Fig. 3.3. The ridge artifacts in Fig. 3.3 are completely removed and the projection onto the anisotropic axis results in the overlap of traceless anisotropic patterns.

The LPSVD method presented in the following sections is due to the original work of Kumaresan and Tufts[6]. The technique was introduced to the NMR community by Barkhuijsen et al.,[4] and has since been widely applied as an extrapolation and spectral estimation technique to improve resolution and SNR. Descriptions of this method may be found in reviews[5,7] and in Kay's book[8] under the heading of "Prony's method".

3.3 Linear Spectral Estimation

3.3.1 Linear Spectral Models

I will first discuss some background theory of linear prediction (LP) and its relationship to other linear spectral models.

A causal discrete linear system can be described by a constant coefficient linear difference equation

$$\sum_{k=0}^{L} b_k y_{n-k} = \sum_{k=0}^{M} c_k x_{n-k}\,, \tag{3.3}$$

where x_n is the discrete input series and y_n is the discrete output series. Both sides of Eq. 3.3 can be recognized as a discrete convolution. Thus by taking the z transform of both sides and using the z transform version of the convolution theorem[9] Eq. 3.3 becomes

$$Y(z)\sum_{k=0}^{L} b_k z^{-k} = X(z)\sum_{k=0}^{M} c_k z^{-k}, \tag{3.4}$$

where z is a complex number, and $X(z)$ and $Y(z)$ are z transforms of the series x_n and y_n. The system function is defined as the ratio

$$H(z) = \frac{Y(z)}{X(z)} = \frac{\sum_{k=0}^{M} c_k z^{-k}}{\sum_{k=0}^{L} b_k z^{-k}}. \tag{3.5}$$

This system function along with an input series, x_n, of white noise forms the most general of the linear spectral estimation models and is called the auto regressive moving average model (ARMA).

Assuming $b_0 = 1$, Eq. 3.3 can be written in terms of a linear filter difference equation for the time series y_n:

$$y_n = -\sum_{k=1}^{L} b_k y_{n-k} + \sum_{k=0}^{M} c_k x_{n-k}. \tag{3.6}$$

One special case of the ARMA model is when $b_k = \delta_{k0}$, then the system function becomes

$$H(z) = \sum_{k=0}^{M} c_k z^{-k}, \tag{3.7}$$

and the time series,

$$y_n = \sum_{k=0}^{M} c_k x_{n-k}, \tag{3.8}$$

now only depends on the input white noise x_n. This model is called the moving average (MA) or the all zero model since the roots of the polynomial in Eq. 3.7 correspond to zeros of the system response function. The MA model has been shown most useful for estimating spectra with broad features.[8,10]

Another special case is when $c_k = \delta_{k0}$; the system response function then becomes

$$H(z) = \frac{1}{1 + \sum_{k=1}^{L} b_k z^{-k}}, \tag{3.9}$$

and the time series equation becomes

$$y_n = -\sum_{k=1}^{L} b_k y_{n-k} + x_n. \tag{3.10}$$

Several names, auto regressive (AR), all poles model, linear prediction, and maximum entropy method, are used to describe this model. The roots of the polynomial in the denominator of Eq. 3.9 correspond to the poles of $H(z)$, making the AR model particularly useful for estimating spectra with sharp narrow features;[8,10] because of this, the AR model has been thoroughly studied in liquid state NMR.

3.3.2 Linear Prediction

Although the different names for the time series in Eq. 3.10 are used interchangeably in the literature, linear prediction gives slightly different interpretation to

the terms in the equation. In forward LP the nth term of the time series is estimated from a linear sum of the previous L output data points

$$y_n^{\mathrm{LP}} = -\sum_{k=1}^{L} b_k^f y_{n-k}. \tag{3.11}$$

The error in the prediction is defined as

$$\varepsilon_n = y_n - y_n^{\mathrm{LP}}, \tag{3.12}$$

so that

$$y_n = -\sum_{k=1}^{L} b_k^f y_{n-k} + \varepsilon_n. \tag{3.13}$$

Clearly if the prediction error ε_n is assumed to be white noise, Eq. 3.13 is identical to Eq. 3.10, and the coefficients for forward LP are identical to the coefficients for the AR model. The LP time series equation may also be set up in backward mode where the nth term of the time series is estimated from the following L data points:

$$y_n = -\sum_{k=1}^{L} b_k^b y_{n+k} + \varepsilon_n. \tag{3.14}$$

It can be shown that the forward and backward LP coefficients are related as [8]

$$b_k^f = \left(b_k^b\right)^*. \tag{3.15}$$

Conventional LP methods involve finding the LP coefficients in Eq. 3.13 or Eq. 3.14 by least-square minimization of the prediction error, ε_n. Up to this point we have not required

our output data, y_n, to have any particular functional form; the only requirement was that the time series lead to a spectrum with sharp features. The LPSVD method presented in the next section, however, uses the backward LP equation to model a signal as a sum of complex exponentials.

3.4 Linear Prediction with Singular Value Decomposition

3.4.1 Backward Linear Prediction Data Matrix

In LPSVD, the data are assumed to have the form

$$y_n = \sum_{m=1}^{M} a_m z_m^{n+d} + w_n \qquad n = 0,1,\ldots,N-1, \tag{3.16}$$

where

$$z_m = \exp\left[\left(i\omega_m - \lambda_m\right)t_d\right]. \tag{3.17}$$

a_m, ω_m, λ_m are the complex amplitude, frequency, and damping factor, respectively, of each exponential term; M is the total number of exponential components; t_d is the dwell time of the time series signal; N is the total number of points in the time series; and d is an arbitrary integer that shifts the time origin of the series. Using the N data points in Eq. 3.16 and the *backward* LP time series (Eq. 3.14), a matrix equation may be constructed as

$$\begin{bmatrix} y_1 & y_2 & \cdots & y_L \\ y_2 & y_3 & \cdots & y_{L+1} \\ \vdots & \vdots & \ddots & \vdots \\ y_{N-L} & y_{N-L+1} & \cdots & y_{N-1} \end{bmatrix} \begin{bmatrix} b_0^b \\ b_1^b \\ \vdots \\ b_{L-1}^b \end{bmatrix} = -\begin{bmatrix} y_0 \\ y_1 \\ \vdots \\ y_{N-L-1} \end{bmatrix}, \tag{3.18}$$

or in short form as

$$\mathbf{Ab} = -\mathbf{h}, \tag{3.19}$$

where $\mathbf{A}$ is an $(N-L)\times L$ data matrix, $\mathbf{h}$ is the data vector with $N-L$ components, and $\mathbf{b}$ is the vector of the backward LP coefficients. The prediction order, L, corresponds to the number of LP coefficients used and is bounded by the condition $M \le L \le N-M$, but is usually set to $0.75N$. [6]

All of the data points y_n in Eq. 3.18 are known; the only unknowns are the backward LP coefficients, b_i^b. These coefficients may be obtained by inverting the matrix $\mathbf{A}$ through singular value decomposition. But first we should note some of the important properties of $\mathbf{A}$. First, all the cross diagonal terms of the matrix are the same; this is referred to as Hankel structure. Next consider the form of $\mathbf{A}$ when the time series in Eq. 3.16 contains only one exponential component and *no noise*:

$$\mathbf{A}_1 = a_1 z^d \begin{bmatrix} z_1 & z_1^2 & \cdots & z_1^L \\ z_1^2 & z_1^3 & \cdots & z_1^{L+1} \\ \vdots & \vdots & \ddots & \vdots \\ z_1^{N-L} & z_1^{N-L+1} & \cdots & z_1^{N-1} \end{bmatrix}. \tag{3.20}$$

A given row, labeled by the index i, differs from its neighboring row, i+1, only by a factor z. Thus $\mathbf{A}_1$ contains only one linearly independent row (the same conclusion can be drawn for the columns), which means $\mathbf{A}_1$ is a rank 1 matrix. Now when the signal is composed of M exponential terms, $\mathbf{A}$ may be written as

$$\mathbf{A} = \sum_{i=1}^{M} a_i \mathbf{A}_i . \tag{3.21}$$

All of the matrices in the summation are rank 1 matrices and have the same form as $\mathbf{A}_1$ in Eq. 3.20. Thus we see that when the signal contains no noise, **A** has a rank equal to the number of sinusoidal components in the signal. When noise is added to the signal, however, the linear dependence of rows and columns in Eq. 3.20 is destroyed and **A** becomes full rank regardless of the number of sinusoidal components:

$$\text{rank}(\mathbf{A}) = \min[L, N-L]. \tag{3.22}$$

However, as long as the SNR is not too low, we can still define an approximate rank which equals M. Thus by assuming the signal is formed of a sum of exponentials, it is still possible to obtain information on the number of exponential terms in the signal through a rank analysis of the backward LP data matrix, **A**.

3.4.2 Singular Value Decomposition

Singular value decomposition not only provides a method for inverting Eq. 3.19 but also for doing a rank analysis of the matrix **A** and separating the parameters due to the signal and those due to noise. Any matrix can be factorized by SVD as[8]

$$\mathbf{A} = \mathbf{U}\begin{bmatrix}\mathbf{S}\\ \mathbf{0}\end{bmatrix}\mathbf{V}^{\dagger}, \tag{3.23}$$

where **U** and **V** are unitary matrices of dimensions $(N-L)\times(N-L)$ and $L\times L$, respectively; "†" denotes Hermitian conjugate; **S** is a diagonal matrix with the singular values, $\{\sigma_k, k = 1,2,\cdots \min(L, N-L)\}$, as its diagonal elements; and **0** is a null matrix. The structure of the matrix multiplication for $L > N-L$ and $N-L > L$ are shown in Fig. 3.5. The number of nonzero singular values is equal to the rank of **A**; thus for noiseless

data, there will only be M nonzero singular values (Fig. 3.6a). When there is noise, **A** becomes full rank; however, if the SNR is not too low, a jump in the magnitude of the singular values can be seen at the Mth singular value (Fig. 3.6b). Thus it is possible to keep only the large singular values, $\{\sigma_k, k = 1,2,\cdots M\}$, and truncate the matrix product in Eq. 3.21 (Fig. 3.7), since the other singular values are those associated with the noise. This allows an overall increase in SNR in the final spectrum. Since M represents the number of exponential components in the time series, if the SNR is high enough, M should be chosen as the total number of peaks in the spectrum; if SNR is lower, M may be chosen as a higher value.[7] Denoting the column vectors of the matrices **U** and **V** by $\{\mathbf{u}_1, \mathbf{u}_2, \cdots, \mathbf{u}_{N-L}\}$ and $\{\mathbf{v}_1, \mathbf{v}_2, \cdots, \mathbf{v}_L\}$, the truncated linear prediction coefficients are

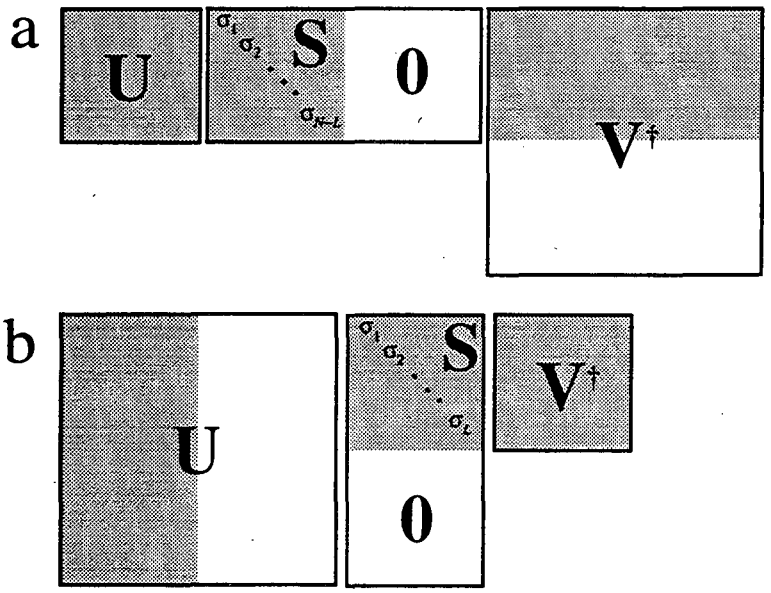

Figure 3.5. Structures of matrix **A** after SVD. **U** and **V** are $(N-L)\times(N-L)$ and $L \times L$ matrixes. The matrix **0** is a null matrix, and the shaded regions contain the matrix elements that contribute to the matrix elements of **A**. (a) When $L > N-L$ the matrix **S** is a diagonal matrix with the singular values $\{\sigma_1, \sigma_2, \ldots, \sigma_{N-L}\}$. (b)When $N-L > L$, the matrix S is a diagonal matrix with the singular values $\{\sigma_1, \sigma_2, \ldots, \sigma_L\}$.

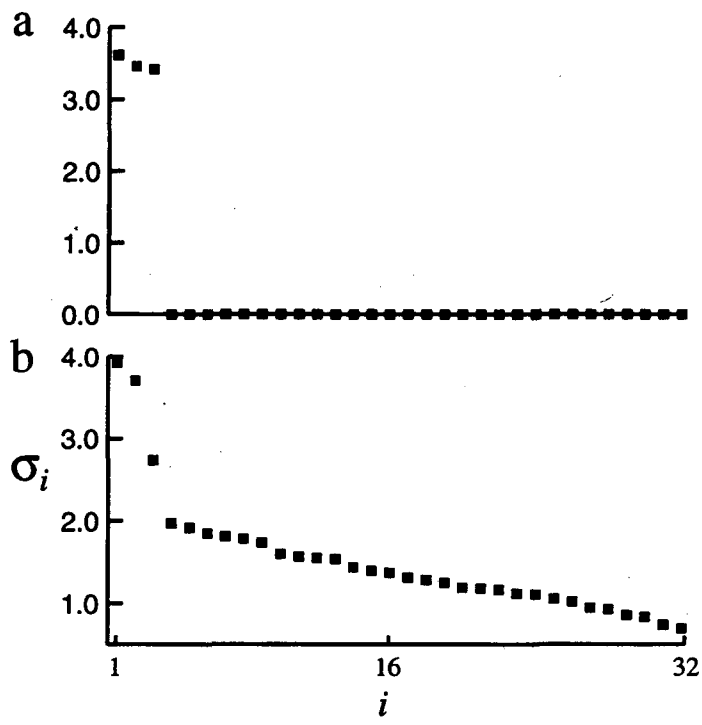

Figure 3.6 The singular values, σ_i, obtained from a simulated time series with three exponential components. A total of 32 σ_i values are shown in descending order of magnitude. (a) Time series with no noise. There are only three nonzero σ_i values. (b) All σ_i values are nonzero; however, a jump in the magnitude of the σ_i can be seen at $i = 3$.

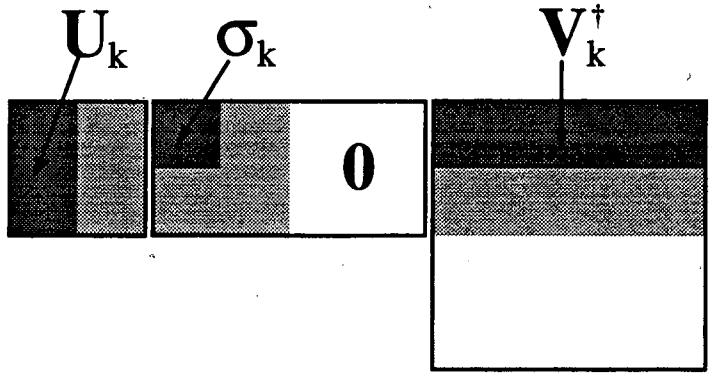

Figure 3.7 The same matrices in Fig. 3.5 have now been truncated at the Mth singular value. The dark shaded regions now contain the matrix elements that will contribute to the elements of matrix **A**.

computed as

$$\mathbf{b} = -\sum_{k=1}^{M} \frac{1}{\sigma_k} (\mathbf{u}_k^{\dagger} \mathbf{a}) \mathbf{v}_k . \tag{3.24}$$

Once the backward LP coefficients are known, the time series in Eq. 3.16 may be extrapolated to the time origin, where $n + d = 0$:

$$y_n = -\sum_{k=1}^{L} b_k y_{n+k} \qquad n = (-1, -2 \ldots - d). \tag{3.25}$$

However, extrapolation at this point would not be making full use of the LPSVD method. A potential increase in the SNR can be obtained by relating the LP coefficients to the signal parameters in Eq. 3.17.

3.4.3 Spectral Parameter Calculation

First we define a complex polynomial,

$$\Phi(z) = \prod_{m=1}^{M} (z - z_m), \tag{3.26}$$

that has M roots at the z_m values of Eq. 3.16. Without loss of generality, the same polynomial may be expanded as a power series,

$$\Phi(z) = \sum_{k=0}^{M} C_k z^{M-k}, \tag{3.27}$$

where C_k are complex coefficients with $C_0 = 1$.

Now by multiplying Eq. 3.16 by C_k (assuming no noise) and shifting the data index from n to $n-k$, we obtain

$$C_k y_{n-k} = C_k \sum_{m=1}^{M} a_m z_m^{n-k+d}, \tag{3.28}$$

and by rearranging terms and summing over the index k,

$$\sum_{k=0}^{M} C_k y_{n-k} = \sum_{m=1}^{M} a_m \sum_{k=0}^{M} C_k z_m^{n-k+d}. \tag{3.29}$$

With the substitution $z_m^{n-k+d} = z_m^{n+d-M} z_m^{M-k}$, Eq. 3.29 becomes

$$\sum_{k=0}^{M} C_k y_{n-k} = \sum_{m=1}^{M} a_m z_m^{n+d-M} \sum_{k=0}^{M} C_k z_m^{M-k}, \tag{3.30}$$

but the last summation is Eq. 3.27 solved at its roots; thus the RHS is equal to zero,

$$\sum_{k=0}^{M} C_k y_{n-k} = 0. \tag{3.31}$$

Using $C_0 = 1$, we obtain the equation for *forward* linear prediction,

$$y_n = -\sum_{k=1}^{M} C_k y_{n-k}. \tag{3.32}$$

Thus the complex coefficients in Eq. 3.27 are the *forward* LP coefficients of the time series.

To calculate the spectral parameters, the backward LP coefficients, b_m^b must first be calculated from Eq. 3.24; then the M roots of the polynomial

$$\Phi(z) = \sum_{m=1}^{M} \left(b_m^b\right)^* z^{M-m} \tag{3.33}$$

must be solved. When the linear prediction equation is written in backward mode (as opposed to forward mode) the M roots of the polynomial corresponding to the signal fall outside of the complex unit circle, whereas the $L-M$ extraneous roots fall inside.[6] This allows for easy separation of the desired signal roots. Each signal root z_m is related to the spectral parameters λ_m and ω_m by

$$\begin{aligned} \lambda_m &= \ln|z_m|/t_d \\ \omega_m &= \tan^{-1}\left[\frac{\mathrm{Im}(z_m)}{\mathrm{Re}(z_m)}\right]\frac{1}{t_d}. \end{aligned} \tag{3.34}$$

The rest of the spectral parameters contained in the complex amplitudes, a_m, can be obtained by substituting λ_m and ω_m into Eq. 3.18.

3.5 LPSVD on VACSY Data

The 2D VACSY signal after interpolation may be written in the same discrete time-series form as Eq. 3.16:

$$S(n_1, n_2) = \sum_{m=1}^{M} a_{m,n_1} \exp\left[i\omega_m^i t_d n_2 + \lambda_m\right], \tag{3.35}$$

where

$$a_{m,n_1} = \int_{-\infty}^{\infty} I(\omega_m^i, \omega^a) \exp\left[i\omega^a t_d n_1 / R\right] d\omega^a . \tag{3.36}$$

Here, $I(\omega_m^i, \omega^a)$ is the isotropic-anisotropic correlation spectrum, n_1 and n_2 specify the discrete time increments in the τ_1 and τ_2 dimensions, and M is the total number of isotropic resonances. Since the VACSY spectrum correlates isotropic frequencies with distributions of anisotropic frequencies, the time domain signal can be considered as a sum of discrete exponentials only along the τ_2 dimension. Thus LPSVD must be applied to each slice parallel to the τ_2 axis to extrapolate the missing data or to completely reconstruct the FID through the calculated spectral parameters, thereby completely filling two of the quadrants of the time domain Fourier space. Figure 3.4 shows the schematic for the LPSVD procedure.

The advantages of using LPSVD with experimental 2D VACSY data are demonstrated by ^{13}C NMR of solid lauric acid. Lauric acid poses a particularly difficult problem for the VACSY technique due to the combination of a large spectral width and small chemical shift anisotropies of the aliphatic sites. Four isotropic resonances are completely resolved in the MAS spectrum which contains the carboxyl resonance at 181 ppm and three aliphatic resonances centered about 24 ppm (Fig 3.8). The assignments shown in the figure were based on liquid state ^{13}C NMR spectra.[11] Thirty-one VAS FIDs were acquired, each containing 512 points and using angles restricted to the range $-0.5 \le P_2(\cos\theta) \le 0.5$. After interpolation onto a 128x512 grid, LPSVD computations were carried out with MATLAB-SGI (version 4.0), using matrix software developed by the LINPACK[12] and EISPACK[13] projects. The signal parameters for each anisotropic slice were obtained using $N = 512 + n_1 - 65$ for $n_1 \le 65$ and $N = 512 - n_1 + 65$ for $n_1 > 65$ and L=284. Figure 3.9 shows a graph of the singular values obtained for different slices parallel to the τ_2 axis. As the SNR decreases for slices further away from the MAS slice ($n_1 = 65$), the singular values due to noise and those due to the signal become harder to discriminate. Thus the profile of the M values (Fig. 3.10) used in the computations to

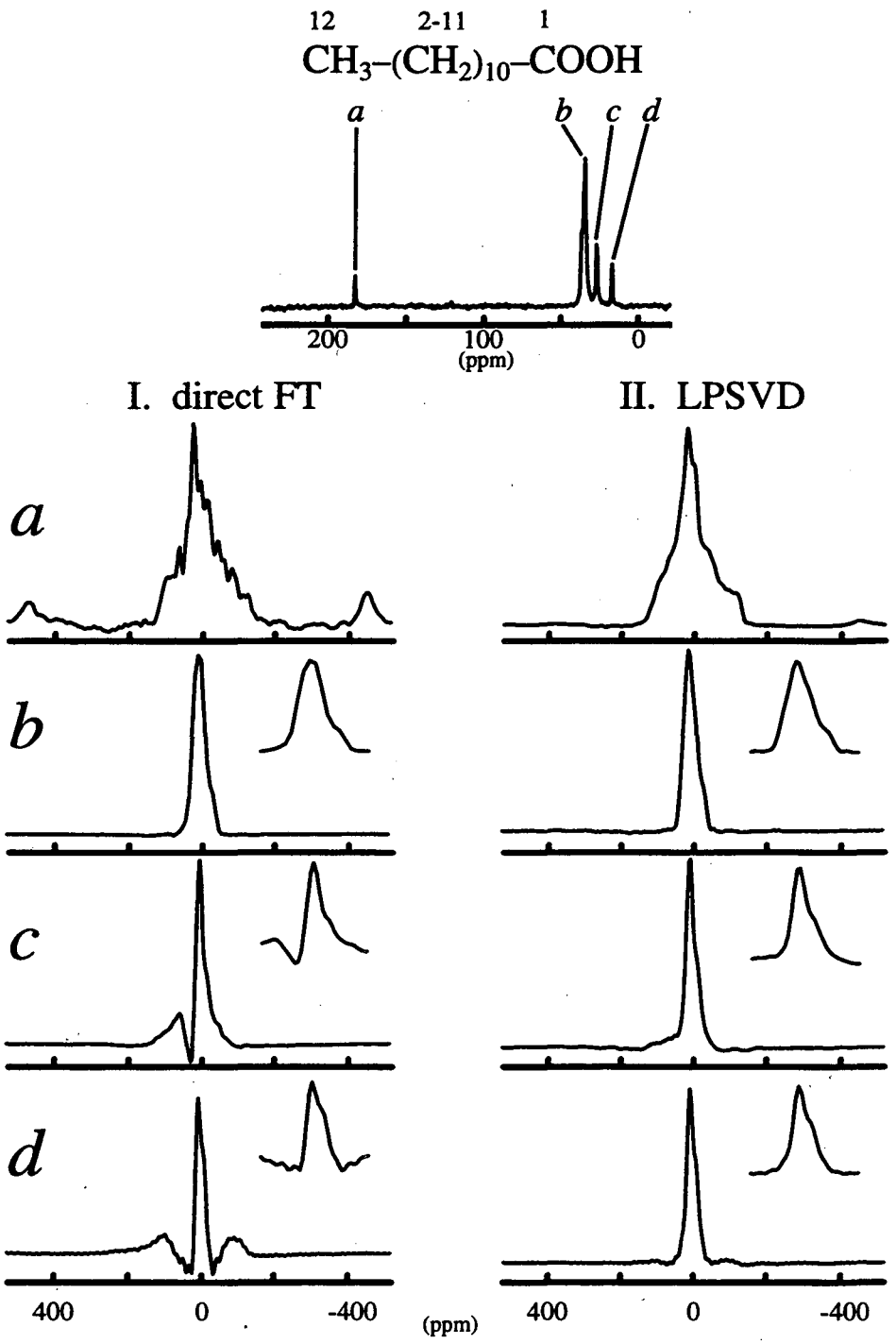

Figure 3.8 Isotropic and anisotropic spectra obtained from a 2D VACSY spectrum of lauric acid. The MAS spectrum shows four completely resolved sites. Site *a* corresponds to the carboxyl carbon 1; site *b* to carbons 4-10, and 2; site *c*, to carbons 3 and 11; and site *d*, to the methyl carbon 12. The anisotropic patterns in column I were obtained by Fourier transforming the interpolated data with zeroes outside the region spanned by the FIDs. The anisotropic patterns in column II were obtained, using LPSVD to construct a data set that completely spanned two of the four quadrants in the time domain Fourier space.

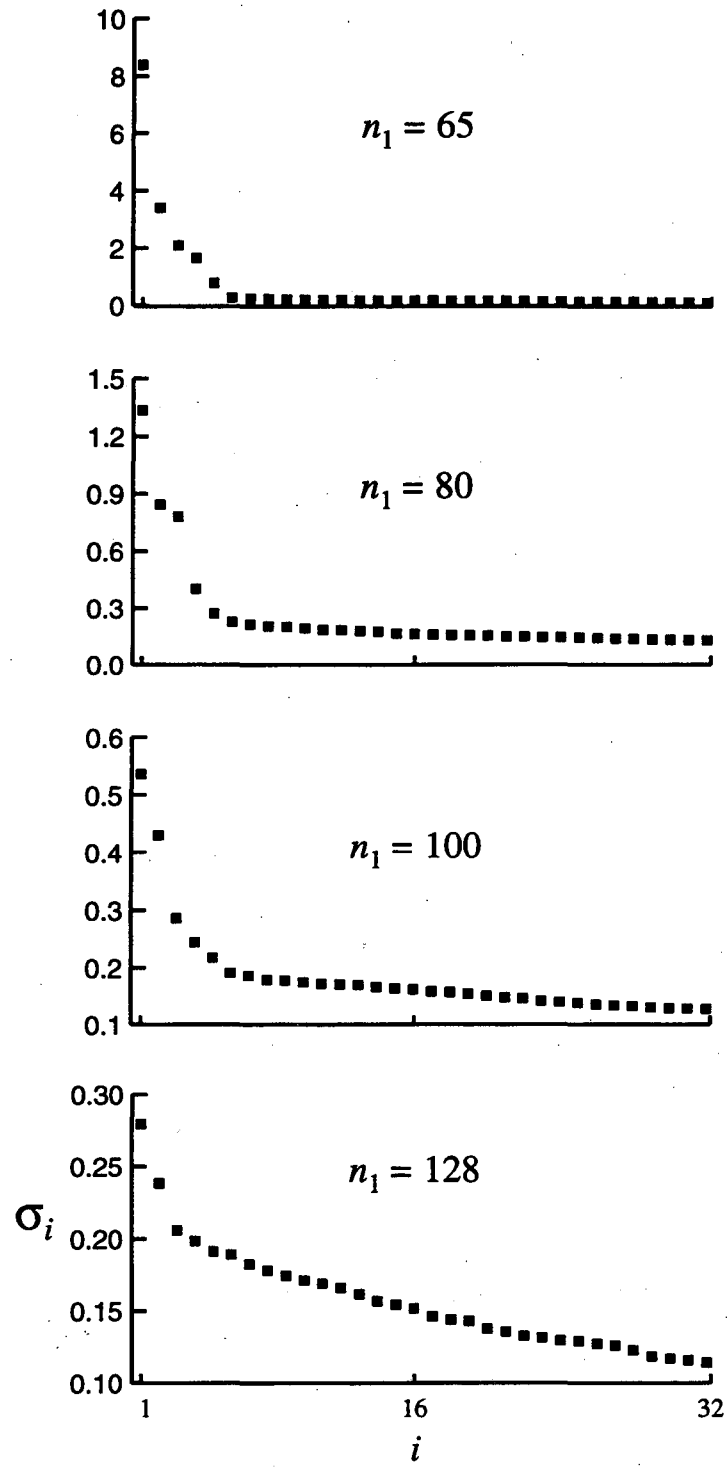

Figure 3.9 Singular values, σ_i, from the experimental lauric acid data. 32 singular values are shown for each slice in descending order of magnitude. n_1 labels the time domain slices taken parallel to the τ_2 axis. $n_1 = 65$ corresponds to the MAS FID at $\tau_1 = 0$.

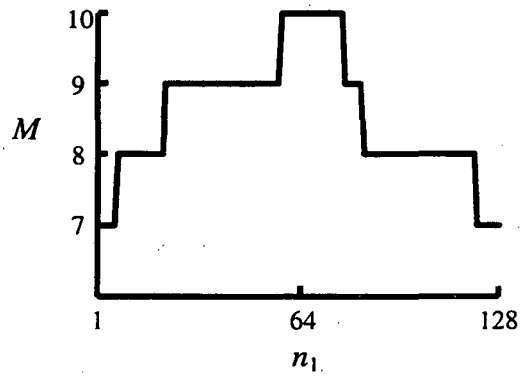

Figure 3.10. M values used for each of the n_1 slices parallel to the τ_2 axis in processing the lauric acid VACSY data.

truncate the matrix equation 3.23, was determined empirically by comparing Fourier transformations of several slices at different n_1 values with and without LPSVD to ensure that the LPSVD method was always generating all of the isotropic peaks.

Figure 3.8 shows the anisotropic patterns obtained from 2D VACSY spectra processed using direct Fourier transformation (Column I) and including LPSVD extrapolation (Column II). Fourier transformation directly after interpolation results in severe artifact interference among the aliphatic carbon resonances *b*, *c*, and *d*, making examination of individual anisotropic patterns difficult. The ridge artifacts from site *b* can even be seen in the anisotropic spectrum of the carboxyl carbon, appearing as lobes on both sides of the powder pattern. These spectral artifacts are significantly reduced using LPSVD as shown in Column II. LPSVD also has the effect of smoothing spectral features[14] as seen in the carboxyl powder pattern, *a*. Comparable results (not shown) have also been obtained using the commercial LPSVD routine in the FELIX data processing software (Biosym Technologies). Further analysis and interpretation of the anisotropic lineshapes of lauric acid in an inclusion compound will be presented elsewhere.[15]

3.6 Conclusion

In summary, 2D VACSY artifacts are seen to have the same origin as the phase-twist artifacts observed in conventional 2D NMR experiments. These artifacts may be removed by using linear prediction with singular value decomposition (LPSVD) to fill in missing data in the time domain Fourier space. The resulting pure-absorption spectrum eliminates resolution problems associated with closely spaced isotropic lines and interference of phase artifacts. This should allow 2D VACSY to be applied to investigate a wider range of complex systems. Similar spectral analysis methods may be applicable to the 3D VACSY exchange experiments, discussed in chapter 5, that also suffer from artifacts due to holes in the time domain Fourier space .

References

1. D. J. States, R. A. Haberkorn, and D. J. Ruben, J. Magn. Reson., **48**, 286 (1982).

2. A. Bax, A. F. Mehlkopf, and J. Smidt, J. Magn. Reson., **35**, 373 (1979).

3. J. Keeler, and D. Neuhaus, J. Magn. Reson., 454 (1985).

4. H. Barkhuijsen, R. DeBeer, W. M. M. J. Bovee, and D. VanOrmondt, J. Magn. Reson., **61**, 465 (1985).

5. D. S. Stephenson, Prog. NMR Spectrosc., **20**, 515 (1988).

6. R. Kumaresan, and D. W. Tufts, IEEE Trans. Acoust. Speech Signal Process, **ASSP-30**, 833 (1982).

7. R. DeBeer, D. VanOrmondt, W. W. F. Pijnappel, and J. W. C. VanDerVeen, Isr. J. Chem., **28**, 249 (1988).

8. S. M. Kay, *Modern Spectral Estimation Theory and Application*; Prentice Hall, Englewood Cliffs, New Jersey, 1988.

9. R. N. Bracewell, *Fourier Transform and its Applications*; McGraw-Hill, New York, 1986.

10. S. L. Marple, *Digital Spectal Analysis with Applications*; Prentice Hall, Englewood Cliffs, New Jersey, 1987.

11. E. Bengsch, B. Perly, C. Deleuze, and A. Valero, J. Magn. Reson., **68**, 1 (1986).

12. J. J. Dongarra, C. B. Moler, J. R. Bunch, and G. W. Steward, *LINPACK User's Guide*; SIAM, Philadelphia, 1979.

13. B. T. Smith, J. M. Boyle, J. J. Dongarra, B. S. Garbow, Y. Ikebe, V. C. Klema, and C. B. Moler, *Matrix Eigensystem Routines-EISPACK Guide, Lecture Notes in Computer Science*; Springer-Verlag, Berlin, 1977; Vol. 6.

14. T. Yu, IEE proceedings, **137**, 192 (1990).

15. R. L. Vold, G. L. Hoatson, and Y. K. Lee, in preparation,

Chapter 4 2D VACSY Applications

In chapter 2, resolved powder patterns were used to extract the CSA tensor values for each chemical site. However, analysis of CSA patterns may provide further information about the microscopic structure and dynamics of molecules. In this chapter two additional applications of 2D VACSY for the study of intermediate dynamics and molecular ordering will be explored.

4.1 Intermediate dynamics

In solid state NMR, there are three motional time regimes where dynamical information may be obtained from the spectrum. First, in the "fast" regime, where the correlation time, τ_c, is of the order of the Larmor frequency, measurements of the spin-lattice relaxation times are useful for determining motional rates. Second, in the "intermediate" regime, where τ_c is of the order of the inverse width of the anisotropic frequency distribution, $\tau_c \sim 1/\Delta\omega^a$, the spectral lineshapes become altered; in favorable cases motional information may be extracted by computer-simulated fits to the anisotropic patterns.[1] Finally, in the "slow" regime, where $\tau_c >> 1/\Delta\omega^a$, a 2D exchange experiment can be used to correlate the molecular orientations at two different times.

For both the intermediate and slow regimes, the motional information is contained in the anisotropic component of the spectrum. Thus studies of either time regimes suffer from resolution problems due to overlapping spectral patterns unless an isotropic chemical shift dimension is added to the experiments to separate the patterns from each chemical site. The application of the VACSY technique in 3D experiments to study slow molecular motion will be discussed in chapter 5. The rest of this section will be concerned with the application of 2D VACSY to study intermediate dynamics.

4.1.1 Theory

With the condition for intermediate motion, $\tau_c \sim 1/\Delta\omega^a$, a significant amount of molecular reorientation occurs while the signal is being acquired. This motion alters the anisotropic component of the chemical shift frequency (Eq. 2.5) and will create distortion in the powder patterns shown in chapter 2. These distortions are dependent on the dynamics of the system; thus by using computer simulations, the dynamical information may be extracted from the lineshapes.

The Chemical Shift Frequency for Intermediate Motion

In order to the describe the chemical shift frequency for a system undergoing intermediate motion, it is helpful to define coordinate frames with respect to the molecule. The frames Mol_1 and Mol_2, shown in Fig. 4.1 correspond to the frames fixed with respect to the molecule before and after the exchange reorientation. Using the addition theorem of Wigner rotation matrices (Eq. 1.39), the coordinate transformation from the chemical shift PAS frame to the lab frame may be broken down into consecutive rotations

$$D^2_{m0}(\Omega) = \sum_{\substack{m,m',\\ m'',m'''}} D^2_{mm'}(\Omega_1) D^2_{m'm''}(\Omega_2) D^2_{m''m'''}(\Omega_3) D^2_{m'''0}(\omega_r t, \theta)\rho_m , \tag{4.1}$$

which simplifies under fast sample spinning to

$$D^2_{m0}(\Omega) = P_2(\cos\theta) \sum_{\substack{m,m',\\ m''}} D^2_{mm'}(\Omega_1) D^2_{m'm''}(\Omega_2) D^2_{m''0}(\Omega_3)\rho_m . \tag{4.2}$$

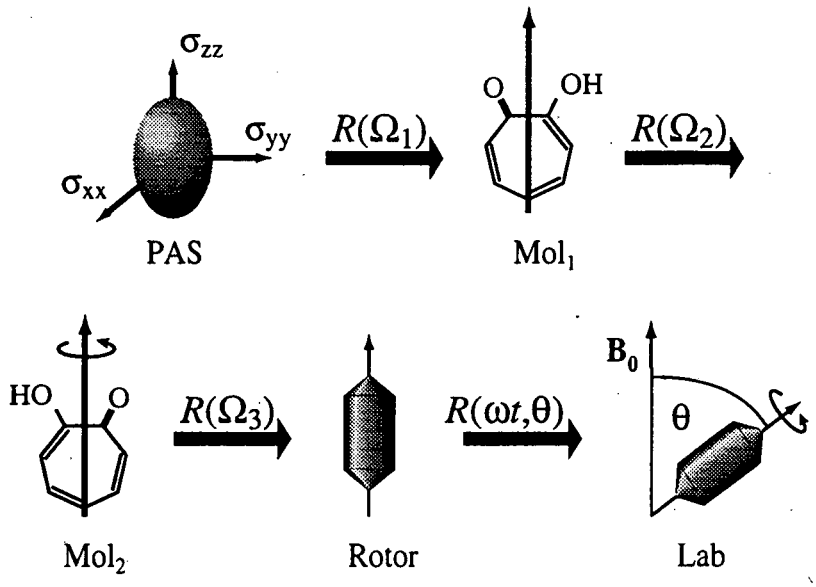

Figure 4.1. Coordinate transformations rotating the coordinate axes from the CSA PAS frame to the lab frame. Mol_1 and Mol_2 frames define the coordinate axis with respect to the molecule before and after reorientation. R represents the rotation transformations from one coordinate frame to the next, and Ω_i are the sets of Euler angles relating the coordinate systems.

Figure 4.1 shows the coordinate rotations defined for the sets of Euler angles Ω_1, Ω_2, and Ω_3. From Eq. 1.42, the chemical shift (CS) frequency may be written as

$$\omega_{CS} = \omega^i + \sqrt{\tfrac{2}{3}}\omega_0 P_2(\theta) \sum_{\substack{m,m',\\ m''}} D^2_{mm'}(\Omega_1) D^2_{m'm''}(\Omega_2) D^2_{m''0}(\Omega_3) \rho_m . \tag{4.3}$$

If the molecular reorientation only occurs about one axis, the frequency equation may be simplified as

$$\begin{aligned} \omega_{CS} &= \omega^i + \sqrt{\tfrac{2}{3}}\omega_0 P_2(\theta) \sum_{m,m'} D^2_{mm'}(\Omega_1) \exp[im'\alpha_2] D^2_{m'0}(\Omega_3) \rho_m \\ &= \omega^i + \sqrt{\tfrac{2}{3}}\omega_0 P_2(\theta) \sum_{m,m'} d^2_{mm'}(\beta_1) d^2_{m'0}(\beta_3) \exp\left[im\alpha_1 + im'(\gamma_1 + \alpha_2 + \alpha_3)\right] \rho_m . \end{aligned} \tag{4.4}$$

The angles α_1 and β_1 determine the orientation of the PAS frame with respect to the molecule, α_2 is the molecular reorientation angle, and α_3 and β_3 determine the orientation of the molecule with respect to the rotor frame and are the powder average angles used in the spectral simulations.

As in the examples from the previous chapter, the term for the anisotropic frequency in Eq. 4.4 is identical to the frequency for a static sample except for the $P_2(\cos\theta)$ scaling factor. Thus the phase due to chemical shift evolution may again be written as

$$\Phi(t) = \omega^i t + P_2(\cos\theta)\omega^a t, \tag{4.5}$$

where

$$\omega^a = \sqrt{\tfrac{2}{3}}\omega_\circ \sum_{m,m'} d^2_{mm'}(\beta_1) d^2_{m'0}(\beta_3) \exp[im\alpha_1] \exp[im'(\gamma_1 + \alpha_2 + \alpha_3)]\rho_m . \tag{4.6}$$

Since the width of the anisotropic spectral pattern is scaled by a constant $P_2(\cos\theta)$ term, the same 2D VACSY technique described in the previous chapters to separate the isotropic and anisotropic interactions also applies to systems undergoing intermediate motion.

Signal for Intermediate Exchange

Even though the chemical shift frequency has the same form as in the examples from the previous chapter, when the frequency is modulated by molecular motion during signal detection, the frequency gains a time dependence and the equation for the signal is no longer given by Eq. 1.30. The complete signal now becomes[2]

$$S(t) = \sum_\alpha S_\alpha(t), \tag{4.7}$$

where $S_\alpha(t)$ is the signal component with a well define frequency ω_α at time *t*.

A functional form for $S_\alpha(t)$ can be obtained by assuming the molecular reorientation to be a stationary Markov process where the molecular orientation at any given time *t* is independent of the previous orientations.[2] With this condition, the probability that the system will be evolving with a frequency ω_2 at a time $t+\Delta t$ given that it was evolving with ω_1 at time *t* can be written for small Δt as

$$P(\omega_1|\omega_2;\Delta t) = \delta_{\omega_1,\omega_2} + \pi_{\omega_1,\omega_2}\Delta t, \tag{4.8}$$

where

$$\delta_{\omega_1,\omega_2} = \begin{cases} 1, & \omega_1 = \omega_2 \\ 0, & \omega_1 \neq \omega_2 \end{cases}, \tag{4.9}$$

and π_{ω_1,ω_2} is the exchange matrix describing the jumping process between the frequencies. The signal from each frequency component may then be described by

$$S_\beta(t+\Delta t) = \exp[i\omega_\beta \Delta t]\sum_\alpha S_\alpha(t)P(\omega_\alpha|\omega_\beta;\Delta t). \tag{4.10}$$

For small Δt,

$$\exp[i\omega_\beta \Delta t] \approx 1 + i\omega_\beta \Delta t. \tag{4.11}$$

Substituting Eqs 4.8 and 4.11 into Eq. 4.10,

$$S_\beta(t+\Delta t) = S_\beta(t+\Delta t)(1+i\omega_\beta\Delta t) + \Delta t\sum_\alpha \pi_{\omega_\alpha,\omega_\beta}S_\alpha(t), \tag{4.12}$$

which may be written in differential form as

$$\frac{dS_\beta}{dt} = i\omega_\beta S_\beta + \sum_\alpha \pi_{\omega_\alpha,\omega_\beta} S_\alpha(t) \tag{4.13}$$

or in terms of matrices as

$$\frac{d\mathbf{S}}{dt} = \mathbf{S}\left(i\tilde{\omega} + \tilde{\pi}\right), \tag{4.14}$$

where $\tilde{\omega}$ is a diagonal matrix with elements ω_α, $\tilde{\pi}$ is the exchange matrix with elements $\pi_{\omega_\alpha,\omega_\beta}$, and $\mathbf{S}$ is the signal vector with components $S_\alpha(t)$. Equation 4.14 may be integrated, and using Eq. 4.7, the complete signal becomes

$$S(t) = \mathbf{1}\cdot\exp\left[i\left(\tilde{\omega} + \tilde{\pi}\right)t\right]\cdot\mathbf{S}(0), \tag{4.15}$$

where $\mathbf{1}$ is the unit matrix, and $\mathbf{S}(0)$ is the vector representing the relative contributions by each signal components to the total signal at $t = 0$. By diagonalizing the exponential phase in Eq. 4.15, the signal may be written as

$$\begin{aligned} S(t) &= \mathbf{1}\cdot\mathbf{A}\cdot\exp[i\mathbf{D}t]\cdot\mathbf{A}^{-1}\cdot\mathbf{S}(0) \\ &= \sum_j (\mathbf{1}\cdot\mathbf{A})_j \exp\left[iD_j t\right]\left(\mathbf{1}\cdot\mathbf{A}^{-1}\right)_j, \end{aligned} \tag{4.16}$$

where $\mathbf{D}$ is the diagonal eigenvalue matrix, D_j are the eigenvalues, and

$$\mathbf{A}^{-1}\cdot\left(i\tilde{\omega} + \tilde{\pi}\right)\cdot\mathbf{A} = \mathbf{D}. \tag{4.17}$$

Signal for Two Site Exchange

In the example of two site exchange, the signal (Eq. 4.16) may be readily written in analytical form. Assuming equal rate constants for going from one site to the other, the exponential phase becomes

$$i\tilde{\omega} + \tilde{\pi} = i\begin{pmatrix} \omega_1 & 0 \\ 0 & \omega_2 \end{pmatrix} + k\begin{pmatrix} -½ & ½ \\ ½ & -½ \end{pmatrix}. \tag{4.18}$$

Diagonalizing Eq. 4.18, we obtain the eigen values

$$\begin{aligned} D_1 &= -\tfrac{1}{2}C - k + i\tfrac{1}{2}(\omega_1 + \omega_2) \\ D_2 &= \tfrac{1}{2}C - k + i\tfrac{1}{2}(\omega_1 + \omega_2) \end{aligned} \tag{4.19}$$

and matrices

$$\begin{aligned} \mathbf{A} &= \begin{pmatrix} \dfrac{-2k}{C + i(\omega_1 - \omega_2)} & \dfrac{-2k}{-C + i(\omega_1 - \omega_2)} \\ 1 & 1 \end{pmatrix} \\ \mathbf{A}^{-1} &= \begin{pmatrix} -\dfrac{k}{C} & \dfrac{-2k^2}{-C^2 + iC(\omega_1 - \omega_2)} \\ \dfrac{k}{C} & \dfrac{2k^2}{C^2 + iC(\omega_1 - \omega_2)} \end{pmatrix}, \end{aligned} \tag{4.20}$$

where

$$C = \left(4k^2 - \omega_1^{\,2} + 2\omega_1\omega_2 - \omega_2^{\,2}\right)^{½}. \tag{4.21}$$

The VAS signal for two site exchange may now be obtained by substituting Eqs. 4.19 and 4.20 into Eq. 4.16 and by using the chemical shift frequency, Eq. 4.5 with $\alpha_2 = 0°,\ 180°$ for ω_1 and ω_2.

There is however an important difference between the anisotropic lineshapes obtained from a VAS signal and the lineshapes obtained for the same dynamical system under static conditions. The distortions in the powder patterns depend on the jump rates relative to the width of the patterns. Thus as the angle is varied in the VACSY experiment and the width of the anisotropy is reduced due to the $P_2(\cos\theta)$ scaling factor, the distortion in the lineshape due to molecular motion becomes more prominent. Figure 4.2 shows the changes in the simulated anisotropic lineshapes of a rapidly spinning dimethylsulfone (discussed below) at various different values of $P_2(\cos\theta)$. Since the lineshape changes at the different angles θ in the 2D VACSY experiment, the overall anisotropic patterns obtained after interpolation and Fourier transformation will be a weighted average of the anisotropic patterns at the different angles. Despite these differences, the dynamical information may be obtained from VACSY anisotropic lineshapes through comparisons with simulations as long as the entire set of VAS FIDs are simulated and processed in the same manner as the experimental data.

4.1.2 Experimental

All the Experiments in this section were performed by Dr. L. Frydman and S. Vallabhaneni at the University of Illinois at Chicago. Samples of dimethylsulfone (DMS) and tyrosine ethyl ester were obtained from Aldrich. The experiments were carried out on a home-built spectrometer with a ^{13}C Larmor frequency of 75.78 MHz. The probe and variable temperature system are described in chapter 6. High-power decoupling fields are

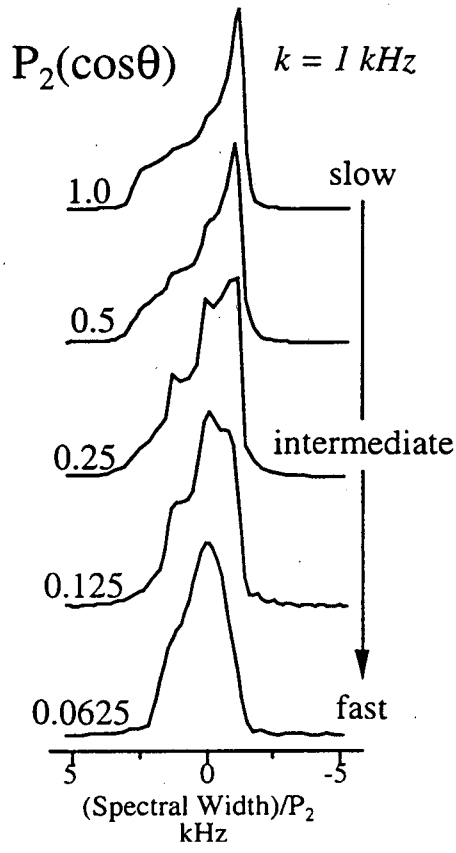

Figure 4.2. Variations in the simulated anisotropic lineshapes of dimethylsulfone under rapid sample rotation at various different $P_2(\cos\theta)$ values with an exchange rate of 1 kHz.

essential for retrieving undistorted CSA lineshapes from protonated solids reorienting in the intermediate exchange regime. Hartmann-Hahn matching conditions were therefore achieved using over 300 W in both the transmitter and decoupler channels, corresponding to proton nutation rates ranging between 93 and 55 kHz depending on the rotation axis angle. In the DMS VACSY experiment, FIDs were acquired at 31 different angles within the range $-0.5 \le P_2(\cos\theta) \le 0.5$. The tyrosine ethyl ester VACSY experiment used the same number of FIDs but the range in angles were reduced to $-0.25 \le P_2(\cos\theta) \le 0.25$. Data sets for both samples were interpolated onto a 256×64 time domain grid before being Fourier transformed.

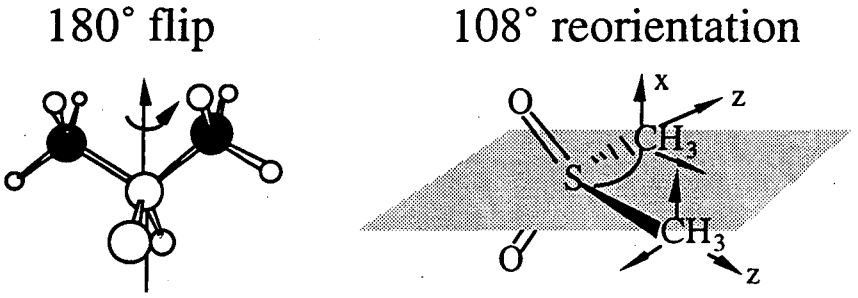

Figure 4.3. Reorientation of solid DMS. 180° flips along the main molecular symmetry axis exchange the relative orientations of the carbon sites (filled circles, left) at temperature dependent rates $k = 5.44 \times 10^{13} \exp(-7601/T)$ Hz. These molecular motions result in mutual 108° rotations of the ^{13}C chemical shift tensors around their x-axes, as shown on the right.

4.1.3 Results

Dimethylsulfone

Dimethylsulfone (DMS) was used as a test study to examine the potential usefulness of 2D VACSY for investigating molecular motions in the intermediate regime. DMS was initially studied by Solum *et al.*[3] and has since served extensively as model system for dynamic solid-state NMR analyses. DMS possesses two chemically equivalent carbon sites; thus the anisotropic CSA pattern can be obtained simply from a static experiment without problems of resolution due to overlapping patterns, allowing direct comparison of static and VACSY anisotropic patterns. With increasing temperatures, DMS undergoes 180° reorientations about its main symmetry axis (Fig. 4.3), producing well-defined changes in the ^{13}C NMR powder lineshapes. From the analysis of these lineshapes, both the kinetics and geometries of the reorientation process have been accurately extracted, providing a model case of intermediate dynamics where all the parameters involved are known.

Figure 4.4 shows a series of 2D VACSY spectra of DMS as a function of temperature. All spectra reveal a high-resolution isotropic dimension and an anisotropic dimension that shows the distinct changes in the lineshapes with the changes in temperature. Comparisons of the anisotropic lineshapes obtained from static and VACSY experiments on DMS clearly show sensitivity to different NMR time scales for the two experiments (Fig. 4.5). At room temperature for instance, the static spectrum shows little evidence of molecular reorientations, whereas the VACSY patterns are already considerably distorted due to the effects of motions. Likewise, the VACSY experiment yields a motionally averaged pattern at 55 °C whereas the static lineshape at the same temperature is still well in the intermediate exchange regime. However, as discussed above, molecular reorientation information can still be obtained from the VACSY lineshapes by simulating the entire 2D VACSY spectrum. The exchange rates obtained from simulations of the VACSY anisotropic patterns (shown in Fig. 4.5) are in good agreement with the motional rates obtained for similar temperatures in the static spectrum.

Tyrosine Ethyl Ester

To investigate the full potential of the 2D VACSY experiment for studying intermediate motion, we examined the dynamics of a multi-site system, tyrosine ethyl ester. The ^{13}C CPMAS spectra of this crystalline solid show a marked dependence on temperature.[4] Whereas the spectra recorded below 0 °C clearly exhibit one isotropic peak for each of the eleven inequivalent carbon sites in the molecule, a dynamic process makes the protonated phenyl carbons ortho to both the hydroxyl and the alkyl groups equivalent as the temperature is increased (Fig. 4.6). The splittings observed at low temperatures are characteristic of an -OH group whose fast rotation around the C-O bond is quenched in the solid. In crystalline compounds where dynamic processes rarely disturb the translational

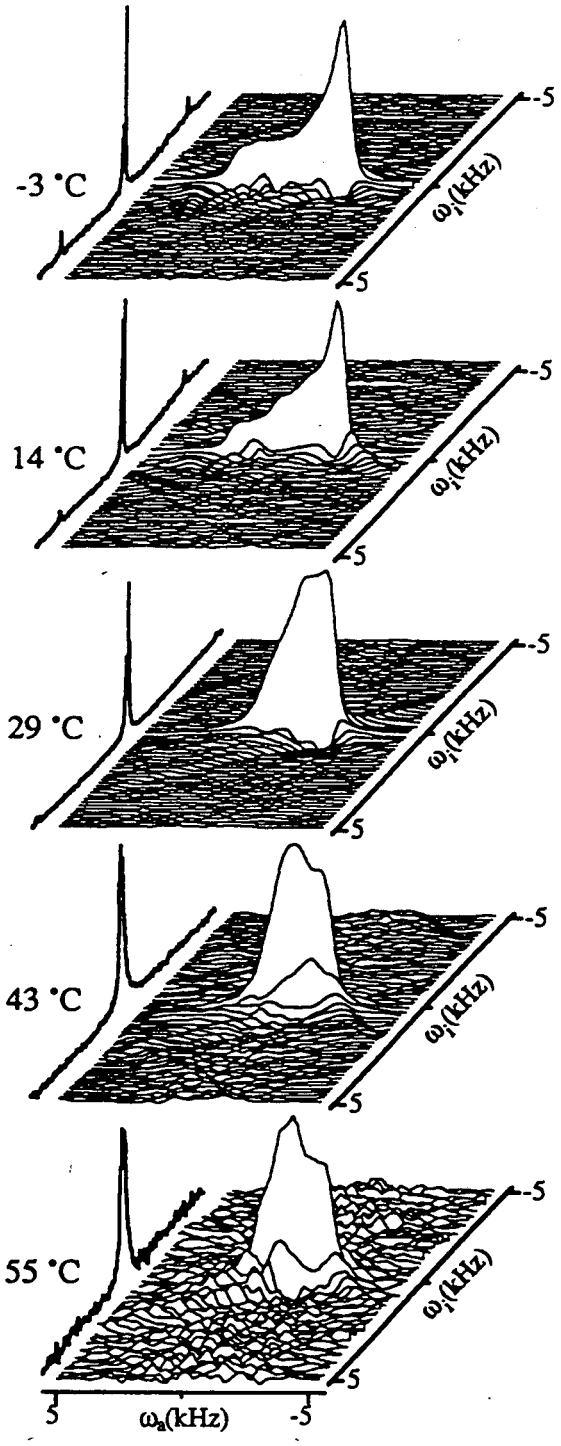

Figure 4.4. 2D VACSY spectra of DMS recorded as a function of temperature.

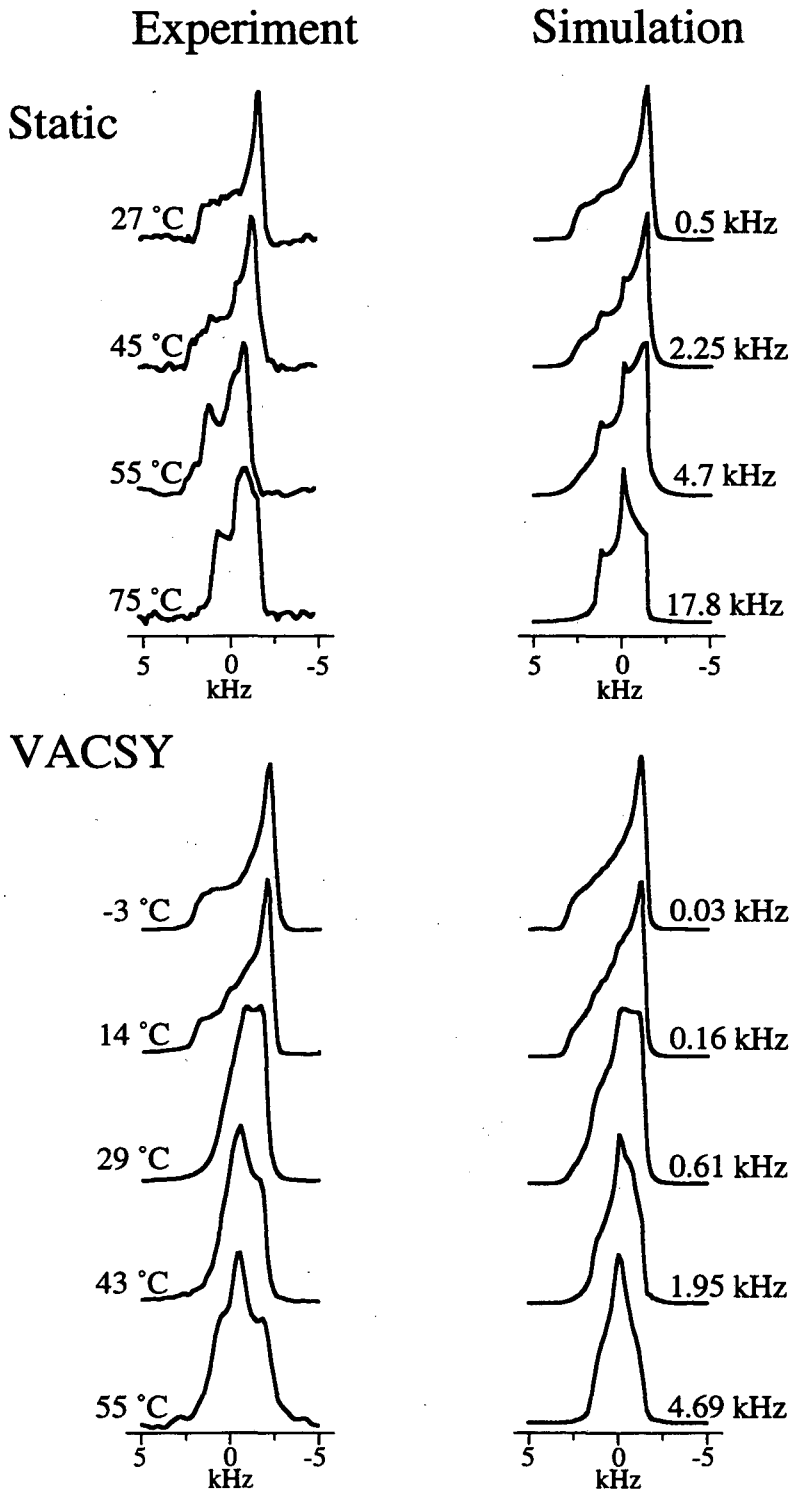

Figure 4.5 Comparisons of experimental and simulated lineshapes of DMS for static and VACSY experiments. The experimental lineshapes are labeled by the temperature at which the data were recorded, while the simulations are labeled by the exchange rates used in the computations.

symmetry of the lattice, the merging of peaks observed as temperature increases can originate either from the onset of 180° rotations of the -OH groups around their C-O bonds, from synchronized $H\cdots O-H\cdots O-\leftrightarrow H-O\cdots H-O\cdots$ intermolecular hydrogen transfer processes, or from sudden 180° reorientations of the phenyl rings about their para-axes. These three different processes cannot be unambiguously distinguished by monitoring the changes in the isotropic ^{13}C chemical shifts of the molecule. The last type of motion, however, common in both crystalline and polymeric materials, can be discriminated from the others by measuring the variations taking place in the CSA parameters of the protonated aromatic carbons. The processes involving hydroxyl group dynamics will change the anisotropic shifts of these sites by an amount comparable to the splittings observed in the low-temperature MAS spectra (ca. 3 ppm); phenyl ring reorientations on the other hand will be associated with much larger changes (ca. 50 ppm) arising from the mixing of the in-plane components of their CSA tensors.

In studying the molecular dynamics, we focused on peak *e*, the clearly resolved signal from the carbons ortho to the hydroxyl group. The CSA lineshapes as a function of temperature were obtained from the VACSY experiments and are illustrated on the left-hand column of Fig. 4.7. The averaging observed among the least shielded components of the chemical shift tensor as temperature is increased reflect 180° ring flip rotations. Such motions can be characterized by comparing experimental VACSY results with simulated lineshapes. To carry out the simulations, the principal shielding components of site *e* were obtained from low-temperature ^{13}C anisotropic lineshapes. Following single-crystal and theoretical guidelines, we placed the most shielded component of the tensor perpendicular to the aromatic ring, and least shielded direction along the C-H bond. The effects of the 180° ring flips were then taken into account by assuming mutual exchange processes between two classical sites whose CSA frequencies are related by 120° rotations of their

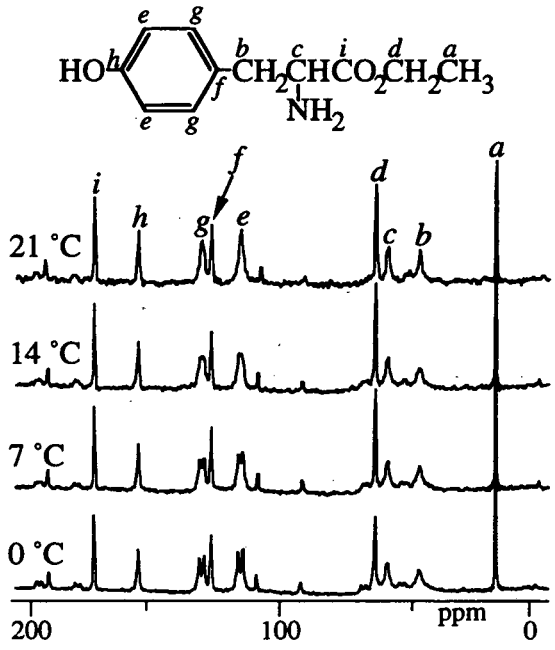

Figure 4.6 MAS spectra of tyrosine ethyl ester recorded at varying temperatures

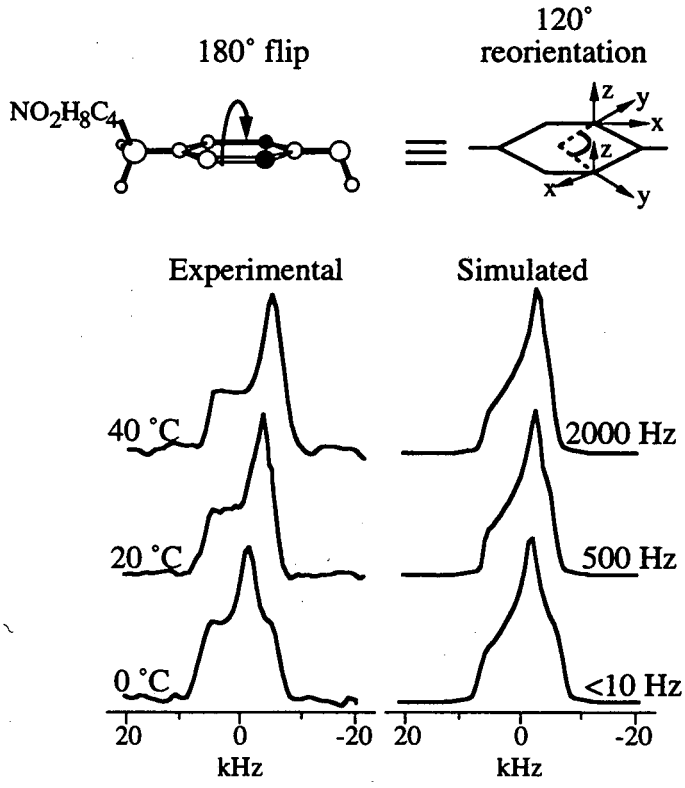

Figure 4.7 Comparison between VACSY experimental and simulated lineshapes for site *e* of tyrosine ethyl ester. The simulations were calcuated assuming 180° flips of the aromatic rings at the indicated exchange rates. This reorientation brings about 120° rotations of the CSA tensors around their z-axes as shown in the diagram on top.

tensors about the z-axes. Complete dynamic VACSY time-domain simulations were carried out as described above by integrating the signals arising from the exchanging sites over a solid sphere as a function of the macroscopic spinning angle. Figure 4.8 shows good agreement between the simulated spectra and the VACSY lineshapes, lending support to the presence of ring-flip dynamic processes for tyrosine ethyl ester in the solid phase.

4.2 Molecular Ordering

In many polymer systems, the microscopic ordering of the molecules plays an important role in many of the material's properties such as tensile strength, refractive index and Young's modulus.[5] Multi-dimensional NMR experiments have proven useful in revealing important quantitative information on the nature and level of ordering in polymer fibers and films.[6-8] In this section I will discuss the application of 2D VACSY to obtain the orientation distribution of ordered isotactic polypropylene (iPP).

When the distribution of crystallites in a system is no longer isotropic, the powder spectral patterns seen in chapter 2 become altered. Since the features of these patterns are characteristic of the level of ordering in the system, VACSY may be applied as in the previous example to resolve the anisotropic pattern for each chemical site, and computer simulated fits can be used to obtain information on the molecular ordering in the system.

4.2.1 Molecular Ordering Theory

In describing the partial orientation of molecules, it is useful to define a director frame in which primary sample order direction is along the Z_D axis. As in the case of molecular dynamics, the transformation from the PAS frame to the laboratory frame may

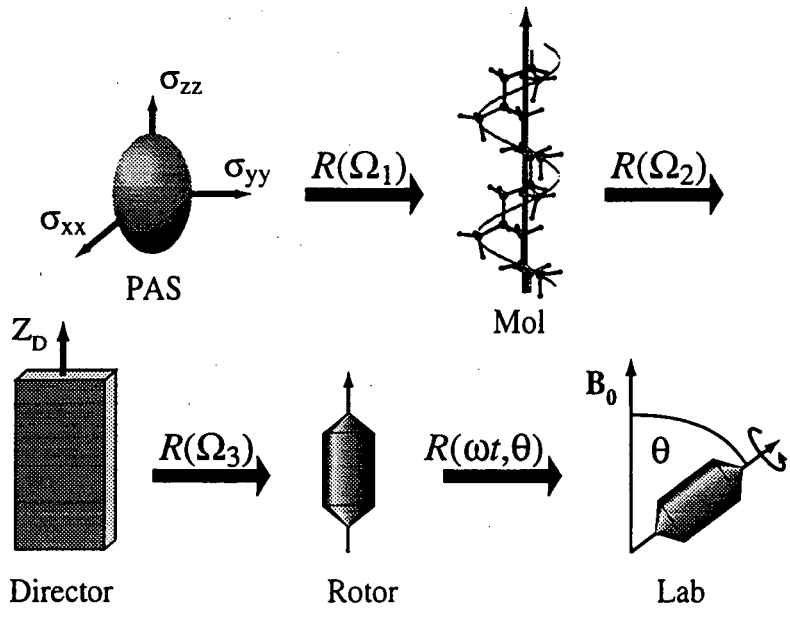

Figure 4.8. Coordinate transformations rotating the coordinate axis from the CSA PAS frame to the lab frame for an ordered system. The Z_D axes of the director frame designates the primary order direction.

then be broken down into consecutive transformations as shown in Fig. 4.8. Using the addition theorem of Wigner rotation matrices, the chemical shift frequency for an ordered system by be written in the identical manner as Eq. 4.2; but now, the sets of Euler angles Ω_1, Ω_2, and Ω_3 are defined by the transformations shown in Fig. 4.8.

If we assume the sets of Euler angles Ω_3 and Ω_1 to be constant for each isotropic site, the 1D anisotropic spectrum for the given site may be written as

$$I(\omega) = \int P(\Omega_2)\delta\left[\omega - \omega^a(\Omega_2)\right]d\Omega_2. \tag{4.22}$$

$P(\Omega_2)$ is the orientation distribution function, and $P(\Omega_2)d\Omega_2$ defines the fraction of molecules with an orientation between Ω_2 and $\Omega_2 + d\Omega_2$ with respect to the director frame. The simplest model for $P(\Omega_2)$ is a spherical Gaussian distribution,[8]

$$P(\Omega_2) = \exp\left[-\sin^2 \alpha_2/(2\alpha_\sigma^2)\right]\exp\left[-\sin^2 \beta_2/(2\beta_\sigma^2)\right] \times \exp\left[-\sin^2 \gamma_2/(2\gamma_\sigma^2)\right], \tag{4.23}$$

where the full width at half maximum for a particular angular distribution is defined as $\Delta\alpha = 2\sqrt{2\ln 2}\ \alpha_\sigma$ and similarly for $\Delta\beta$ and $\Delta\gamma$.

Alternatively order parameters and moments can be used to describe the orientation distribution:[9]

$$P(\Omega_2) = \sum_{l=0}^{\infty} \sum_{m,n=l}^{-l} P_{lmn} D^l_{mn}(\Omega_2), \tag{4.24}$$

where P_{lmn} are moments of the distribution. Order parameters are defined as

$$\left\langle D^l_{mn}(\Omega_2)\right\rangle = \left(8\pi^2\right)^{-1} \int P(\Omega_2) D^l_{mn}(\Omega_2) d\Omega_2 \tag{4.25}$$

and are related to the moments by

$$P_{lmn} = (2l+1)\left\langle D^l_{mn}(\Omega_2)\right\rangle. \tag{4.26}$$

Case of Uniaxial Symmetry

In certain cases, the symmetry of the ordering can be used to simplify the equations presented above. Well defined helical structure of molecular chains leads to a microscopic axial symmetry in the orientation distribution, while the large diameter of the drawn samples leads to a macroscopic axial symmetry. Thus the orientation distribution is constant in two of the three Euler angles (transverse isotropy).[10] Equation 4.23 then simplifies to

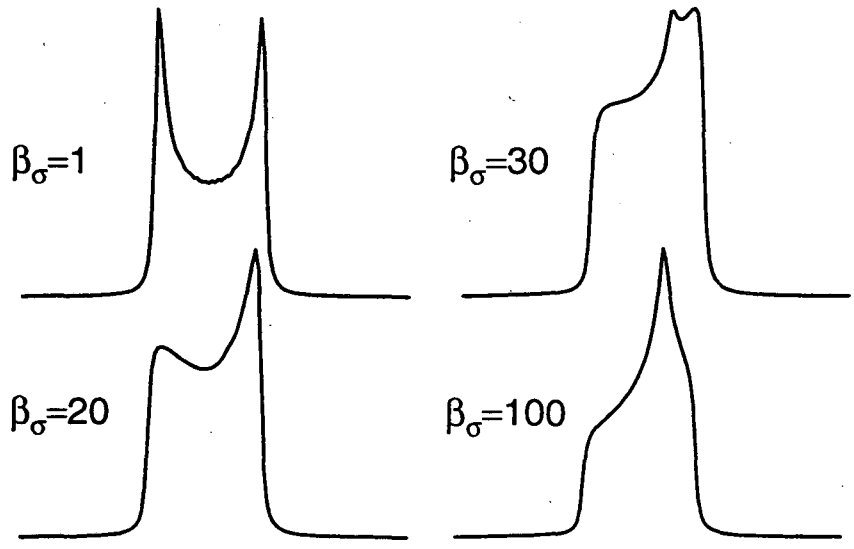

Figure 4.9. Simulations of $\eta = 0.5$ lineshapes for different levels of molecular ordering. A one-dimensional Gaussian orientation distribution function is used in the simulations with the Z_p axis set 90° from the static field.

$$P(\beta_2) = \exp\left[-\sin^2\beta_2/\left(2\beta_\sigma^2\right)\right] \tag{4.27}$$

for the Gaussian distribution, while Eq. 4.24 simplifies to

$$P(\beta_2) = \sum_{l=0}^{\infty}(2l+1)\left\langle P_l(\cos\beta_2)\right\rangle P_l(\cos\beta_2) \tag{4.28}$$

with

$$\left\langle P_l(\cos\beta_2)\right\rangle = \int P(\beta_2)P_l(\cos\beta_2)d\beta_2 \tag{4.29}$$

Figure 4.9 shows changes in the simulated lineshapes for different levels of ordering, using Eq. 4.27 as the orientation dsitribution function.

3.2.2 Experimental

The ^{13}C 2D VACSY experiments were performed on ordered isotactic polypropylene $\left(\text{iPP},\ \left[-CH_2CH-(CH_3)-\right]_n\right)$ obtained from Hoechst AG (Frankfurt, Germany). This polymer exhibits sharp X-ray diffraction peaks arising from well-defined crystalline regions in which two symmetry-related polypropylene chains are helically arranged, each one possessing three monomers per unit cell (3_1 helix).[11,12]. The ordering of the sample is characterized by a single draw axis, and the sample was cut into disks and placed inside the rotor with the draw axis perpendicular to the spinning axis. The CSA tensor values and orientations for each of the three carbon sites were obtained from literature[13] and are shown in Fig. 4.10. and are listed in Table 4.1.

The iPP spectra were recorded at 7.07 T with a carbon resonant frequency at 75.74 MHz, using the conventional cross polarization pulse sequence described previously in chapter 2.

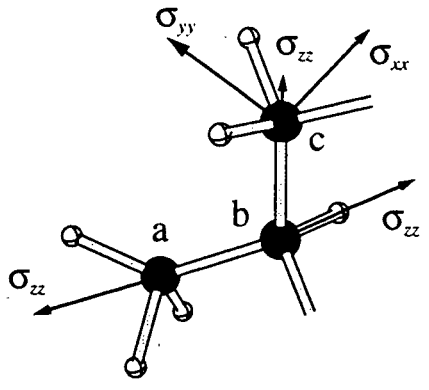

Figure 4.10. The orientation of the CSA tensors in the molecular frame. The tensors for the methine (b) and methyl (a) carbons are nearly axially symmetric so only one axis is required to describe the orientations for these tensors. The σ_{zz} of the methine carbon is placed along the $C-H$ bond. The σ_{zz} of the methyl carbon is placed along the $CH-CH_3$. The σ_{xx} of the methylene carbon is perpendicular to the $H-C-H$ plane, while the σ_{yy} axis is offset from bisecting the $H-C-H$ angle.

group	σ_{xx}	σ_{yy}	σ_{zz}
CH_2	26	44	65
CH	21	21	38
CH_3	32	32	3

Table 4.1. CSA parameters for the three sites of iPP. The tensor values are in ppm from TMS.

Thirty-one different rotation axis angles in the range $90^\circ \leq \theta \leq 35.3^\circ$ were used and the complete data set was interpolated onto a 128×128 grid.

3.2.3 Results and Discussion

The anisotropic patterns obtained from the 2D VACSY experiments on ordered and disordered iPP show significant changes in the powder patterns for all three sites due to sample ordering (Fig. 4.11). To obtain quantitative information on the level of ordering, iterative computer simulated fits were made to the experimental lineshapes using Powell's minimization method.[14] The anisotropic patterns were calculated assuming transverse isotropy and weighted by the orientation distributions given in Eqs. 4.27 and 4.28. To obtain the computational speed required for the iterative fitting, weighted orientation averaging was made using method the proposed by Alderman *et al.*.[15]

Figure 4.11 shows the simulated lineshapes using a Gaussian orientation distribution with a FWHM of 15°. Similar lineshapes were also obtained using Eq. 4.28 for the orientation distribution, with the order parameters listed in Table 4.2.

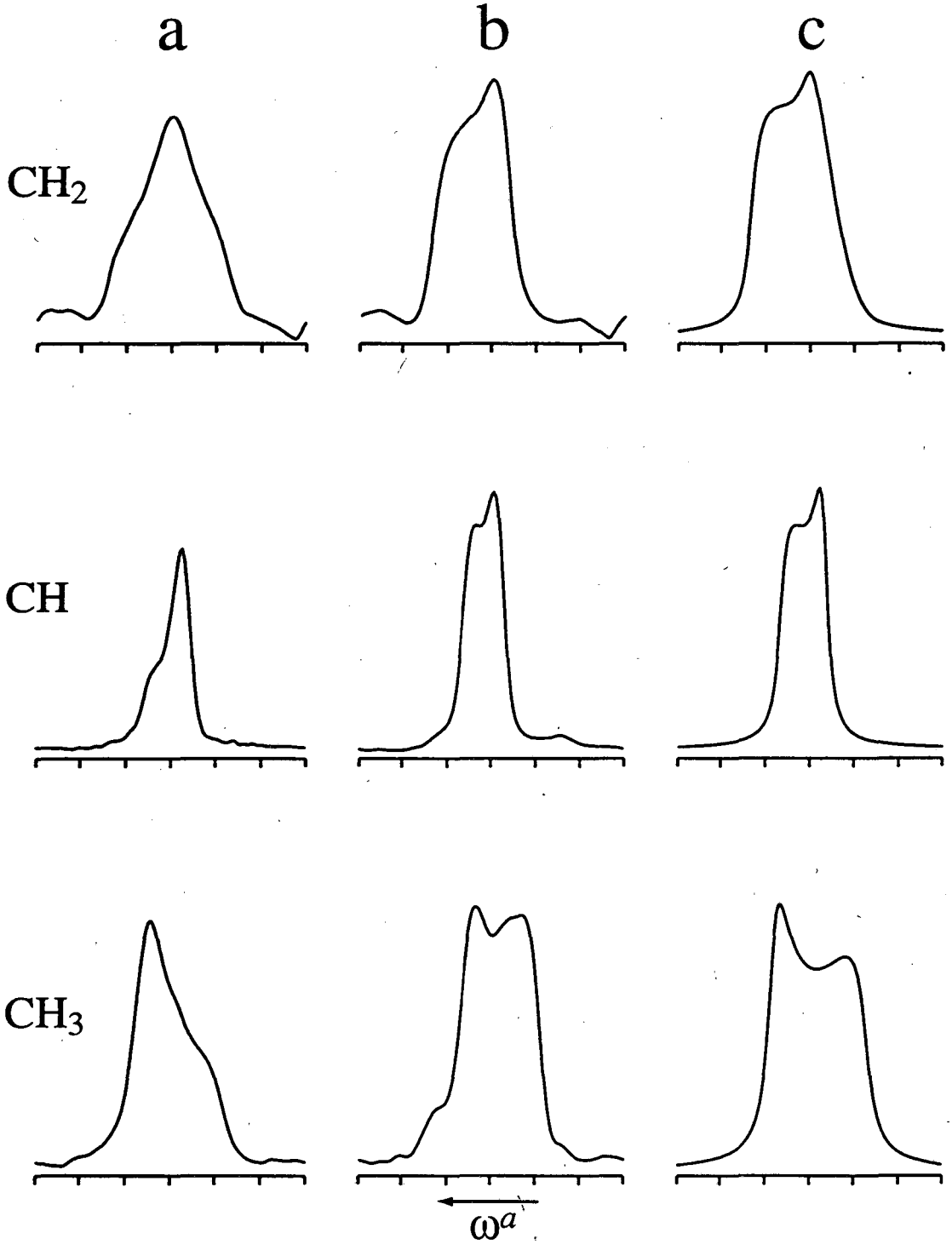

Figure 4.11 Anisotropic ^{13}C spectral patterns for the three sites of iPP. The spacing of the tick marks corresponds to 1 kHz. (a) Powder patterns obtained from a 2D VACSY experiment on a non-ordered sampled of iPP. (b) Anisotropic patterns obtained from a 2D VACSY experiment on a partially ordered sample of iPP. (c) Simulated spectral patterns using a 1D spherical Gaussian orientation distribution function with $\beta_\sigma = 15°$

l	2	4	6	8	10
$\langle P_l(\cos\theta)\rangle$	0.45	0.34	0.2	0.03	0.05

Table 4.2 Order parameters for the iPP orientation distribtution function.

However the fits to the experimental data were not improved significantly, suggesting the ordering of the polymer is mainly a Gaussian distribution.

References

1. H. W. Spiess, *Dynamic NMR Spectroscopy in Solids*; Springer-Verlag, Berlin, 1978.

2. A. Abragam, *Priciples of Nuclear Magnetism*; Clarendon Press, Oxford, 1961.

3. M. S. Solum, K. W. Zilm, J. Michl, and D. M. Grant, J. Phys. Chem., **87**, 2940 (1983).

4. A. Schmidt, intermed exchange of tyrosine ethyl ester, The Weizmann Institute of Sciences, Rehovot, Israel, 1989.

5. I. M. Ward, *Structure and Properties of Oriented Polymers*; Applied Science Publishers Ltd., London, 1975.

6. P. M. Henrichs, Macromolecules, **26**, 2099 (1987).

7. K. Schmidt-Rhor, M. Hehn, D. Schaefer, and H. W. Spiess, J. Chem. Phys., **97**, 2247 (1992).

8. B. F. Chmelka, K. Schmidt-Rohr, and H. W. Spiess, Macromolecules, **26**, 2282 (1993).

9. R. Hentschel, J. Schlitter, H. Sillescu, and H. W. Spiess, J. Chem. Phys., **68**, 56 (1978).

10. G. S. Harbison, V. Vogt, and H. W. Spiess, J. Chem. Phys., **86**, 1206 (1987).

11. Z. Mencik, J. Macromol. Sci., Phys., **B6**, 101 (1972).

12. A. Bunn, M. E. A. Cudby, R. K. Harris, K. J. Packer, and B. J. Say, Polymer, **23**, 694 (1982).

13. T. Nakai, J. Ashida, and T. Terao, Mag. Res. Chem., **27**, 666 (1989).

14. W. H. Press, S. A. Teukolsky, W. T. Vetterling, and B. P. Flannery, *Numerical Recipes in C*; Cambridge University Press, Cambridge, 1992.

15. D. W. Alderman, M. S. Solum, and D. M. Grant, J. Chem. Phys., **84**, 3717 (1985).

Chapter 5 3D VACSY Exchange

In the previous chapter, 2D VACSY was applied to examine molecular dynamics in the intermediate time regime. In this chapter, 3D experiments that incorporate the VACSY technique will be used to examine slow molecular motions in polymers.

Molecular dynamics play an important role in determining macroscopic mechanical properties of polymers. Both amorphous and crystalline polymers exhibit distinct temperature dependent mechanical relaxation properties. The different relaxation processes are labeled α, β, γ etc., with α being associated with the highest temperature process and the other processes being associated with decreasing temperatures. These relaxation processes are directly related to microscopic molecular motions. For example in many polymers, the α relaxation process is associated with slow, large-scale motions of polymer chains.[1,2] Such motions can be studied by solid-state 2D exchange experiments that correlate the molecular orientations at two different times, separated by a long mixing period to allow for molecular motion. The resulting 2D exchange spectrum directly reflects the probability distribution function for molecular reorientation.[3] However, just as in the previous chapters, where overlapping 1D anisotropic line shapes impede spectral analysis, the overlapping 2D exchange patterns limit the application of solid-state exchange experiments to simple or labeled systems.

In this chapter, I will present two different 3D experiments that incorporate the VACSY technique to separate ^{13}C exchange spectra according to their respective chemical sites. These experiments are used to examine the helical jum motions in isotactic polypropylene (iPP).

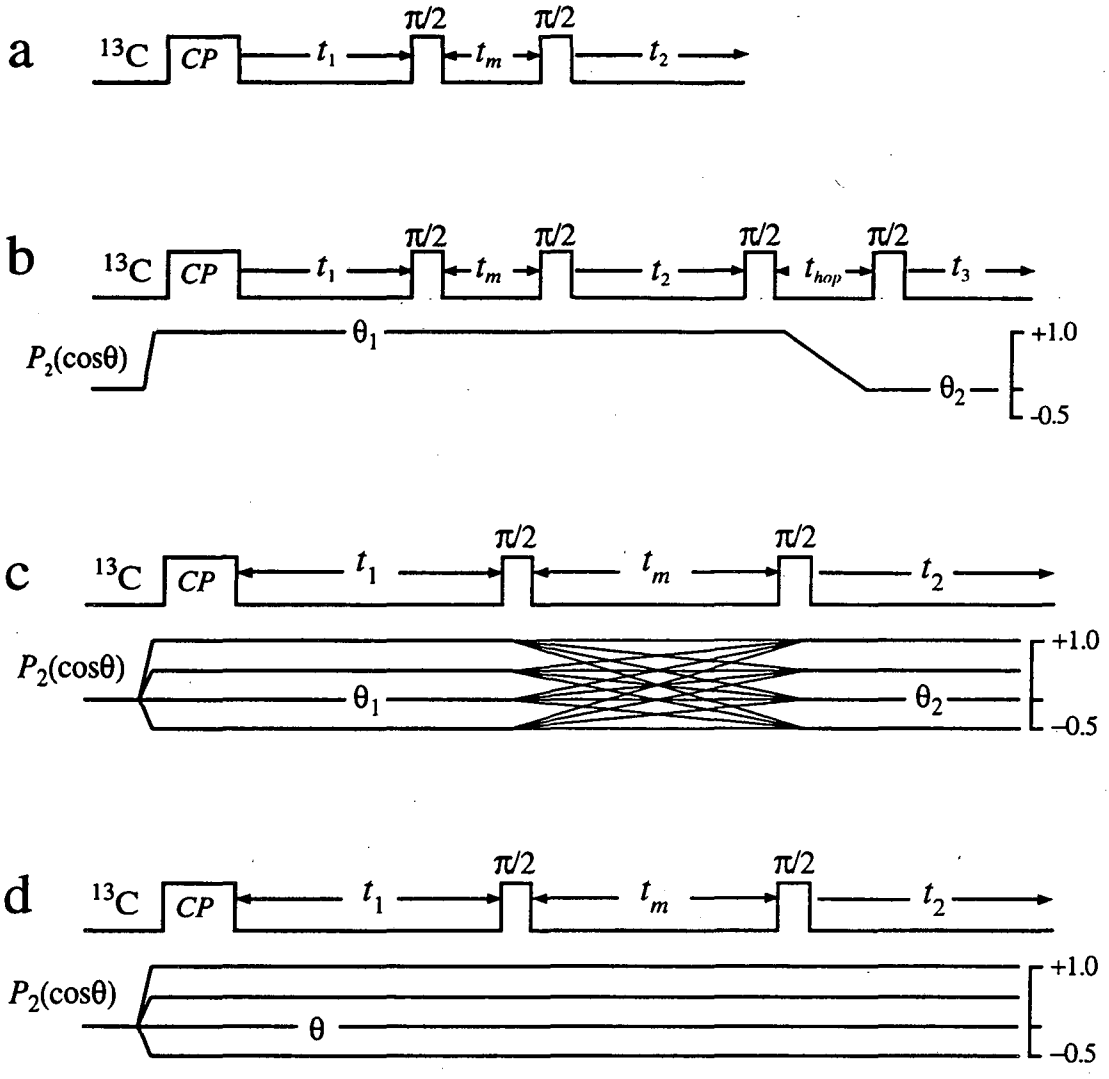

Figure 5.1 Pulse sequences and rotation axis angle profiles for 2D and 3D solid-state exchange experiments. In all sequences, ^{13}C magnetization is created by cross polarization from ^{1}H magnetization, and ^{1}H decoupling is applied throughout except during t_m and t_{hop} delays. (a) 2D exchange sequence. The evolution and detection periods, t_1 and t_2, are separated by a long mixing delay, t_m. (b) Extension of the 2D sequence to a high resolution 3D experiment by the conventional NMR method of adding a high resolution time dimension. Evolution during t_1 and t_2 occurs with the sample spinning about $\theta_1 = 0°$, while detection occurs with $\theta_2 = 54.74°$. (c) 3D VACSY-S exchange pulse sequence. The initial time delay, t_1, is a constant time delay, while θ_1 and θ_2 are varied independently. (d) 3D VACSY-T exchange pulse sequence. The normal 2D exchange sequence in (a) is applied at different angles θ.

5.1 2D Exchange

The 3D VACSY exchange experiments are based on the three-pulse sequence (Fig. 5.1a) that has been extensively used in 2D ^{13}C exchange experiments to study slow molecular reorientation in the time scale of 0.1 Hz to 1 kHz.[4] A similar sequence may also be used for ^{2}H NMR exchange experiments. The initial ^{13}C magnetization is created by cross polarization from ^{1}H magnetization. The ^{13}C magnetization of a particular isochromat then evolves during t_1 with a CS frequency

$$\omega_{CS}(\Omega_1) = \omega^i + \sqrt{\tfrac{2}{3}}\omega_0 \sum_{m=-2}^{2} D^2_{m0}(\Omega_1)\rho_m, \tag{5.1}$$

where Ω_1 specifies the set of Euler angles, (α_1,β_1), that rotate the coordinate axes from the PAS frame of the CSA tensor to the lab frame, and ω^i is the isotropic chemical shift frequency. The second pulse stores one component of the magnetization parallel to $\mathbf{B_0}$ for the duration of the mixing period, t_m, and the third pulse returns the magnetization to the transverse plane for detection during t_2. If molecular reorientation occurs during t_m, a new set of Euler angles, Ω_2, defines the relative orientation of the CSA tensor frame and the lab frame. The frequency of the same isochromat during t_2 detection then becomes

$$\omega_{CS}(\Omega_2) = \omega^i + \sqrt{\tfrac{2}{3}}\omega_0 \sum_{m=-2}^{2} D^2_{m0}(\Omega_2)\rho_m, \tag{5.2}$$

where the isotropic frequency, ω^i, is assumed unchanged during t_m. The complete 2D NMR signal may be written as an ensemble average over all possible isochromats,

$$\begin{aligned} S(t_1,t_2;t_m) &= \left\langle \exp\left[i\omega_{CS}(\Omega_1)t_1\right]\exp\left[i\omega_{CS}(\Omega_2)t_2\right]\right\rangle \\ &= \iint P(\Omega_1,\Omega_2;t_m)\exp\left[i\omega_{CS}(\Omega_1)t_1\right]\exp\left[i\omega_{CS}(\Omega_2)t_2\right]d\Omega_1 d\Omega_2, \end{aligned} \tag{5.3}$$

where $P(\Omega_1,\Omega_2;t_m)$ is the joint probability distribution of the orientations of the CSA tensors before and after the delay t_m. $P(\Omega_1,\Omega_2;t_m)$ is related to the 2D spectrum by

$$I(\omega_1,\omega_2) = \int P(\Omega_1,\Omega_2;t_m)\delta[\omega_1 - \omega_{CS}(\Omega_1)]\delta[\omega_2 - \omega_{CS}(\Omega_2)]d\Omega_1 d\Omega_2 \qquad (5.4)$$

The ability to obtain detailed information about $P(\Omega_1,\Omega_2;t_m)$ directly from spectrum makes NMR unique in its ability to examine not only the time scale of the motions but also the geometry of the reorientations.

$P(\Omega_1,\Omega_2;t_m)$ may also be written in terms of conditional probabilities as

$$P(\Omega_1,\Omega_2;t_m) = P(\Omega_1)P(\Omega_2|\Omega_1;t_m), \qquad (5.5)$$

where $P(\Omega_1)$ is the probability distribution for the initial orientation of the PAS frame, and $P(\Omega_2|\Omega_1;t_m)$ is the conditional probability for the PAS frame to have the orientation defined by Ω_2 after the mixing delay, given that its initial orientation was defined by Ω_1. For a sample with an isotropic, powder distribution of crystallites, $P(\Omega_1)$ is constant; for an oriented sample, $P(\Omega_1)$ may be obtained experimentally as a sum of weighted subspectra as discussed in chapter 4. The conditional probability $P(\Omega_2|\Omega_1;t_m)$ depends on the motional model for molecular reorientation. One such model is random jump reorientations between n equivalent sites;[3,4] $P(\Omega_2|\Omega_1;t_m)$ is then a solution to a set of differential equations describing a stationary Markov process,

$$\frac{dP(\Omega_i|\Omega_j;t_m)}{dt} = C_J \sum_{k=1}^{n} P(\Omega_i|\Omega_k;t_m), \qquad (5.6)$$

where C_J is the jump probability between any two sites. From Eq. 5.6, the solution for the joint probabilities becomes

$$P(\Omega_i|\Omega_i;t_m) = (1/n)\left[1+(n-1)\exp(-nC_j t_m)\right]$$
$$P(\Omega_i|\Omega_j;t_m) = (1/n)\left[1-\exp(-nC_j t_m)\right], \qquad i \neq j. \tag{5.7}$$

Figure 5.2 shows simulations of possible 2D exchange patterns for rotational diffusion and discrete random jumps. For rotational diffusion, the diagonal ridge broadens out to off-diagonal intensities; in the limit of $t_m D_R \rightarrow \infty$, the diagonal ridge disappears and the off-diagonal intensity completely fills up the spectral area accessible by random molecular reorientation (Fig. 5.2a). In contrast, the exchange patterns for discrete jump motions reveal distinct elliptical ridge patterns (Fig. 5.2b) that become more prominent as $C_j t_m \rightarrow \infty$.

When $\eta = 0$, the exchange pattern only depends on the distribution of the reorientation angle, β, which may be obtained directly from the geometry of the exchange pattern without the assumption of a motional model.[5,6] When $\eta \neq 0$, as is generally the case in ^{13}C NMR, extracting quantitative information becomes more difficult since the exchange pattern now depends on all three of the reorientation angles; however, important qualitative information such as limits in the jump angle amplitudes and the number of jump sites may still be obtained directly from the spectrum.[4] Such information can be used to limit the number of possible motional mechanisms involved in the reorientation process.

Since their original introduction, 2D solid-state exchange experiments have been used extensively in both ^{2}H and ^{13}C NMR to study the motional mechanisms of various different systems.[4,6,7] However, while these studies are potentially very powerful, they are limited in that ^{2}H NMR requires isotopic labeling and natural abundance ^{13}C NMR is rendered impractical in all but the simplest systems due to overlapping patterns from chemically distinct but unresolved sites.

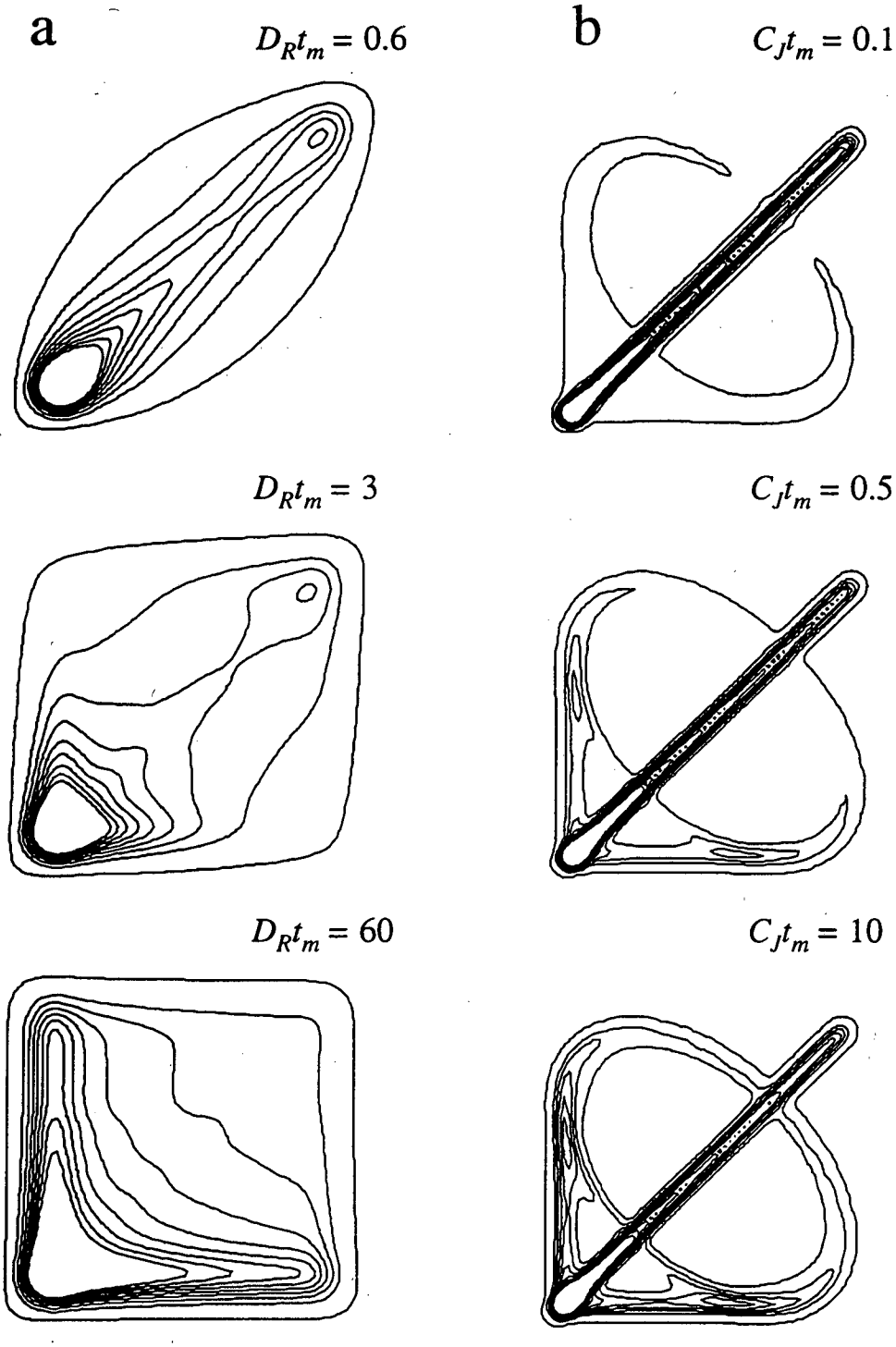

Figure 5.2 2D exchange patterns for $\eta = 0.0$ line shapes. (a) Exchange patterns for rotational diffusion. D_R is the rotational diffusion constant. (b) Exchange patterns for discrete jump motions among three equivalent sites. The simulations involved reorientations of the unique axis of the anisotropy tensor by ±120°. C_J is the jump probability.

To overcome this problem of overlapping exchange patterns, a 3D experiment is required to separate the anisotropic exchange patterns according to isotropic chemical shifts. Figure 5.1b shows how this may be accomplished by the conventional multidimensional NMR method of simply adding an extra time dimension. A normal 2D exchange experiment is performed on a spinning sample with the rotor axis parallel to the $\mathbf{B_0}$ field, $\theta_1 = 0°$. The magnetization is then stored while the rotor is hopped to the magic angle ($\theta_2 = 54.74°$) and detection during t_3 occurs with the spin system evolving with only the isotropic chemical shift frequency. Although the extension of the experiment to three dimensions is straightforward, it involves a significant loss in the signal intensity; the extra storage of the magnetization reduces the signal by a factor of $\sqrt{2}$, and T_1 relaxation further reduces magnetization during the hopping storage delay. The experiments presented below incorporate the VACSY technique and offer alternative methods of obtaining high-resolution 3D exchange correlations without the signal losses associated with extra magnetization storage sequences.

5.2 Structure and Helical Motion of iPP

The potential applications of the 3D VACSY exchange experiments were examined by analyzing the motional behavior of isotactic polypropylene $\left(\text{iPP}, \left[-\text{CH}_2\text{CH}-(\text{CH}_3)-\right]_n\right)$. The structure of this polymer and the orientation of CSA tensors for each ^{13}C site have been discussed in section 4.2.2. A side view of the helix is shown in Fig. 5.3a, and the view along the helix axis with the methyl groups pointing outward is shown in Fig 5.3b. Mechanical and dielectric measurements on iPP have shown that slow motion in the range of 1 Hz to 1 kHz occurs at elevated temperatures.[8] ^{13}C and ^{2}H NMR studies have shown that iPP undergoes discrete threefold 120° jumps about the helix axis[4,9] (Fig. 5.3b), and the correlation times strongly indicate that this helical motion is responsible for the α relaxation process.

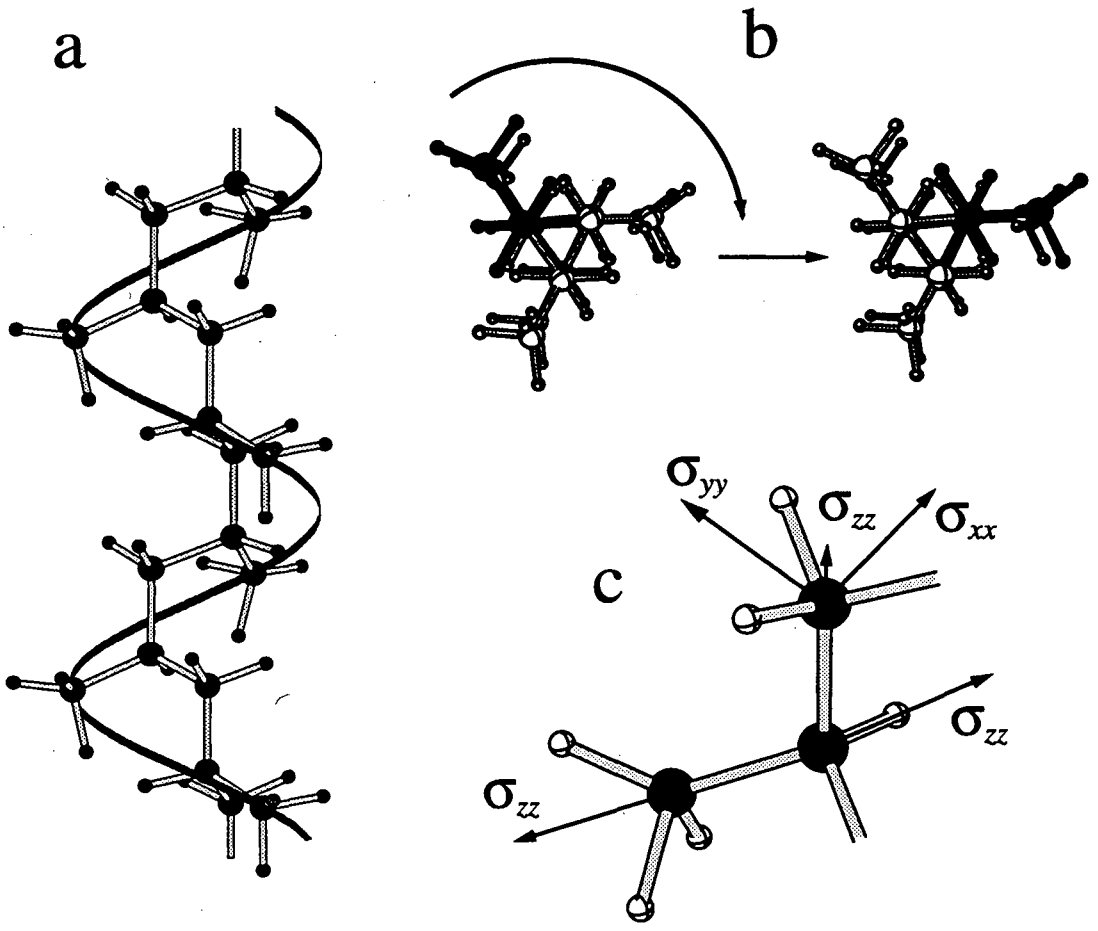

Figure 5.3 (a) Side view of the iPP helix. (b) View of the molecule along the helix axis. The three-fold helical jump motion is illustrated by the highlighted (–CH–CH_3) group that undergoes a 120° rotation. (c) Orientation of the CSA tensors in the molecular frame are described in section 3.2.2.

5.3 3D Switched-Angle VACSY (VACSY-S) Exchange

5.3.1 Theory

In order to apply the VACSY technique to the solid-state exchange experiments described above, we must consider molecular reorientation with respect to the rotor frame rather than the lab frame. This is done in the identical manner as for 2D VACSY in Eqs. 2.4 and 2.5 by using the addition theorem for Wigner rotation matrices and incorporating an additional rotation from the PAS frames to the rotor frame and then rotating from the rotor frame to the lab frame. For a fast spinning sample, Eqs. 5.1 and 5.2 become

$$\begin{aligned} \omega_1 &= \omega^i + P_2(\cos\theta)\omega_1^a(\Omega_1) \\ \omega_2 &= \omega^i + P_2(\cos\theta)\omega_2^a(\Omega_2), \end{aligned} \tag{5.8}$$

where

$$\begin{aligned} \omega_1^a(\Omega_1) &= \gamma\sqrt{\tfrac{2}{3}}\omega_0 \sum_{m=-2}^{2} D_{m0}^2(\Omega_1)\rho_m \\ \omega_2^a(\Omega_2) &= \gamma\sqrt{\tfrac{2}{3}}\omega_0 \sum_{m=-2}^{2} D_{m0}^2(\Omega_2)\rho_m, \end{aligned} \tag{5.9}$$

are the anisotropic frequencies; the sets of Euler angles Ω_1 and Ω_2 relate the two PAS frames with the rotor axis frame.

The correlations desired in a high resolution 3D exchange experiment are

$$\begin{pmatrix} \omega_1 \\ \omega_2 \\ \omega_3 \end{pmatrix} = \begin{pmatrix} \omega_1^a \\ \omega_2^a \\ \omega^i \end{pmatrix}. \tag{5.10}$$

Figure 5.1c shows a pulse sequence that obtains these correlations by incorporating the VACSY technique and a hop of the rotor during t_m.[10] This experiment will be referred to as 3D switched-angle VACSY (VACSY-S) exchange. According to Fig. 5.1c the magnetization evolves for a *fixed* time t_1 at a specified rotation axis angle θ_1. During the mixing period, t_m, the rotation axis angle is changed to θ_2, and the signal is acquired during t_2 with a total phase,

$$\Phi = \omega^i t_1 + \omega_1^a P_2(\cos\theta_1) t_1 + \omega^i t_2 + \omega_2^a P_2(\cos\theta_2) t_2, \tag{5.11}$$

The phase may be written in the form of Eq. 2.1 by partitioning along three-dimensions as

$$\begin{aligned} \Phi_1 &= \omega_1^a(\Omega_1) P_2(\cos\theta_1) t_1 \\ \Phi_2 &= \omega_2^a(\Omega_2) P_2(\cos\theta_2) t_2 \\ \Phi_3 &= \omega^i t_2 \end{aligned} \tag{5.12}$$

and defining the τ space coordinates as

$$\begin{pmatrix} \tau_1 \\ \tau_2 \\ \tau_3 \end{pmatrix} = \begin{pmatrix} P_2(\cos\theta_1) t_1 \\ P_2(\cos\theta_2) t_2 \\ t_2 \end{pmatrix} \tag{5.13}$$

The two angles θ_1 and θ_2 are incremented *independently* in the course of the experiment. These two angles and the signal detection time, t_2, make up the three adjustable experimental parameters required for the 3D experiment. Note that since t_1 is a *constant*

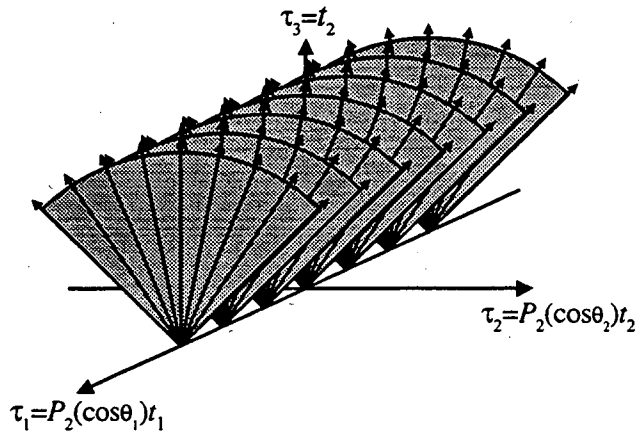

Figure 5.4. Trajectories of FIDs for the 3D VACSY-S exchange experiment. When $P_2(\cos\theta_1)=0$ the signal evolves on the $\tau_1=0$ plane in the identical manner as in the 2D VACSY experiment. When $P_2(\cos\theta_1)\neq 0$ the signal acquires a additional phase shift $\Delta\Phi = P_2(\cos\theta_1)t_1\omega_1^a$ that results in a translation of the 2D VACSY plane along the τ_1 dimension, filling the three-dimensional phase space.

time variable, $\omega^i t_1$ is simply a correctable first order phase shift and is thus not included in the partitioned phase in Eq. 5.12.

The FIDs acquired with $P_2(\cos\theta_1)=0$ form trajectories on the $\tau_1 = P_2(\cos\theta_1)t_1 = 0$ plane (Fig. 5.4) with the coordinates, $[0, P_2(\cos\theta_2)t_2, t_2]$, which are identical to those of 2D VACSY. The only difference in this experiment is that when $P_2(\cos\theta_1)\neq 0$, the magnetization acquires a phase shift,

$$\Delta\Phi = \omega_1^a P_2(\cos\theta_1)t_1, \tag{5.14}$$

during t_1 evolution. This effectively translates the 2D VACSY planes along the $\tau_1 = P_2(\cos\theta_1)t_1$ axis, filling the 3D phase space, as shown in Fig. 5.4. Thus each τ_2, τ_3 plane must be interpolated in an identical manner to 2D VACSY (Eq. 2.10) with the discrete coordinates,

$$\tau_2 = RP_2(\cos\theta_2)nt_d$$
$$\tau_3 = nt_d, \tag{5.15}$$

where now $R = sw_2^a / sw^i$, with sw_2^a being the spectral width in the anisotropic ω_2^a dimension and sw^i being the spectral width in the isotropic ω^i dimension; and t_d is the dwell time. After interpolation the 3D matrix is Fourier transformed to obtain the correlation spectrum.

The correlations in Eq. 5.10 could also have been obtained by incrementing t_1 and keeping θ_1 constant; however, there are some distinct advantages to incrementing θ_1 and using a constant time evolution during the first frequency encoding period. In direct analogy to "spin-warp" imaging techniques, higher sensitivity is obtainable by using constant time evolution.[11] By incrementing θ_1 the signal may span both positive and negative τ_1 values; the resulting echo provides a simple method for removing phase artifacts from the final spectrum. Finally, since $P_2(\cos\theta_1)$ does not modulate the isotropic frequency, ω^i only appears in the ω_3 dimension, leaving traceless anisotropic patterns in the other two dimensions; this allows for more efficient data encoding and storage.

5.3.2 Experimental

The experimental set up for VACSY-S exchange was identical to that used for 2D VACSY, except that the spectrum was recorded on a 7.07 T magnet with a ^{13}C frequency of 75.74 MHz. The sample of powdered iPP was obtained from Aldrich Chemicals. Both θ_1 and θ_2 were incremented independently through 31 different angles within the bounds $-0.5 \le P_2(\cos\theta_i) \le 0.5$. The experiment was performed at room temperature with the sample temperature being elevated by about 7° K due to the frictional heating of the spinning rotor. All FIDs were acquired with a dwell time 166.7 μs; the constant delay t_1 was set to 5 ms corresponding to a spectral width of 6 kHz in both the ω_1 and ω_2

dimensions; both the mixing delay, t_m, and the recycle delay was set to 1s. The total data acquisition time was 5 days. All data processing was done on a Stardent 3000 Titan computer. Each plane perpendicular to τ_1 was interpolated onto a 128x64 grid in the same manner as described in chapter 2. The entire data set was then zero-filled to a 128^3 matrix and then Fourier transformed.

5.3.4 Results and Discussion

In agreement with the results from previous ^{13}C and ^{2}H studies, the spectra from 3D VACSY-S exchange experiment, shown in Fig. 5.5, reveal off-diagonal exchange intensities for each of the chemical sites of iPP.[10] But due to the weak intensity of off-diagonal patterns, direct comparisons with simulations and motional models are difficult. The exchange patterns from the 3D experiment are, however, comparable to the patterns obtained from a 2D exchange experiment shown in Fig. 5.6. Thus we conclude that the poor quality of the exchange patterns is due to the weak intensity of the off-diagonal ridges at the temperature used in the experiment, rather than the methodology of the VACSY-S experiment.

The main feature of the VACSY-S exchange experiment in comparison to the conventional 3D exchange experiment is that by incorporating the hop of the rotor axis into the mixing delay, an extra storage sequence is removed which leads to signal to noise enhancement for the 3D experiment.

However, one disadvantage of the 3D VACSY-S exchange experiment is that a sudden reorientation of the rotor during the mixing delay is still required. I will present in the next section an alternative 3D VACSY exchange experiment that removes all requirements for the sudden rotor axis reorientation.

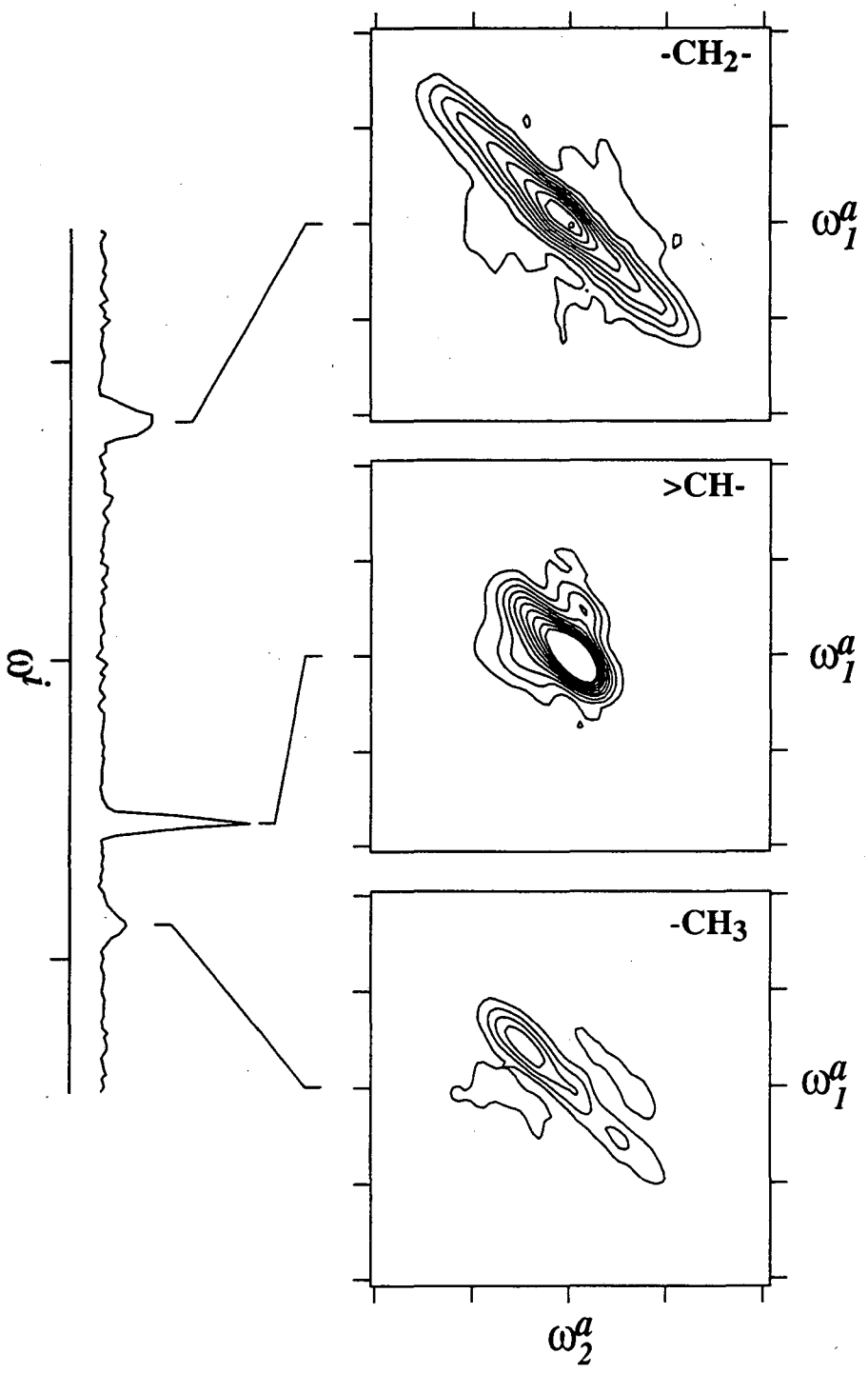

Figure 5.5 Results of the 3D VACSY-S Exchange experiment on isotactic polypropylene. The 1D plot on the left is the isotropic projection of the full 3D data set; the 2D correlation spectra on the right correspond to slices extracted at the isotropic shifts of the different sites. The data was acquired with t_m = 1 s. All markers are 1 kHz apart.

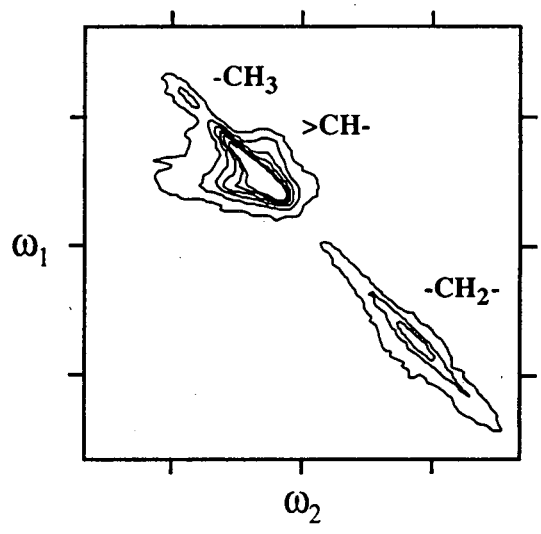

Figure 5.6. 2D exchange spectrum of iPP obtained by using the pulse sequence shown in Fig. 5.1a. The mixing period $t_m = 1$ s, and all markers are 1 kHz apart.

5.4 3D Total VACSY (VACSY-T) Exchange

In contrast to VACSY-S, which requires a series of phase modulated 2D VACSY data sets, the VACSY-T experiment (Fig. 5.1d), requires a series of 2D exchange experiments, each recorded at a different rotation axis angle. We refer to this experiment as 3D total VACSY (VACSY-T) exchange to draw on the direct analogies to the original 2D VACSY experiment. Just as 2D VACSY uses the scaling of one-dimensional powder patterns at each angle to separate the isotropic and anisotropic chemical shifts, 3D VACSY-T uses the scaling of two-dimensional anisotropic patterns at each angle for the isotropic separation (Fig. 5.7), and both the 2D VACSY and 3D VACSY-T have the advantage that they require incremental changes in the rotor axis only at the end of the complete pulse sequence.

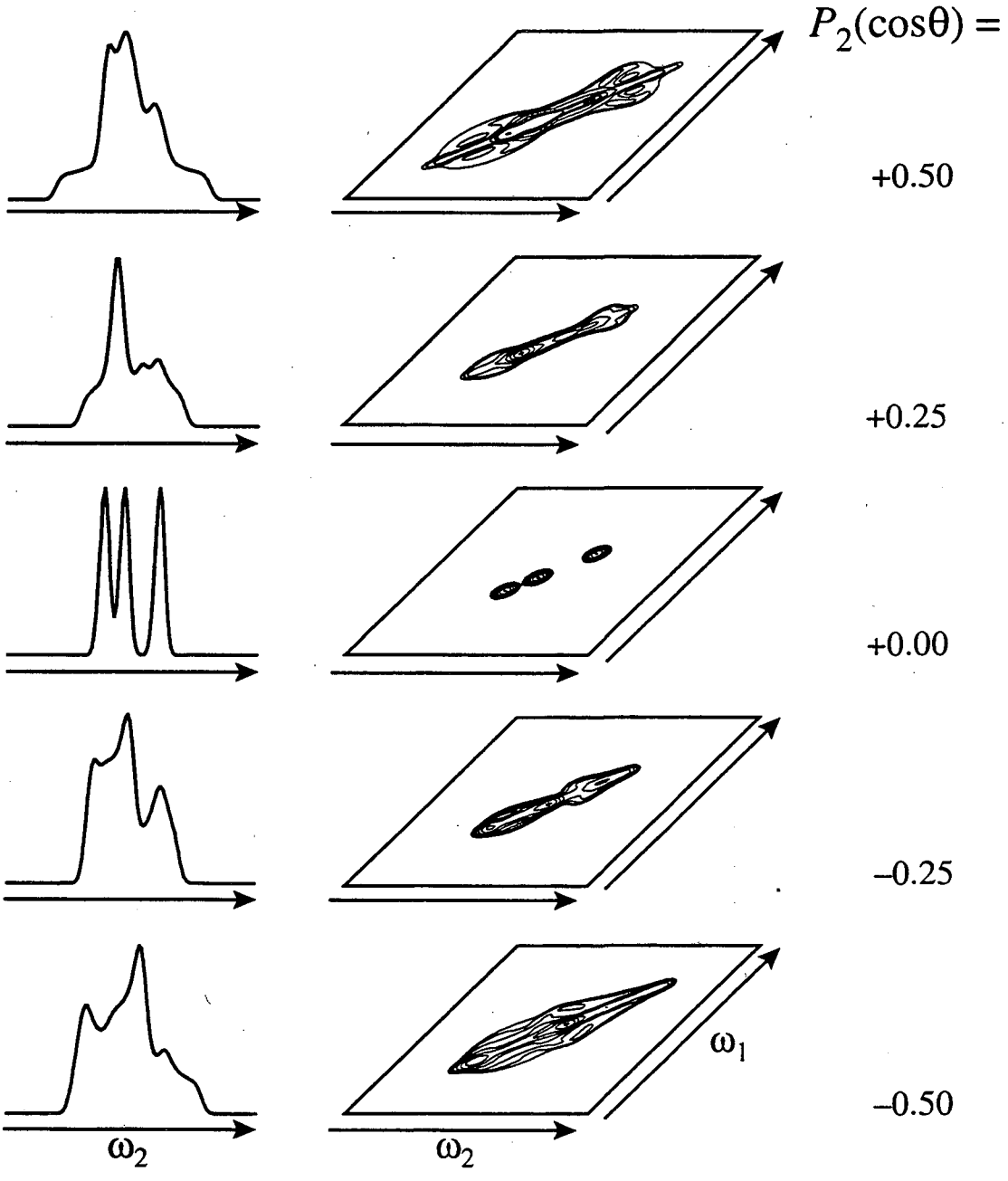

Figure 5.7 Scaling of the anisotropic patterns of three different chemical sites at different rotation axis angles, θ. Simulations of 1D spectra and 2D exchange spectra, corresponding to evolution at different angles, θ, are shown. The anisotropic components of the spectra are scaled by the second Legendre polynomial, $P_2(\cos\theta)$, while the isotropic components are left invariant. This scaling of the anisotropic frequency causes overlapping of the spectral patterns from the three sites for all but the $P_2(\cos\theta) = 0$ spectra.

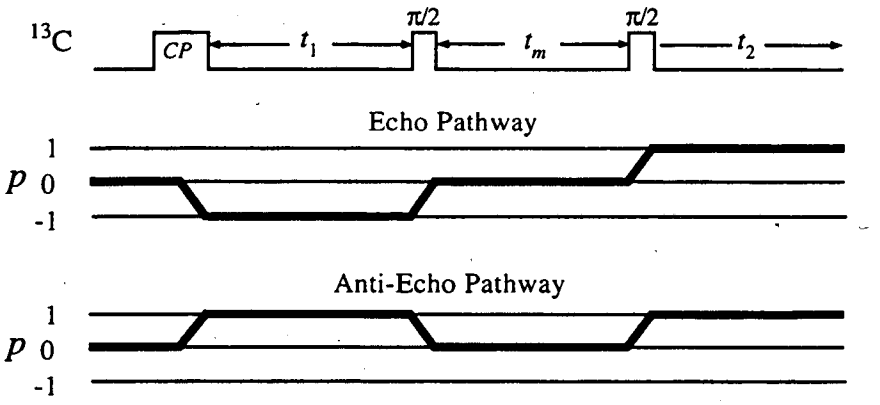

Figure 5.8. Coherence pathways for the two sets of data acquired in the 3D VACSY-T exchange experiment. The echo data are acquired using the $p=-1$ t_1 coherence pathway, while the anti-echo data are acquired using the $p=+1$ t_1 coherence pathway.

5.4.1 VACSY-T Exchange: General Theory

The frequency variables correlated in VACSY-T are identical to those of VACSY-S and are given in Eq. 5.10. The three adjustable parameters in this experiment are the angle θ, and the two time variables t_1 and t_2. In addition, signal for both the $p=+1$ and $p=-1$ t_1 coherence pathways are acquired (Fig. 5.8); the $p=-1$ signal forms stimulated echoes during t_2, while the $p=+1$ signal forms anti-echoes.[12] This separate detection of both coherence pathways is reminiscent of the States acquisition method where cosine and sine amplitude modulated data are acquired separately to obtain a pure-phase 2D spectrum.[13] Here, it provides access to larger areas of τ space and reduces truncation artifacts in the line shapes. The total phase,

$$\Phi = \omega^i p t_1 + \omega_1^a P_2(\cos\theta) p t_1 + \omega^i t_2 + \omega_2^a P_2(\cos\theta) t_2, \qquad (5.16)$$

acquired in each variable-angle spinning 2D exchange experiment, is partitioned into three dimensions,

$$\begin{aligned}\Phi_1 &= \omega_1^a P_2(\cos\theta) p t_1 \\ \Phi_2 &= \omega_2^a P_2(\cos\theta) t_2 \\ \Phi_3 &= \omega^i (p t_1 + t_2).\end{aligned} \tag{5.17}$$

To obtain the desired frequency correlations, the τ space coordinate axes are defined as

$$\begin{pmatrix}\tau_1 \\ \tau_2 \\ \tau_3\end{pmatrix} = \begin{pmatrix}P_2(\cos\theta_1) p t_1 \\ P_2(\cos\theta_2) t_2 \\ p t_1 + t_2\end{pmatrix}. \tag{5.18}$$

Even though these coordinates appear similar to those that define τ space for VACSY-S (Eq. 5.13), because different parameters are being incremented, the FIDs for this experiment form entirely different trajectories.

The placement of the FIDs in τ space can be clarified by considering the geometric patterns generated by different subsets of the data. The set of data points for $t_2 = 0$ (the first points of all the FIDs) maps onto the $\tau_2 = 0$ plane with the phase space coordinates $[P_2(\cos\theta) p t_1, 0, p t_1]$. Aside from the sign factor in p, these coordinates on the $\tau_2 = 0$ plane are once again identical to those of 2D VACSY. The $p = +1$ signal forms rays on the plane in the familiar 2D VACSY pattern, while the $p = -1$ signal forms rays below the $\tau_3 = 0$ plane in an inverted 2D VACSY pattern, as illustrated in Fig. 5.9. For $t_2 > 0$, the FIDs emerge from the rays on this plane to fill the 3D phase space.

The set of data points for t_1 and t_2 evolution at one specific angle θ_i will map onto a skewed plane in the three dimensional phase space as shown in Fig. 5.10. These points correspond to the data acquired at the angle θ_i during a complete 2D exchange experiment. The data points on the $\tau_2 = 0$ plane form a ray inclined at an angle

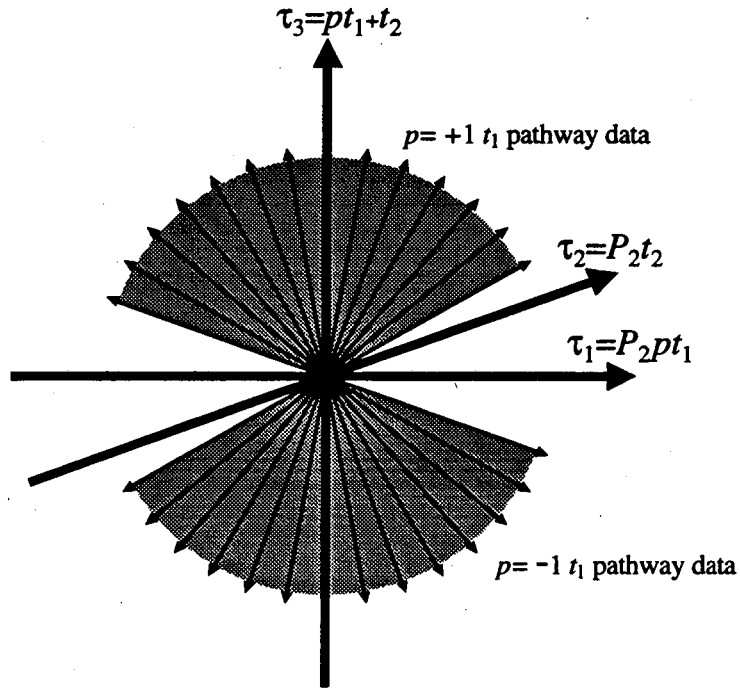

Figure 5.9 Mapping of all $t_2 = 0$ data points in the 3D VACSY-T experiment onto the $\tau_2 = 0$ plane. All the data points map onto the plane with the coordinates $[P_2(\cos\theta)pt_1,0,pt_1]$. The $p = +1$ t_1 pathway data points are placed on the plane in the same manner as in the 2D VACSY experiment (Fig. 2.4). The $p = -1$ t_1 pathway data points are placed below the $\tau_3 = 0$ plane in an inverted 2D VACSY pattern.

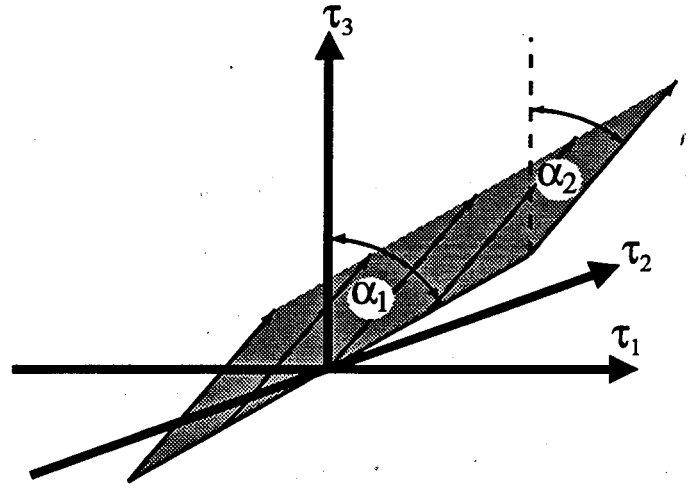

Figure 5.10 Trajectories of 3D VACSY-T data for t_1 and t_2 evolution at one particular rotation axis angle θ_i. The t_1 evolution at θ_i for $t_2 = 0$ is represented by one of the rays from Fig. 5.9. The ray makes an angle $\alpha_1 = \tan^{-1}[R_1P_2(\cos\theta_i)]$ with respect to the isotropic τ_3 axis, with half of the ray above the τ_3 plane. With t_2 increments, the FIDs emerge from this ray at an angle $\alpha_2 = \tan^{-1}[R_2P_2(\cos\theta_i)]$ with respect to the τ_3 axis. Thus the 2D exchange signal acquired at one angle θ_i maps onto a skewed plane in the 3D phase space.

$$\alpha_1 = \tan^{-1}[R_1 P_2(\cos\theta_i)] \tag{5.19}$$

with respect to the isotropic τ_3 axis, where $R_1 = \mathrm{sw}_1^a/\mathrm{sw}^i$, with sw_1^a being the spectral width in the anisotropic ω_1^a dimension, and sw^i being the spectral width in the isotropic ω^i dimension (Fig. 5.10). This ray of data corresponds to one of the rays in Fig. 5.9. With increasing t_2, evolution not only occurs along the anisotropic τ_2 dimension but also along the isotropic τ_3 dimension. Thus, unlike conventional 3D NMR experiments, the FIDs do not emerge from the $\tau_2 = 0$ plane in a perpendicular trajectory, but at an angle,

$$\alpha_2 = \tan^{-1}[R_2 P_2(\cos\theta_i)], \tag{15.20}$$

with respect to the isotropic axis, where $R_2 = \mathrm{sw}_2^a/\mathrm{sw}^i$, and sw_2^a is the spectral width in the anisotropic ω_2^a dimension (Fig. 5.10). Figure 5.11 shows how the data acquired at other rotation axis angles form trajectories in similar 2D planes but skewed at different angles, α_1 and α_2. Note that when $\theta_i = 54.74^\circ$ (the magic angle), the entire plane collapses on to the isotropic axis, since at this angle, $P_2 = 0$, and no anisotropic evolution occurs. This change in the orientation of the 2D exchange data planes for different θ_i allows the 3D τ space to be densely filled with data.

In the final processing step all data points that map below the $\tau_3 = 0$ plane are complex conjugated and spatially inverted into the upper four octants where the data are interpolated onto a Cartesian matrix. The interpolation is simplified when t_1 and t_2 increments are identical. Then $R_1 = R_2$, and all of the data points lie on equally spaced Cartesian planes perpendicular to the isotropic τ_3 axis. In this case, 2D interpolation is required on each of these planes, while no interpolation is required along the isotropic dimension. Figure 5.12 shows the patterns made by the experimental data on some of the

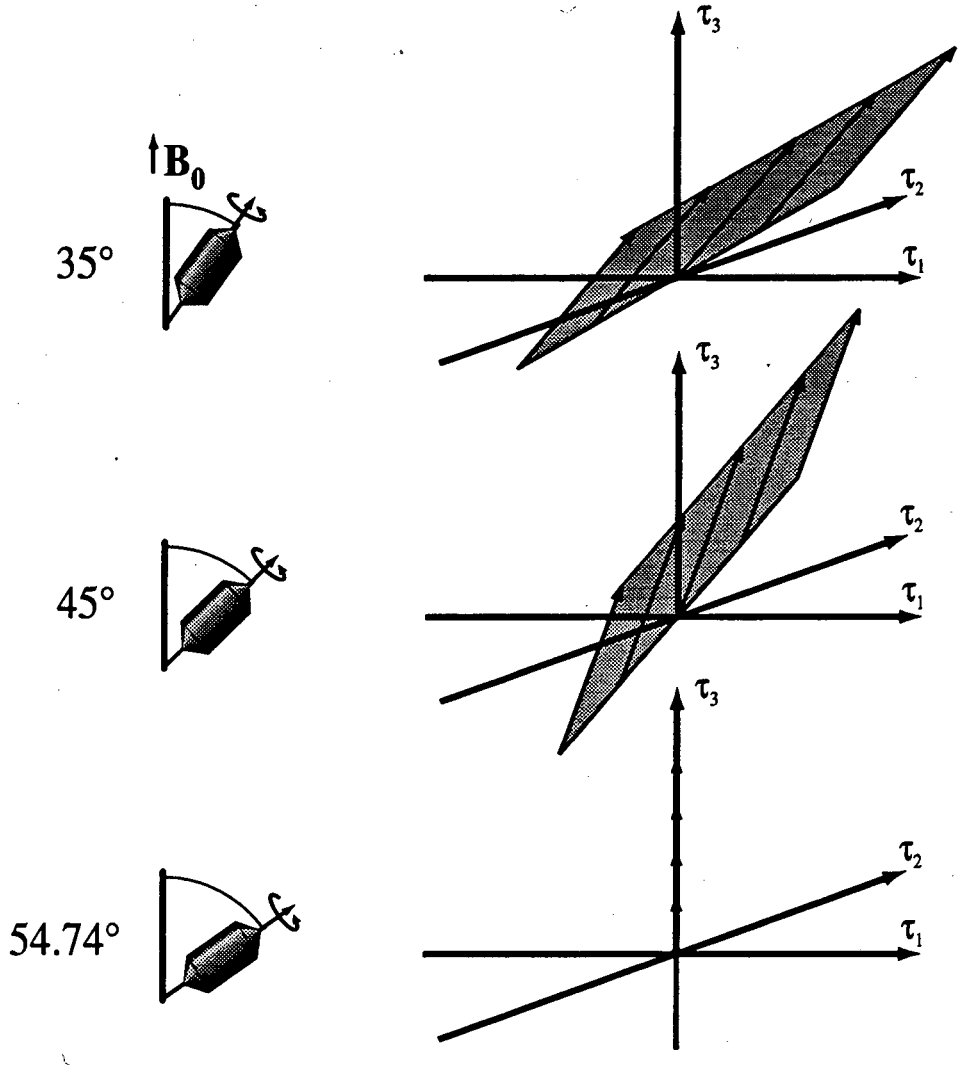

Figure 5.11 Trajectories of VACSY-T data for t_1 and t_2 evolution at three different rotation axis angles. At different rotation angles θ_i, the angles α_1 and α_2 defining the orientation of the data plane in the 3D phase space changes, allowing the full 3D phase space to be filled with data. At θ_i=54.74°, $\alpha_1 = \alpha_2 = 0$, and the 2D data plane collapses onto the isotropic axis.

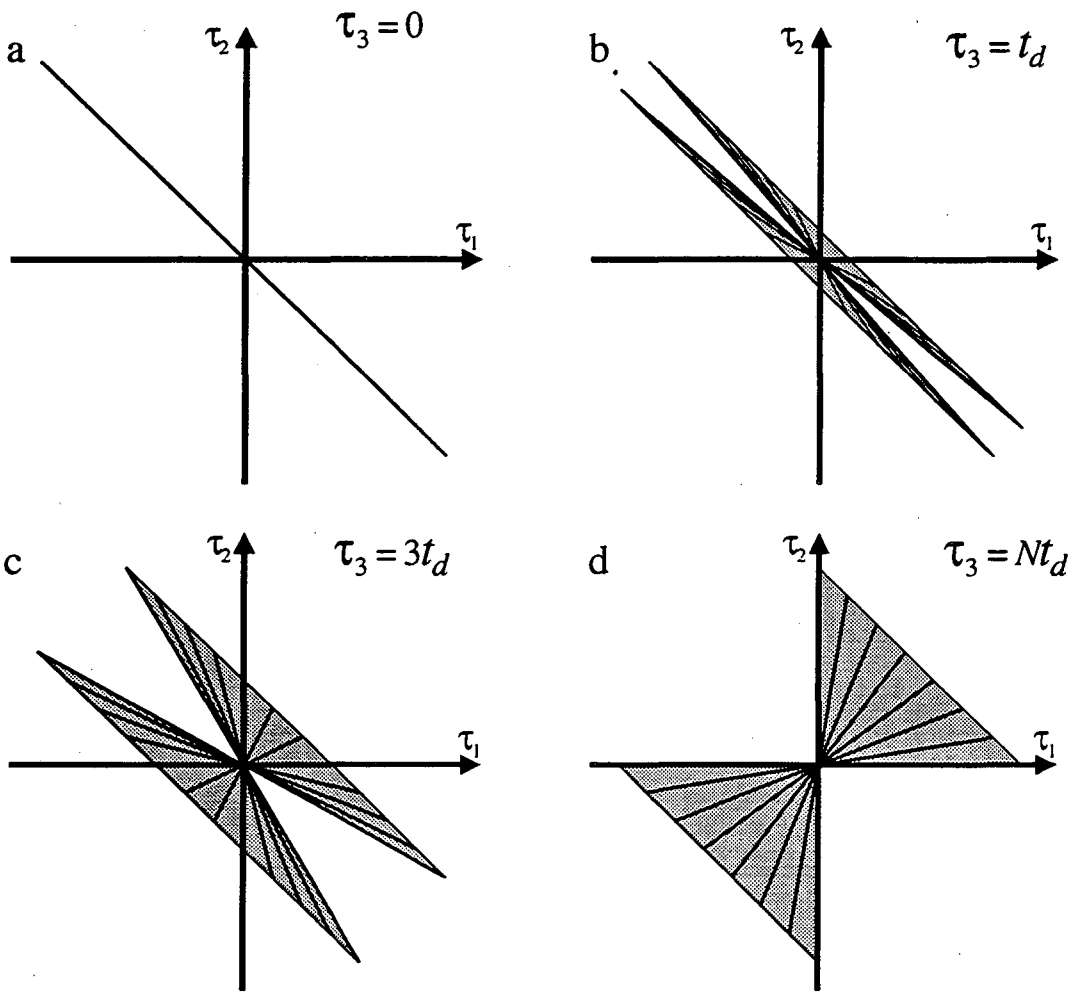

Figure 5.12 The patterns made by data points on different isotropic planes perpendicular to the τ_3 axis. For these patterns, all the data have been mapped onto the 3D phase space. Data points originally below the τ_3 plane have been complex conjugated and spatially inverted into the upper half of the phase space. (a) $\tau_3 = 0$ plane. Only a single ray of data exists on this plane along the $\tau_3 = -\tau_1$ line. The rest of the area on the plane contains no data, and thus all the points outside of the line are set to zero. The data on this plane correspond to the stimulated-echo tops. (b) and (c) show the data mappings for higher τ_3 planes. As τ_3 increases, the portions of the phase space containing data (the shaded regions) also increases; the regions outside of this area are set to zero (d) The data mapping onto the highest isotropic plane at $\tau_3 = Nt_d$, where $N+1$ is the total number of data points in each FID. The data on this plane occupies only two of the quadrants.

τ_3 planes. Further details of the coordinate calculations and the interpolation procedure are given in following section. After interpolation, a 3D Fourier transformation yields the final spectrum.

The data rearrangement procedure required for both 3D VACSY exchange experiments is an extension of the procedure used in 2D VACSY. All three experiments require tracing out linear trajectories of FIDs in τ space tilted at angles determined by the rotation axis orientations and the relative anisotropic and isotropic spectral widths. In fact an excellent check of the interpolation routine for 3D VACSY-T exchange is to examine the $\tau_1 = 0$ or the $\tau_2 = 0$ planes in the 3D time domain data matrix after interpolation. Since the coordinates for the data on these planes are identical to those of 2D VACSY, a Fourier transformation of the time domain data from these planes gives the same spectrum as the 2D VACSY experiment.

5.4.2 Coordinate Mappings for VACSY-T Coordinates

General Properties of the VACSY-T Coordinates

During t_2 evolution, the $p = -1$ t_1 pathway signal forms stimulated echoes while the $p = +1$ t_1 pathway signal forms anti-echoes. The data are thus separated into 4 arrays, D_a^+, D_a^-, D_e^+, and D_e^-, depending on the sign of the parameters during acquisition. The + and – superscripts designate the sign of P_2, while a and e subscripts designate the sign of the t_1 pathway. The array elements are specified by i, j, and k indices; i denotes the angle at which the experiment took place, j denotes the t_1 increment, and k denotes the t_2 increment. These indices have the following bounds:

$$\begin{aligned} 1 \le \mathrm{i} \le N_a \\ 0 \le \mathrm{j} \le N_1 \\ 0 \le \mathrm{k} \le N_2, \end{aligned} \tag{5.21}$$

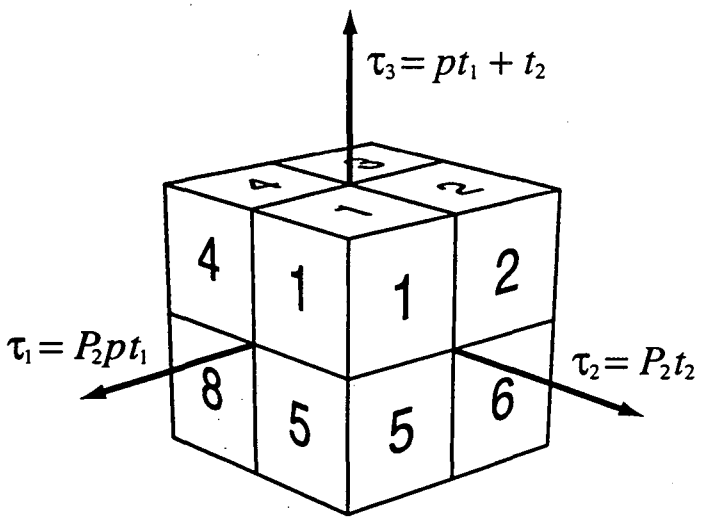

Figure 5.13. Labeling of the octants in the 3D phase space. All the octants of the 3D cube are shown and numbered except octant 7 which is hidden in the perspective shown in the figure.

where N_a is the number of different angles used in the experiment, $N_1 + 1$ is the number of t_1 points, and $N_2 + 1$ is the number of t_2 points. For notational simplicity, we will assume $N_1 = N_2 = N$ and $R_1 = R_2 = 1$.

Using the labeling of the octants in Fig. 5.13, the data contained in each of the four arrays can be shown to map into different regions of the phase space listed in Table 5.1. Since the anti-echo signal evolves with $\tau_3 = t_1 + t_2$, the D_a^+ and D_a^- data points map

p (t_1 path)	$P_2(\cos\beta)$	Data Array	Mapping Region
+1	+	$D_a^+(i,j,k)$	octant 1
+1	-	$D_a^-(i,j,k)$	octant 3
-1	+	$D_e^+(i,j,k)$	octants 2, 6
-1	-	$D_e^-(i,j,k)$	octants 4, 8

Table 5.1. Regions of the Fourier space mapped by each of the four data arrays. The octants are defined in Fig. 5.13. The integers *i, j,* and *k* index the rotation axis angle, t_1 and t_2 increments, respectively.

only above the $\tau_3 = 0$ plane. When $P_2 > 0$, the anti-echo signal evolves along the $+\tau_1$ and $+\tau_2$ axes, which restricts the mapping of the D_a^+ data points to octant 1. Likewise, when $P_2 < 0$ the anti-echo signal evolves along the $-\tau_1$ and $-\tau_2$ axes, restricting the mapping of the D_a^- data points to octant 3. In contrast the echo signal evolves with $\tau_3 = -t_1 + t_2$; thus the D_e^+ and D_e^- data points map above and below the $\tau_3 = 0$ plane. The $\tau_3 = 0$ plane itself contains all of the stimulated echo tops. When $P_2 > 0$ the echo signal evolves along the $-\tau_1$ and $+\tau_2$ axes, which restricts the mapping of the D_e^+ data points to octant 6 if $\tau_3 < 0$ and to octant 2 if $\tau_3 > 0$. When $P_2 < 0$ the echo signal evolves along the $+\tau_1$ and $-\tau_2$ axes, which restricts the mapping of the D_e^- data points to octant 8 if $\tau_3 < 0$ and to octant 4 if $\tau_3 > 0$. As mentioned above, all of the data points that map below the $\tau_3 = 0$ plane are complex conjugated and spatially inverted to the upper four octants. Thus the data points originally mapping into octant 6 will end up in octant 4, while the points originally mapping into octant 8 will end up in octant 2.

The τ space coordinates for 3D VACSY-T exchange in Eq. 5.18 may be written in discrete index form by substituting $t_1 = pjt_d$ and $t_2 = kt_d$. With an additional index l defining the isotropic τ_3 increments,

$$l = pj + k, \tag{15.22}$$

and using the condition $R_1 = R_2 = 1$, we obtain

$$\begin{aligned} \tau_1 &= P_2(\cos\theta_i)pjt_d \\ \tau_2 &= P_2(\cos\theta_i)(l - pj)t_d \\ \tau_3 &= lt_d, \end{aligned} \tag{5.23}$$

where the bounds in l are set to $-N \le l \le N$. As described above, all the data points lie on one of the equally spaced isotropic planes indexed by the integer l, and from Eq. (5.23),

index j locates the data points within each of these planes. The calculation of the τ_1 and τ_2 coordinates, required for interpolation on these planes, will now be discussed.

Mapping of the Anti-echo Data

All of the anti-echo data D_a^+ map into octant 1 (Fig. 5.14) and are acquired with $p=+1$, so Eq. (5.22) becomes

$$l = j + k. \tag{5.24}$$

On the $l=0$ plane (Fig. 5.14a), only $j=0$ satisfies Eq.(5.24) and the bounds in Eq. (5.21). Thus all of the data points $D_a^+(i,0,0)$ map into the same coordinate on the $l=0$ plane:

$$\begin{aligned} \tau_1 &= 0 \\ \tau_2 &= 0. \end{aligned} \tag{5.25}$$

These points correspond to the data acquired with zero time evolution in both t_1 and t_2.

On the $l=1$ plane (Fig. 5.14b), the Eqs. (5.21) and (5.24) are satisfied for $j=0,1$. Substituting $j=0$ into Eq. (5.23), the coordinates for $D_a^+(i,0,1)$ become

$$\begin{aligned} \tau_1 &= 0 \\ \tau_2 &= P_2(\cos\theta_i)t_d. \end{aligned} \tag{5.26}$$

Likewise, substituting $j=1$, the $D_a^+(i,1,0)$ coordinates become

$$\begin{aligned} \tau_1 &= P_2(\cos\theta_i)t_d \\ \tau_2 &= 0. \end{aligned} \tag{5.27}$$

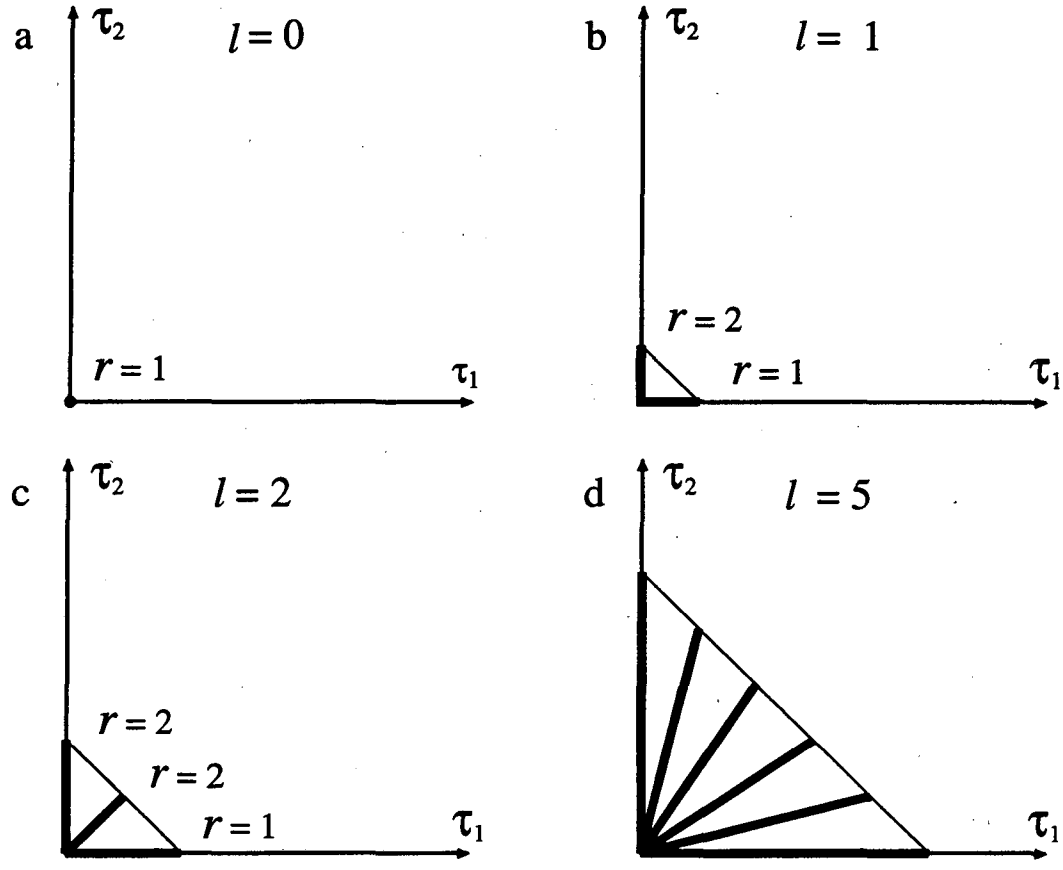

Figure 5.14 Mapping of data onto t_3 planes in octant 1. The planes are shown in *ascending* order starting from the $l = 0$ plane. This portion of the phase space is mapped by the anti-echo data with $P_2 \geq 0$ contained in the array D_a^+. The bold lines represent the rays of experimental data points that are placed in each of the planes. The rays of data are labeled by the index r and are numbered counter clockwise starting from the τ_1 axis. The specific coordinates and data points mapping into this octant are given in Table 5.2 and are discussed in the text. (a) $l = 0$ plane. There is only a single point in this plane corresponding to zero evolution in both t_1 and t_2. (b) $l = 1$ plane. The data map onto two rays, one along each of the two anisotropic axes on the plane. The data correspond to the signal obtained from a single dwell time increment in either t_1 or t_2. Each of the two rays contains N_a data points. (c) $l = 2$ plane. There are three rays of data on this plane corresponding to three different combinations of t_1 and t_2 dwell time increments to obtain $i + j = 2$. (d) $l = 5$ plane. With each higher increment of the τ_3 plane, one additional ray of data appears and the portion of the phase space covered by the data increases. There are six rays of data on this plane. Altogether, plane l contains l+1 rays of data, with each ray containing N_a data points.

These points form two rays, one along each of the axes in the plane, with each ray containing N_a data points.

On the $l=2$ plane (Fig. 5.14c) there are three rays of data corresponding to $j=0,1,2$. The coordinates on this plane are obtained in the same manner as above and are listed in Table 5.2 In general the $l=n$ plane has $n+1$ rays of data. With the rays indexed by the integer r and numbered counter clockwise from the τ_1 axis (Fig. 5.14), each ray contains the data points $D_a^+(i,n+1-r,r-1)$ with the coordinates

$$\begin{aligned}\tau_1 &= P_2(\cos\theta_i)(n+1-r)t_d \\ \tau_2 &= P_2(\cos\theta_i)(r-1)t_d.\end{aligned} \tag{5.28}$$

The data points in D_a^- map into τ space in the identical manner as described above except that since $P_2 \le 0$, the data maps into octant 3, and all the coordinates undergo a sign inversion $(\tau_1,\tau_2)\rightarrow(-\tau_1,-\tau_2)$. Table 5.2 summarizes the results of this subsection.

$l=j+k$	r	$\tau_1 = P_2 j t_d$	$\tau_2 = P_2 k t_d$	Data Points $D_a^+(i,j,k)$
0	1	0	0	$D_a^+(i,0,0)$
1	1	$P_2 t_d$	0	$D_a^+(i,1,0)$
1	2	0	$P_2 t_d$	$D_a^+(i,0,1)$
2	1	$P_2 2t_d$	0	$D_a^+(i,2,0)$
2	2	$P_2 t_d$	$P_2 t_d$	$D_a^+(i,1,1)$
2	3	0	$P_2 2t_d$	$D_a^+(i,0,2)$
n	$1 \le r \le n+1$	$P_2[n+1-r]t_d$	$P_2[r-1]t_d$	$D_a^+(i,n+1-r, r-1)$

Table 5.2. Coordinates for the anti-echo data points that map directly into octant 1.

Mapping of the Echo Data

The mapping for the echo data differs from the anti-echo mapping in that the echo data points map both above and below the $l = 0$ plane. The points that originally mapped into the lower half of the phase space are inverted into the upper half before interpolation and Fourier transformation. Thus, two sets of data appear on each plane (Fig. 5.15); set *a* corresponds to the data points that map directly onto the plane; set *b* corresponds to the points that map through spatial inversion. According to Table 5.1, set *a* of octant 2 contains D_e^+ data points, while set *b* contains D_e^{-*} data points that originally mapped into octant 8 but were complex conjugated and inverted into octant 2. Likewise, set *a* of octant 4 contains D_e^- data points, while set *b* contains D_e^{+*}. The echo data mapping also differs in that the plane with the fewest data points is the highest isotropic plane (Fig. 5.15a), so we will begin analysis of the echo data coordinates by examining the mapping onto octant 2 with $l = N$ and proceeding to lower l planes.

For the echo data $p = -1$, so Eq. 5.22 becomes

$$l = -j + k. \tag{5.29}$$

On the $l = N$ plane (Fig. 5.15a), D_e^+ data points in set *a* satisfy Eqs. 5.21 and 5.28 only if $j = 0$. Substituting $j = 0$ into Eq. 5.23, the coordinates for $D_e^+(i,0,N)$ on the plane become

$$\begin{aligned} \tau_1 &= 0 \\ \tau_2 &= P_2(\cos\theta_i)Nt_d. \end{aligned} \tag{5.30}$$

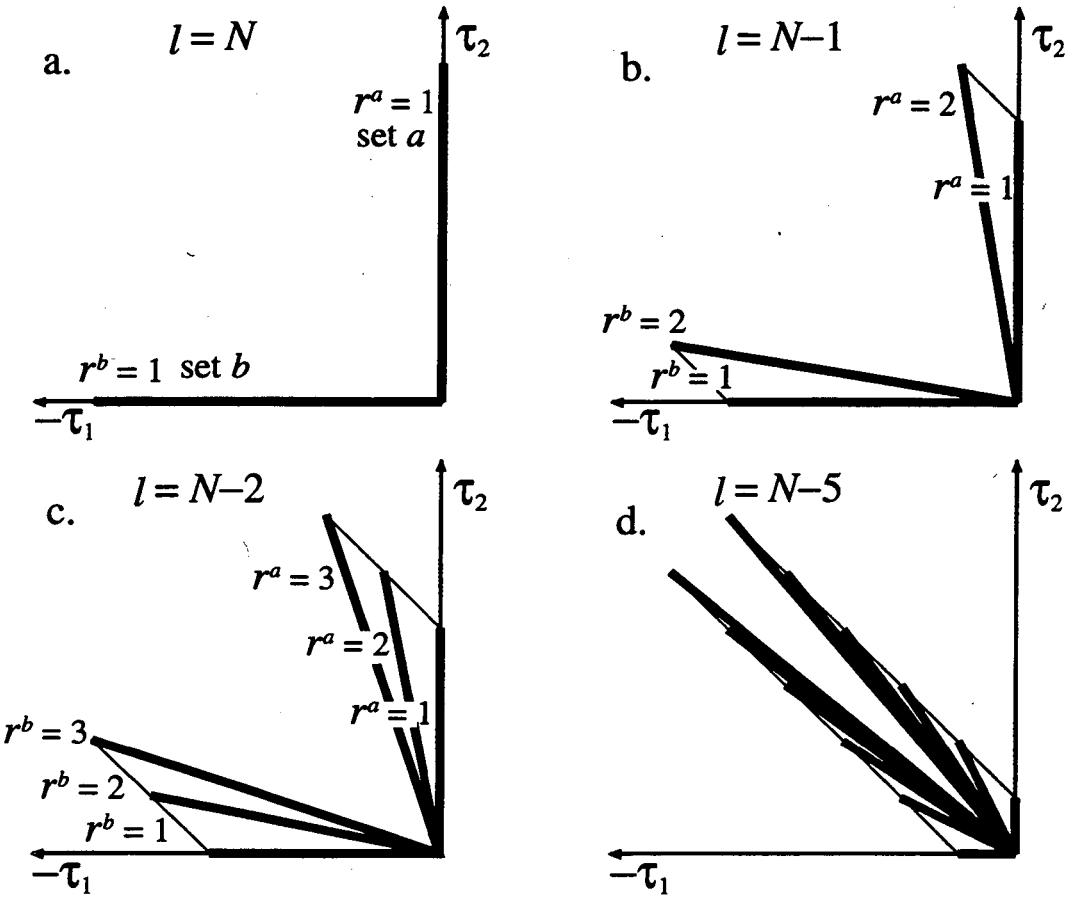

Figure 5.15 Mapping of the echo data D_e^{-*} and D_e^{+} onto octant 2. The planes are shown in *descending* order from the highest isotropic plane at $l = N$. The data in this octant are separated into two sets. Set a contains the D_e^{+} data that map directly onto the octant. Set b contains the D_e^{-*} data that map into octant 2 through complex conjugation and spatial inversion of D_e^{-} that originally mapped into octant 8. The rays of data in set a are indexed by r^a and are numbered counterclockwise starting from the $+\tau_2$ axis; the rays in set b are indexed by r^b and are numbered clockwise starting from the $-\tau_1$ axis. The data points that map onto this octant and their coordinates are given in Tables 5.3 and 5.4 and are discussed in the text. (a) $l = N$ plane. Two rays of data appear on this plane. The D_e^{+} data that have evolved with $j = 0$ and $k = N$ map onto the $+\tau_2$ axis. The D_e^{-*} data that have evolved with $j = N$ and $k = 0$ map onto the $-\tau_1$ axis. (b) $l = N - 1$ plane. Two rays appear on this plane for each set of data. The two rays in set a correspond to the two possible combinations of t_1 and t_2 dwell times that satisfies the condition $-j + k = N - 1$. The two rays in set b require the dwell time combinations to satisfy $-j + k = -(N - 1)$. (c) $l = N - 1$ plane. There are three rays for each set of data. The three rays in set a correspond to the three possible combinations of t_1 and t_2 dwell times that satisfy $-j + k = N - 2$. The three rays in set b require the dwell time combinations to satisfy $-j + k = -(N - 2)$. (d) $l = N - 1$ plane. With each decrement of l, an additional ray appears for each set of data. However the area of phase space the data covers becomes smaller at the lower planes until at $l = 0$ all the rays collapse onto a single line at $\tau_2 = -\tau_1$.

The data points in set b originally mapped into the $l=-N$ plane of octant 8, requiring $j=N$ and the coordinates

$$\begin{aligned}\tau_1 &= N\left|P_2(\cos\theta_i)\right|t_d \\ \tau_2 &= 0.\end{aligned} \tag{5.31}$$

With complex conjugation and spatial inversion of coordinates, $(\tau_1,\tau_3,\tau_3)\rightarrow(-\tau_1,-\tau_3,-\tau_3)$, the $D_e^{-*}(i,N,0)$ points map onto the $l=N$ plane with the final coordinates

$$\begin{aligned}\tau_1 &= -N\left|P_2(\cos\theta_i)\right|t_d \\ \tau_2 &= 0.\end{aligned} \tag{5.32}$$

The data in set a can be seen in Fig. 5.15a to form a ray along the τ_2 axis, while the data in set b forms a ray along the $-\tau_1$ axis.

On the $l=N-1$ plane (Fig. 5.15b), set a contains two rays of data corresponding to $j=0,1$. For $j=0$, $D_e^{+}(i,0,N-1)$ map onto this plane with the coordinates

$$\begin{aligned}\tau_1 &= 0 \\ \tau_2 &= P_2(\cos\theta_i)(N-1)t_d,\end{aligned} \tag{5.33}$$

while for $j=1$, $D_e^{+}(i,1,N)$ have the coordinates

$$\begin{aligned}\tau_1 &= -P_2(\cos\theta_i)t_d \\ \tau_2 &= P_2(\cos\theta_i)Nt_d.\end{aligned} \tag{5.34}$$

Likewise, set b on this plane also contains two rays of data, corresponding to the points that originally mapped into the $l=-(N-1)$ plane with $j=N-1,N$. After the final transformation, $D_e^{-*}(i,N-1,0)$ map onto the $l=N-1$ plane with the coordinates

$$\tau_1 = -|P_2(\cos\theta_i)|(N-1)t_d$$
$$\tau_2 = 0, \tag{5.35}$$

while $D_e^{-*}(i,N,1)$ have the coordinates

$$\tau_1 = -|P_2(\cos\theta_i)|Nt_d$$
$$\tau_2 = |P_2(\cos\theta_i)|t_d. \tag{5.36}$$

On the $l = N-2$ plane (Fig. 5.15c), set a contains three rays of data corresponding to $j = 0, 1, 2$, and set b also contains three rays of data corresponding to $j = N-2, N-1, N$. The data points and coordinates on this plane are given in Tables 5.3 and 5.4. In general the $l = n$ plane has a total of $N - n + 1$ rays of data for each of the two sets, a and b. Fig 5.15 shows the rays of data in set a indexed by r^a and numbered counter-clockwise from the $+\tau_2$ axis; rays in set b are indexed by r^b and numbered clockwise from the $-\tau_1$ axis. In the $l = n$ plane, each ray in set a contains the data points $D_e^{+}(i, r^a - 1, n - 1 + r^a)$ with the coordinates

$$\tau_1 = -P_2(\cos\theta_i)(r^a - 1)t_d$$
$$\tau_2 = P_2(\cos\theta_i)(n + r^a - 1)t_d, \tag{5.37}$$

while each ray in set b contains $D_e^{-*}(i, n-1+r^b, r^b - 1)$ with the coordinates

$$\tau_1 = -|P_2(\cos\theta_i)|(n + r^b - 1)t_d$$
$$\tau_2 = |P_2(\cos\theta_i)|(r^b - 1)t_d. \tag{5.38}$$

$l=-j+k$	r^a	$\tau_1=-P_2jt_d$	$\tau_2=P_2kt_d$	Data Points $D_e^+(i,j,k)$
N	1	0	P_2Nt_d	$D_e^+(i,0,N)$
$N-1$	1	0	$P_2[N-1]t_d$	$D_e^+(i,0,N-1)$
$N-1$	2	$-P_2t_d$	P_2Nt_d	$D_e^+(i,1,N)$
$N-2$	1	0	$P_2[N-2]t_d$	$D_e^+(i,0,N-2)$
$N-2$	2	$-P_2t_d$	$P_2[N-1]t_d$	$D_e^+(i,1,N-1)$
$N-2$	3	$-P_22t_d$	P_2Nt_d	$D_e^+(i,2,N)$
n	$1\le r^a$ $\le N-n+1$	$-P_2[r^a-1]t_d$	$P_2[n+r^a-1]t_d$	$D_e^+(i,r^a-1,$ $n+r^a-1)$

Table 5.3. Coordinates for the echo data points with $P_2 \ge 0$ that map directly into octant 2.

$l=-j+k$	r^b	$\tau_1=-\lvert P_2\rvert jt_d$	$\tau_2=\lvert P_2\rvert kt_d$	Data Points $D_e^{-*}(i,j,k)$
N	1	$-\lvert P_2\rvert Nt_d$	0	$D_e^{-*}(i,N,0)$
$N-1$	1	$-\lvert P_2\rvert[N-1]t_d$	0	$D_e^{-*}(i,N-1,0)$
$N-1$	2	$-\lvert P_2\rvert Nt_d$	$\lvert P_2\rvert t_d$	$D_e^{-*}(i,N,1)$
$N-2$	1	$-\lvert P_2\rvert[N-2]t_d$	0	$D_e^{-*}(i,N-2,0)$
$N-2$	2	$-\lvert P_2\rvert[N-1]t_d$	$\lvert P_2\rvert t_d$	$D_e^{-*}(i,N-1,1)$
$N-2$	3	$-\lvert P_2\rvert Nt_d$	$\lvert P_2\rvert 2t_d$	$D_e^{-*}(i,N,2)$
n	$1\le r^b$ $\le N-n+1$	$-\lvert P_2\rvert[n+r^b-1]t_d$	$\lvert P_2\rvert[r^b-1]t_d$	$D_e^{-*}(i,n+r^b-1,$ $r^b-1)$

Table 5.4. Coordinates for the echo data points with $P_2 \le 0$ that map into octant 2 through complex conjugation and spatial inversion.

The mapping into octant 4 is identical to that of octant 2 except that the arrays are swapped, $D_e^{-*} \rightarrow D_e^{+*}$ and $D_e^{+} \rightarrow D_e^{-}$, and the coordinates undergo a sign change $(\tau_1, \tau_2) \rightarrow (-\tau_1, -\tau_2)$. Tables 5.3 and 5.4 summarize the results of this subsection.

Interpolation

Once the coordinates are calculated, the experimental data on each isotropic plane must be interpolated onto a Cartesian grid. Only the points within the shaded bounds of Fig. 5.12 are interpolated. Any Cartesian grid point p within this region is bounded by two rays of data, and thus four nearest neighbor experimental data points can be obtained, two on each ray (Fig. 5.16). Any combination of three of these data points forms a plane in the 3D spaces defined by the coordinates $(\mathrm{Re}\, D, \tau_1, \tau_2)$ and $(\mathrm{Im}\, D, \tau_1, \tau_2)$, where

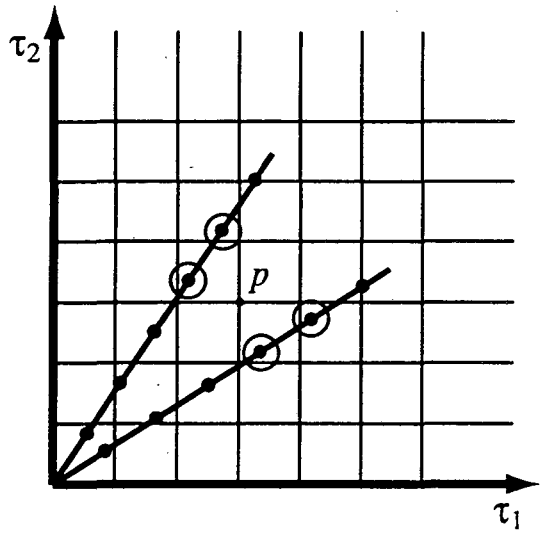

Figure 5.16. Interpolation of the data points onto a Cartesian grid. All the data points lie on one of the $t_2 + t_1$ planes. So a 2D interpolation is required on each of the planes. Only the points within the shaded regions of Fig. 5.12 are interpolated. In this region, each point on the Cartesian grid is bounded by two rays of experimental data. Four nearest neighbor points are chosen from the two rays to interpolate the Cartesian point p as discussed in the text.

$\mathrm{Re}D$ and $\mathrm{Im}D$ are the real and imaginary parts of the complex data points. By successively ignoring one of the extra points of the original four, real and imaginary planes may be constructed in four ways. The interpolated value at point p is assigned the average complex value of the intersecting real and imaginary planes at the coordinates of point p.

5.4.3 Experimental

The 3D VACSY-T exchange spectrum was recorded on a 7.07 T, home built spectrometer, interfaced to a TECMAG pulse programmer. Modifications were made to the basic variable angle probe design[14] to allow for variable temperature control, as described in chapter 6. The angle of the spinner axis was adjusted by a Whedco stepping motor and a computerized motor controller that allowed angles to be set to within 0.1°.

A sample of ordered iPP (Hostalen PP) $\left(\left[-CH_2CH-(CH_3)-\right]_n\right)$ was obtained from Hoechst AG (Frankfurt, Germany). The sample was cut into discs and placed inside the spinner with the draw axis perpendicular to the axis of rotation.

Each variable angle spinning exchange experiment was obtained at 360 °K with a mixing time of 1s and a recycle delay of 1s. A conventional ^{13}C cross-polarization sequence was used with ^{1}H decoupling during the t_1 and t_2 time periods.[15] Phase cycling[16] was used to select the $-1 \rightarrow 0 \rightarrow +1$ and $+1 \rightarrow 0 \rightarrow +1$ pathways, and the data sets were recorded separately. The rotation axis angle, θ, was again restricted to the range $90° \geq \theta \geq 35.3°$. Altogether 31 different 2D exchange experiments were recorded at angles corresponding to the P_2 values of

$$P_2(\cos\theta_k) = -0.5 + (k-1)/30 \qquad k = 1,\ldots,31. \tag{5.39}$$

Both t_1 and t_2 dwell time increments were set to $166.7\mu s$. 128 points were acquired in t_2 while the number of points acquired in t_1 varied with the angle at which the 2D exchange experiment took place. For the experiments recorded in the range $59^\circ \geq \theta \geq 52^\circ$, 128 t_1 points were acquired, while for the experiments in the ranges $51^\circ \geq \theta \geq 35.3^\circ$ and $90^\circ \geq \theta \geq 60^\circ$, 64 t_1 points were acquired, since the FIDs decay faster at these latter angles. Only one FID is required at the magic angle, $\theta = 54.74^\circ$, where all the anisotropic terms disappear. Each FID was signal averaged for 40 scans, and the total data acquisition time for the 3D experiment was four days. The data were then transferred to a Silicon Graphics R4000 computer where each 2D experiment was zero-filled to a 128x128 matrix and then mapped and interpolated onto a 128^3 cube. The data was then Fourier transformed to obtain the 3D exchange spectrum.

5.4.4 Results

Ordered iPP was used to enhance the appearance of the off-diagonal exchange patterns in demonstrating the 3D VACSY-T exchange experiment. The ordering of the sample is reflected in distinct anisotropic line shapes that are modified from powder patterns as discussed in chapter 4.

The effect of molecular reorientation on the 2D exchange patterns for each carbon site of iPP is clearly seen in Figs. 5.17a and 5.17b, which were obtained using mixing times of 1 ms and 1s respectively. Since no significant molecular reorientation has occurred during the short mixing delay, the spectra in Figs. 5.17a show only diagonal ridges. Note that such short mixing delays are not technically achievable in the VACSY-S experiment due to the duration of the rotor flips during the mixing time. The spectra in Figs. 5.17b reveal distinct off-diagonal ridge patterns, reflecting the molecular reorientation

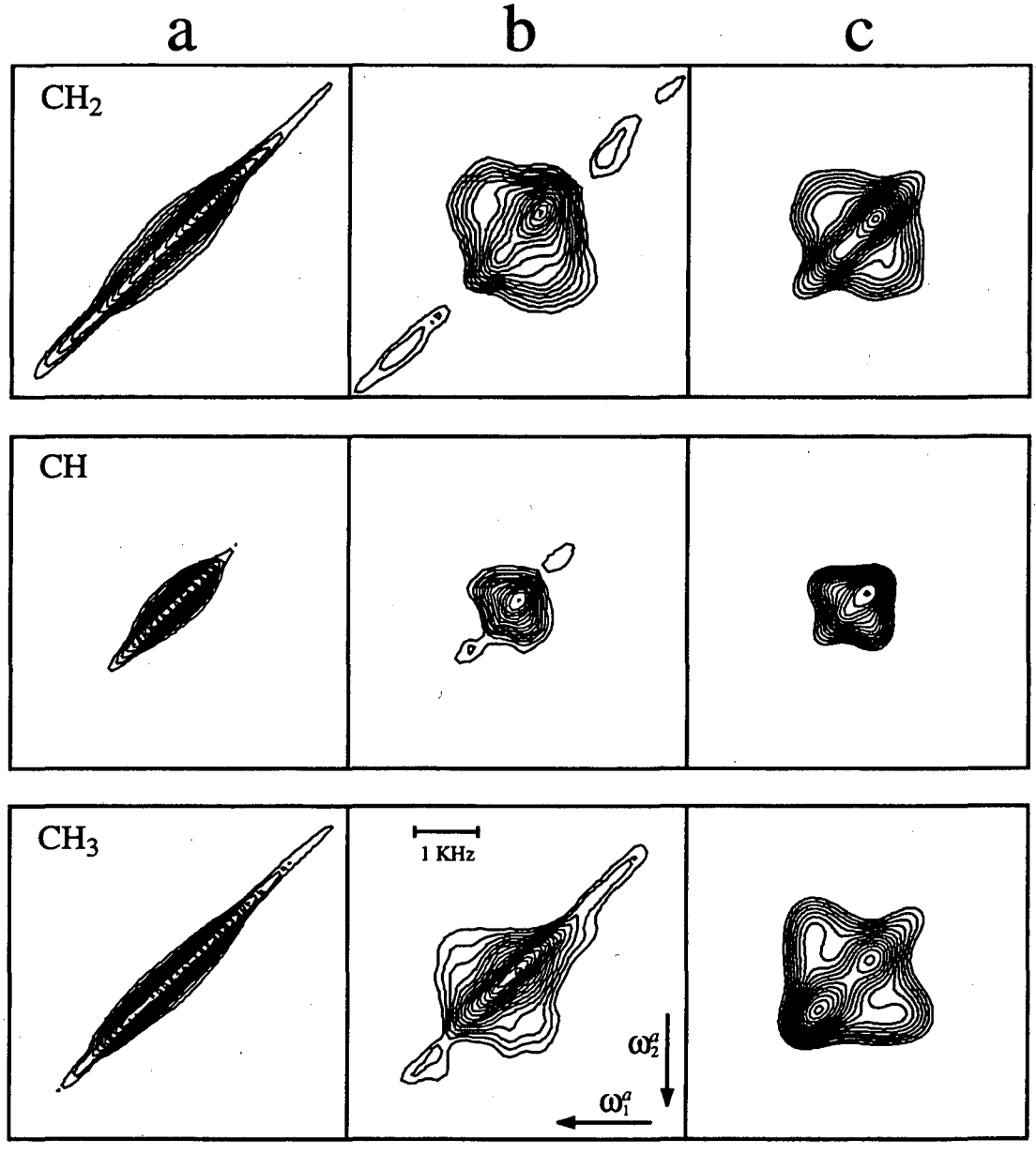

Figure 5.17 Experimental 2D exchange patterns for the three sites of ordered iPP obtained from the 3D VACSY-T exchange experiment at T = 360° K. (a) 3D VACSY-T exchange data with t_m = 1ms. (b) 3D VACSY-T exchange data with t_m = 1s. (c) Simulations of 2D exchange patterns for each site of iPP, using 120° jumps about the helix axis with a correlation time $\tau_c < t_m$.

which occurred during the long mixing delay. Simulations shown in Fig. 5.17c, using 120° helical jumps with $\tau_c < t_m$, show good agreement with the experimental data. In particular both the experimental and simulated spectra for the methylene and methine carbons reveal the elliptical ridge patterns indicative of discrete molecular motion.[17] The exchange pattern for the methyl carbon shows significant discrepancy between experiment and simulation. However, the methyl line shape distortion is also seen in the 2D VACSY patterns (not shown) obtained by Fourier transforming either the $\tau_1 = 0$ or the $\tau_2 = 0$ slice from the full 3D VACSY-T time domain matrix as discussed above. Thus we attribute the distortion in the methyl carbon exchange pattern is not due to the procedure of the experiment but rather due to a strong spectral component from the amorphous regions of the polymer at higher temperatures.[9]

Artifacts that appear as ridges along the diagonal in the exchange patterns, however, are inherent to the experiment and arise from incomplete sampling of the Fourier space, as seen in Fig. 5.12. Filling these holes would require refocusing only the anisotropic frequency during t_2 evolution and would involve a hop of the rotor in between the t_1 and t_2 evolution periods, nullifying the main advantage of the 3D VACSY-T exchange experiment. Artifacts due to incomplete sampling of Fourier space are also seen in 2D VACSY, but these artifacts can be removed by using linear prediction to fill in the missing data as shown in chapter 3. We are currently exploring other processing methods that may be suitable for improving the quality of the 3D VACSY-T exchange spectrum. However, despite the artifacts, distinct patterns revealing discrete jump motions can be clearly seen in the exchange spectrum for two of the three chemical sites in iPP in good agreement with simulations. The quality of the spectra is such that, in the case of an unknown motional mechanism, the spectral patterns can be used, in conjunction with simulations, to identify incorrect motional models and verify the correct mechanisms.

5.4.5 Conclusion and Outlook

We have demonstrated a new extension of the VACSY technique for high resolution studies of slow molecular motion which eliminates the need for rapid reorientation of the sample rotor. This new technique is based on the same basic principle as the original 2D VACSY and 3D VACSY-S exchange experiments: the change in the rotation axis of a rapidly spinning sample with respect to the static magnetic field, $\mathbf{B}_0$, scales the anisotropic frequencies but leaves the isotropic frequencies invariant. By acquiring a series of 2D exchange experiments at different rotation axes, the time domain data may be mapped onto a 3D matrix such that a fast Fourier transformation directly yields isotropic-anisotropic correlations. There are two main features particular to 3D VACSY-T exchange. By removing the requirement for the rotor hop, experimental difficulties have been shifted from the hardware and mechanical aspects of the experiment to the software and data processing, which is generally preferable given continued advances in software and computer technology. The experiment also removes restrictions on the length of the t_m mixing delay and opens up the possibility for studying the full range of dynamical rates in the slow motional regime. This study also further demonstrates how a redefinition of the generalized time variables, τ_i, in terms of adjustable experimental parameters can lead to novel experimental approaches.

References

1. I. M. Ward, *Mechanical Properties of Solid Polymers*; Wiley, New York, 1971.

2. R. T. Bailey, A. M. North, and R. A. Pethride, *Molecular Motions in High Polymers*; Clarendon, Oxford, U.K., 1981.

3. S. Wefing, and H. W. Spiess, J. Chem. Phys., **89**, 1219 (1988).

4. A. Hagermeyer, K. Schmidt-Rohr, and H. W. Spiess, Adv. Magn. Reson., **13**, 85 (1989).

5. A. Hagermeyer, L. Brombacher, K. Schmidt-Rhor, and H. W. Spiess, J. Chem. Phys., 583 (1990).

6. C. Schmidt, S. Wefing, B. Blumich, and H. W. Spiess, Chem. Phys. Lett., **130**, 84 (1986).

7. D. Schaefer, and H. W. Spiess, J. Chem. Phys., **97**, 7944 (1992).

8. N. G. McCrum, B. E. Read, and G. Williams, *Anelastic and Dielectric Effects in Polymeric Solids*; Wiley, New York, 1967.

9. D. Schaefer, H. W. Spiess, U. W. Suter, and W. W. Fleming, Macromolecules, **23**, 3431 (1990).

10. L. Frydman, Y. K. Lee, L. Emsley, G. C. Chingas, and A. Pines, J. Am. Chem. Soc., **115**, 4825 (1993).

11. P. T. Callaghan, and C. D. Eccles, J. Magn. Reson., **71**, 426 (1987).

12. R. R. Ernst, G. Bodenhausen, and A. Wokaun, *Principles of Nuclear Magnetic Resonance in One and Two Dimensions*; Clarendon Press, Oxford, 1987.

13. D. J. States, R. A. Haberkorn, and D. J. Ruben, J. Magn. Reson., **48**, 286 (1982).

14. M. A. Eastman, P. J. Grandinetti, Y. K. Lee, and A. Pines, J. Magn. Reson., **98**, 333 (1992).

15. A. Pines, M. G. Gibby, and J. S. Waugh, J. Chem. Phys., **59**, 569 (1973).

16. G. Bodenhausen, H. Kogler, and R. R. Ernst, J. Magn. Reson., **58**, 370 (1984).

17. S. Wefing, S. Kaufmann, and H. W. Spiess, J. Chem. Phys., **89**, 1234 (1988).

Chapter 6 Hardware

6.1 Epsilon Spectrometer

6.1.1 Homodyne and Heterodyne Architecture

The Epsilon, unlike most NMR spectrometers, incorporates a homodyne rather than a heterodyne architecture. The basic difference between these two systems is illustrated in Fig. 6.1. In a heterodyne system, most of the signal manipulation occurs at a set intermediate frequency (IF). The IF signal is amplified and phase shifted in the transmitter then mixed with a local oscillator (LO) signal such that one of the resultant rf frequencies,

$$f_{RF} = f_{LO} \pm f_{IF} \tag{6.1}$$

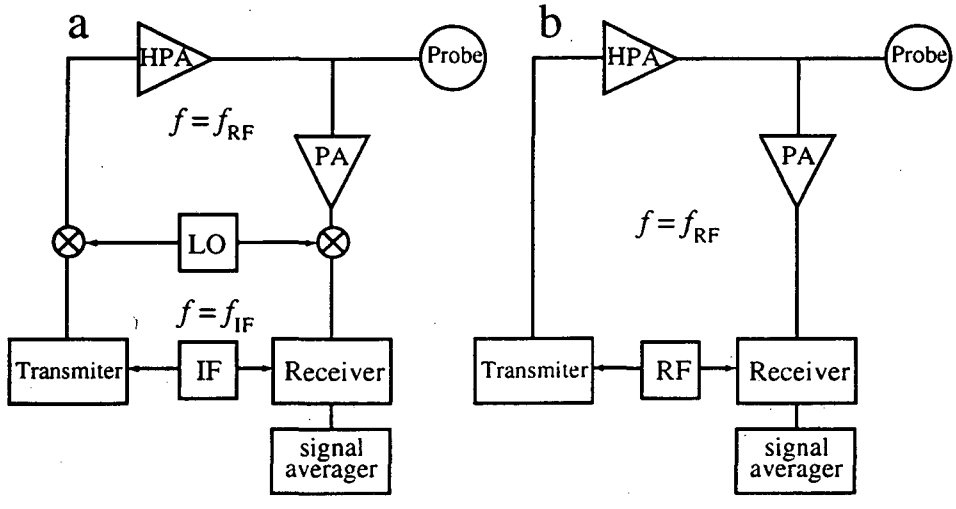

Figure 6.1. Two different NMR spectrometer architectures. HPA and PA are the high power amplifier and the pre-amp. IF, LO, and RF are the intermediate frequency, local oscillator, and the radio frequency (resonant frequency) signal generators, respectively (a) Heterodyne spectrometer. (b) Homodyne spectrometer.

is the nuclear resonant frequency. On the receiver side of a heterodyne system, the signal from the pre-amp is mixed back to the IF for further amplification and filtering. Thus only the high-power amplifier and the pre-amp are required to be broadband in order for the spectrometer to observe different nuclei. In contrast, a homodyne system has no IF or LO frequencies. All high frequency amplification, filtering and phase shifting occurs at the resonant frequency; thus all rf components must be broadband.

The main advantage of a homodyne system is its inherent simplicity; fewer rf components are needed and since only one rf signal should be in the system, debugging and removal of parasitic signals are simplified. The main disadvantage of a homodyne system is the broadband requirement for all rf components, making some of the components more expensive and some of the rf signal procedures such as phase shifting more difficult. In addition, since there is no active filtering in the broadband receiver, care must be taken to ensure that transient signals do not saturate the rf components.

Figure 6.2 shows a block schematic of the Epsilon spectrometer set up for double resonance experiments with observation of the X channel frequency. Further details on each of the stages of the spectrometer will be presented in the following sections.

6.1.2 Transmitter

Proton Channel Transmitter

A block diagram of the H transmitter is shown in Fig. 6.3. The rf signal from the PTS 500 frequency generator is split by a Mini-Circuits ZDC 10-1 directional coupler. The output terminal of the coupler is connected to the receiver, while the couple terminal is connected to the quadrature phase shifter (described below). Two amplifiers,

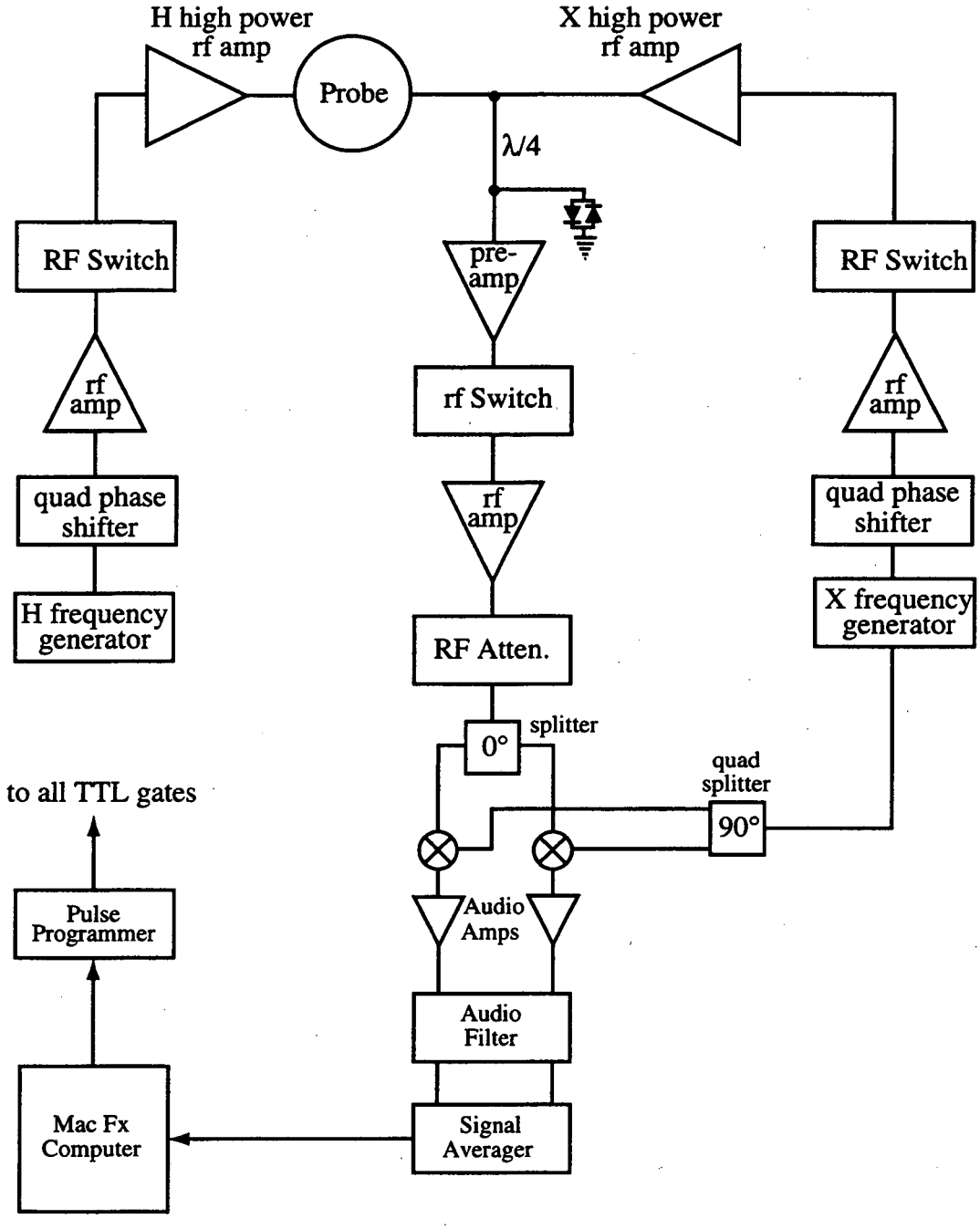

Figure 6.2 Block schematic of the Epsilon homodyne spectrometer. The diagram shows the spectrometer set up for double resonance and observation on the X channel. a 1/4 wave λ cable and a set of signal cross diodes to ground act as a duplexer to protect the pre-amp from high power rf radiation.

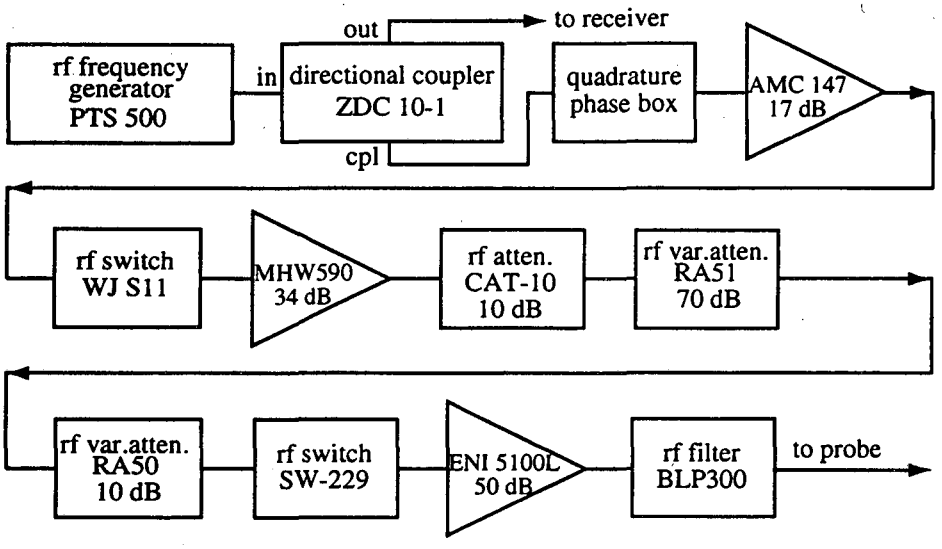

Figure 6.3. Block diagram of the Proton channel transmitter.

the Anzac AMC 147 (17 dB) and the Motorola MHW590 (34 dB), are used in the low power amplification stages of the transmitter. The rf switches, Watkins-Johnson WJS11 and MA-Com SW229, provide a combined isolation of 90 dB. Two Trilithic rotary rf attenuators control the amplitude of the transmitter signal; the RA51 varies from 0 to 70 dB in steps of 10 dB; the RA50 varies from 0 to 10 dB in steps of 1dB. The final high power amplification is provided by a class A broadband ENI 5100L amplifier (2-500 MHz, 50dB, 100W). An additional fixed attenuator, Mini-Circuits CAT-10 (10 dB), ensures that the maximum input into the 5100L never exceeds 1v rms. A high power K&L BLP300 bandpass filter, removes the broadband noise from the 5100L before the rf signal is sent to the probe. Often the 5100L cannot provide the decoupling power needed; in this case, a Creative Electronics CE300 (5dB, 500 W) tuned amplifier is added after the bandpass filter. Five TTL lines control the H transmitter: four lines control the rf phase, and the fifth controls the rf switches.

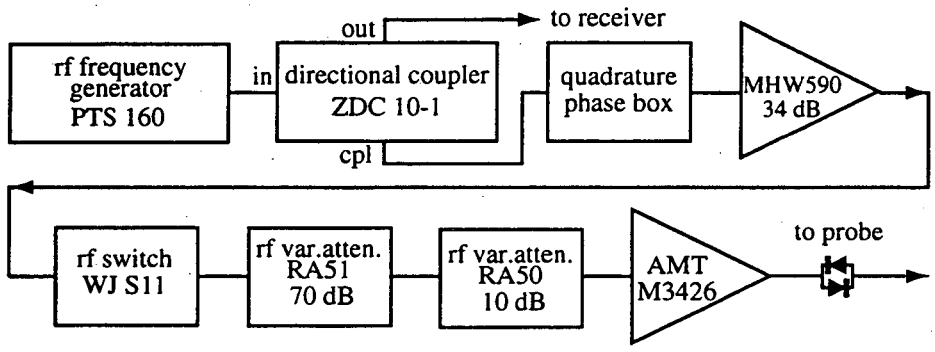

Figure 6.4. Block diagram of the X channel transmitter.

X Channel Transmitter

The same rf components in the H transmitter are also used in the low power stages of the X transmitter (Fig. 6.4). The only difference is that the frequency is generated by a PTS 160 and only one amplifier and rf switch is used. The high power amplifier is an AMT M3426 (2-100 MHz, 60 dB, 1000 W). As with the H transmitter, five TTL lines control the rf phases and switch. An additional TTL line is used to gate the M3426 to minimize the amplifier noise output during detection. A set of signal cross diodes further reduces the amplifier noise.

Quadrature Phase Shifter

Broadband phase shifting in increments of 90° is obtained by a home built quadrature phase shifter (Fig. 6.5). Details of the phase shifter design have been presented elsewhere.[1] Only the principles of the phase shifter and present circuit diagrams which have been slightly modified from the original design will be reviewed here. A broadband quad splitter (Olectron 0-J3-2061) separates the input rf signal into 0° and 90° components. The amplitude of each of the components is controlled by a DC voltage supplied to the IF

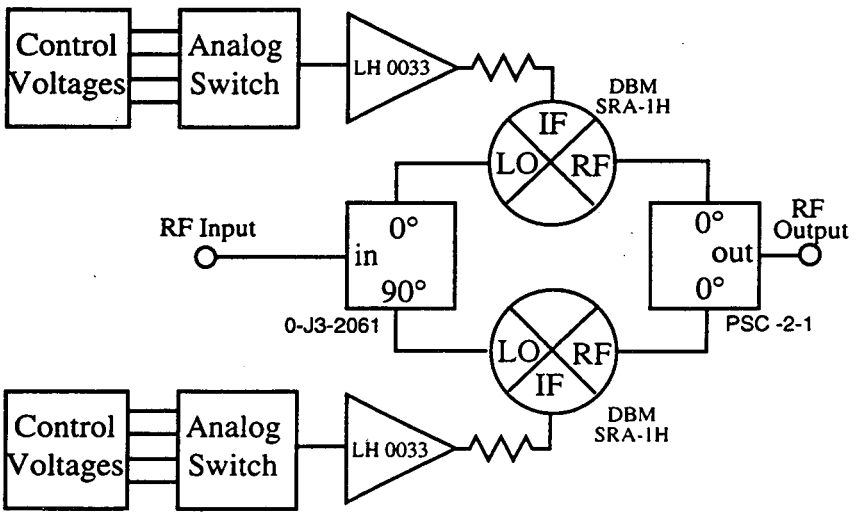

Figure 6.5 Block diagram of the quadrature phase shifter

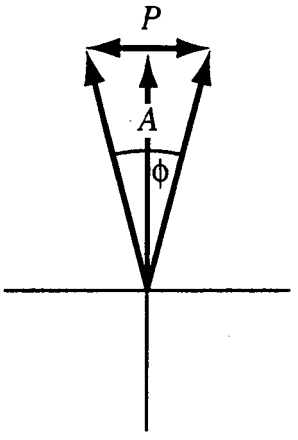

Figure 6.6 Phase diagram of the rf output of the quadrature phase shifter. The larger, *A*, component of the signal determines the overal amplitude of the rf signal. The smaller, orthogonal, *P*, component adjusts the phase of the signal.

port of a Mini-Circuits SRA-1H double balanced mixer (DBM). Here, the DBMs act as voltage controlled variable attenuators. One of the mixers is driven strongly and provides a large rf output; the other is driven weakly and provides a small rf output orthogonal to the stronger signal. Figure 6.6 shows that when the two orthogonal outputs of the mixers are then combined vectorially through a Mini-Circuit PSC-2-1 splitter, the stronger component (designated in the figure by *A*) provides the overall amplitude, while the weaker component (designated in the figure by *P*) controls the overall phase of the signal. As long as the *P* component remains much smaller than the *A* component, the amplitude and phase of the signal are controlled independently by each mixer.

The DC amplitude and phase control circuits used to drive the mixers are shown in Fig. 6.7. To minimize drift in the rf phase and amplitude, Analog Devices AD584 precision voltage references are used to maintain DC voltages for both the amplitude and phase control circuits. Figure 6.7a shows the A_x and A_y voltages are controlled with the AD584 set to +10 V, while the A_{-x} and A_{-y} voltages are controlled with the AD584 set to -10 V. Figure 6.8 shows the circuits used for each of the voltage references to obtain the desired output voltage. Conventional voltage followers (National Semiconductor LM310) are used to buffer the DC circuit. Figure 6.9 shows the wiring for the LM310 in a booster circuit to allow for larger negative current swings under load. The outputs of the LM310s are also shunted to ground through 0.1 μF capacitors to remove transients.

To allow for quick switching of the rf phases needed in multiple pulse experiments, fast switches (Harris Hl-201 HS), with on-off times < 50 ns and buffers (Élantec ELH0033) with rise times < 2 ns are used in the switching circuit shown in Fig. 6.10. The Hl-201 HS operates on inverse logic:

Logic	Switch
0	on
1	off

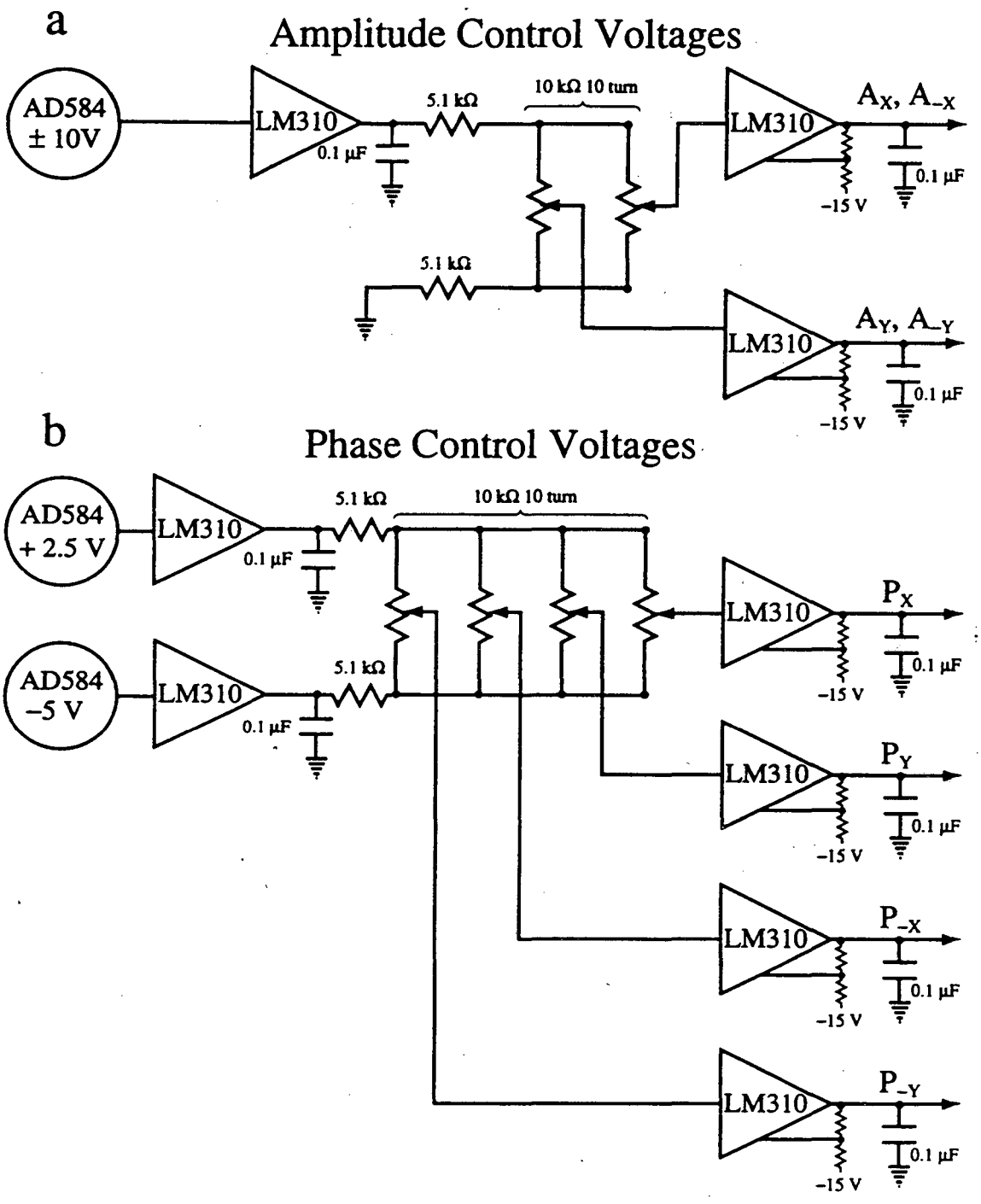

Figure 7. Control voltage circuits for the quadrature phase shifter. The DC voltage is provided by high precision AD584 voltage regulators, wired as shown in Fig. 8 to provide the different voltages. The LM310 buffers are wired with the booster circuit shown in Fig. 9. (a) Amplitude control voltages. A_x and A_y voltages are supplied with the AD584 set to +10 V, while A_{-x} and A_{-y} voltages are supplied with the AD584 set to -10 V. (b) Phase control voltages. The output phase voltages may be positive or negative and the magnitues of the voltages will be smaller than those of the amplitude voltages.

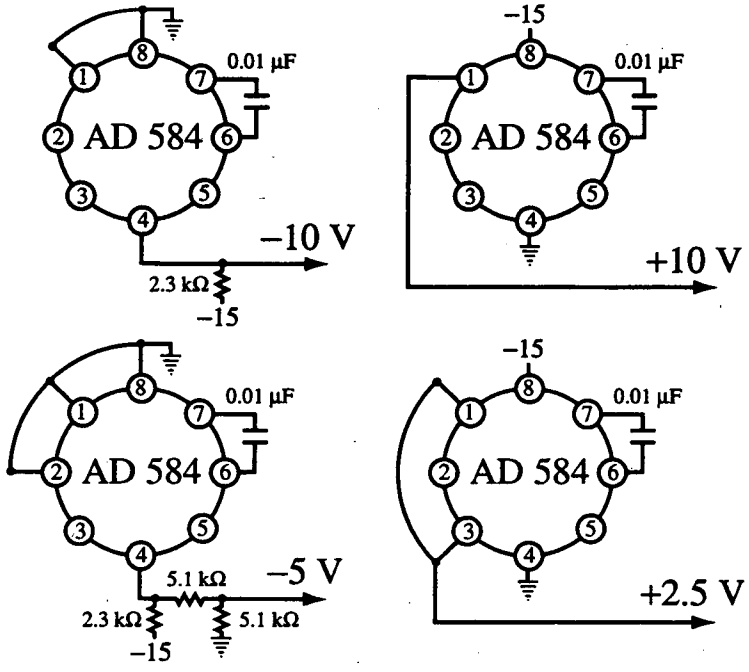

Figure 6.8 Circuits for the high precision voltage references, AD 584, used to provide ±10V, +2.5V and -5V for the control voltage circuits shown in Fig. 7.

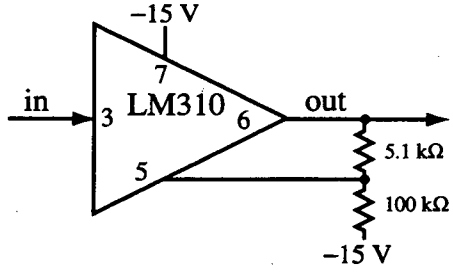

Figure 6.9 Booster circuit for the LM310 follower. The booster circuit allows for larger swings of negative current.

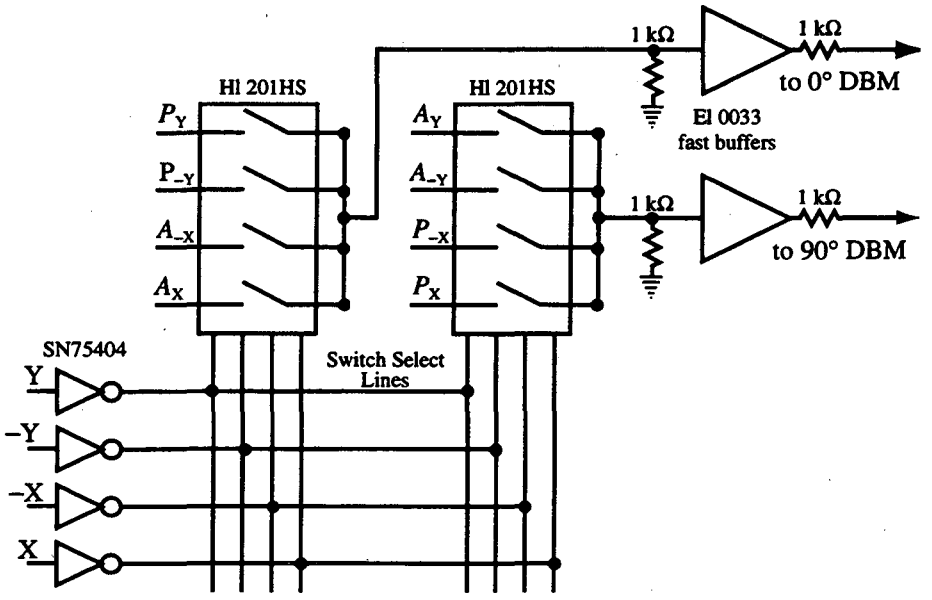

Figure 6.10 Diagram of the switching circuit for the quadrature phase shifter. The inputs into the HI 201HS switches are represented by the amplitude and phase voltages from Fig. 9. The switches are operated by inverted pulse programmer TTL pulses represented by the phase of the rf vector in the rotating frame (X,Y,–X,–Y). The outputs of the EI 0033 buffers are taken into the IF terminal of the double balanced mixers (DBM) shown in Fig. 5.

Pulse Programer TTL Logic	0° IF Voltage	90° IF Voltage	RF Phase
X=1	A_x	P_x	
Y=1	P_y	A_y	
–X=1	A_{-x}	P_{-x}	
–Y=1	P_{-y}	A_{-y}	

Table 6.1 Pulse programmer TTL pulses and their corresponding output voltages. When the particular TTL line in column 1 is set high all the others are set low. In all cases the paired amplitude and phase voltages from the buffers shown in Fig. 10 are output into the IF terminal of the DBMs. Column 3 shows the phase of the rf vector in the rotating frame, similar to Fig. 6.6.

Thus it was convenient to invert the TTL signal from the pulse programmer with hex inverters (Texas Instruments SN75404). The voltages supplied to the 0° and 90° mixers depending on the pulse programmer TTL logic are shown in Table 6.1.

Although the quadrature phase shifter operates broadband, the amplitudes and phases change for different frequencies. Thus the phase shifters should be calibrated for each frequency with a vector volt meter. Multiple pulse sequences are also available for more accurate calibrations.[2]

6.1.3 Receiver

Figure 6.11 shows the block diagram for the receiver. To minimize noise in the detected signal a Mitec AU1114 pre-amp with a noise figure of 2.0 dB is placed at the base of the magnet. A high isolation (90 dB) low transient Daico switch is used to keep the rest

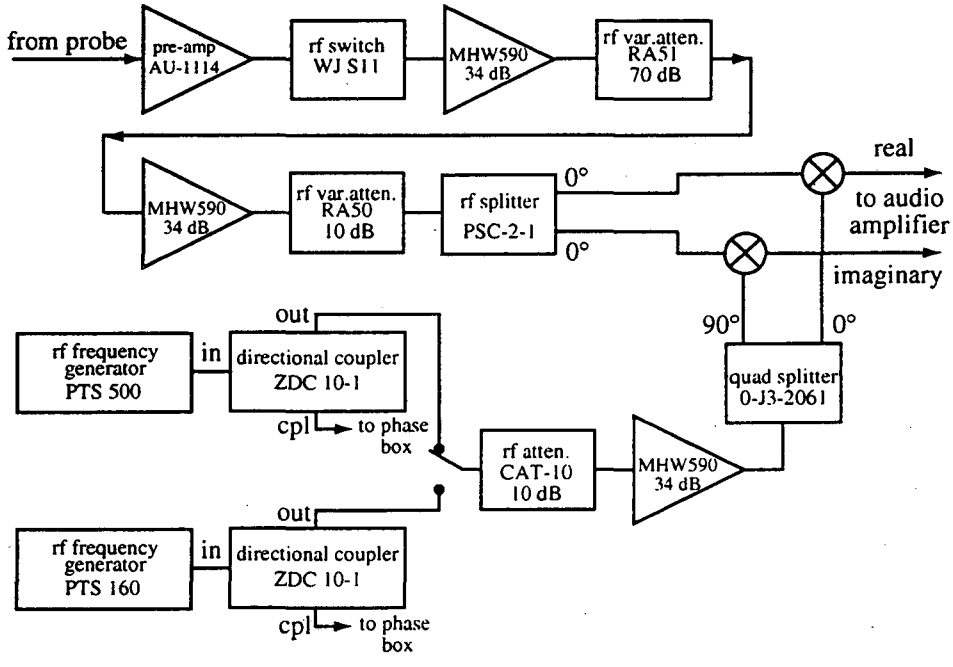

Figure 6.11. Block diagram of the Epsilon receiver.

of the receiver circuit from saturating during the high power rf pulses. Further amplification and attenuation are obtained by the MHW590 amp, RA51, and RA50 attenuators described in the transmitter section. Because the MHW590s are broadband amplifiers, any transient signal is amplified creating potential problems with saturation and receiver ring down. In such cases a low pass filter such as the Mini-Circuits BLP-100 before one or both of the MHW590s may help in removing the transient signal. The detected signal is then divided along the real and imaginary channels by a Mini-Circuit PSC-2-1 splitter. This rf signal must now be mixed with the observe frequency signal to remove the rf carrier frequency. The observe frequency signal is obtained from the output terminal of the directional coupler connected to either the H or X frequency generator. A BNC cable is used to switch between the two frequency generators. The observe frequency signal is then amplified and split in quadrature by a broadband Olectron 0-J3-2061 splitter. The output of the 0° terminal is mixed with the real channel signal (in a Mini-Circuits SRA-1H), while the output of the 90° terminal is mixed with the imaginary channel. The audio outputs of the mixers are then amplified by a low noise audio op-amp shown in Fig. 6.12. Three potentiometers control the audio amplifier circuit: R_1 controls the relative amplitude of the real and imaginary signal; R_2 and R_3 control the dc offsets for the real and imaginary channels respectively. After the audio amplifier, the signal is filtered by a Wavetek audio filter and then sent to the signal averager.

6.1.4 Pulse Programmer

A TECMAG Inc. pulse programmer, PULSkit, is used to control all of the TTL logic lines. The pulse programmer, originally for use with a DEC Micro VAX II computer, was modified to allow operations with a Macintosh II FX computer. PULSkit executes

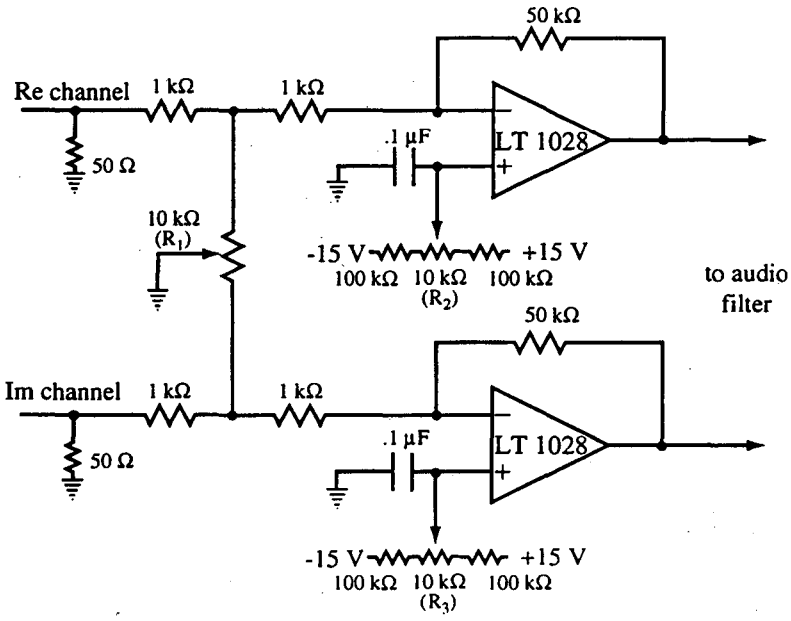

Figure 6.12. Audio amplifier Circuit. The potentiometer R_1 determines the relative amplitude of the real and imaginary channels. R_2 and R_3 determine the DC offset of the real and imaginary channels, respectively.

each step in a pulse sequence through a 128-bit microword, shown in Fig. 6.13 (if the pulse length is longer than 430s, two or more microwords will designate a single event). PULSkit can hold up to 2048 microwords in its memory for execution. Of the 128 bits, 68 are user defined and can be used for general operation of the spectrometer. The functions of the microword bits have been described fully elsewhere,[3] and I will only discuss the user control bits in the microword that are currently defined on the Epsilon spectrometer.

The TTL outputs of PULSkit are sent through a signal distribution box where they are connected to 74LS128 50Ω line drivers to allow access to the TTL lines through 50Ω BNC cables. The line driver circuit previously described[4] has been modified for the X and H phase bits to comply with the convention used by the MacNMR software. MacNMR uses two bits to designate the quadrature phases (0,1,2,3), while the signal distribution

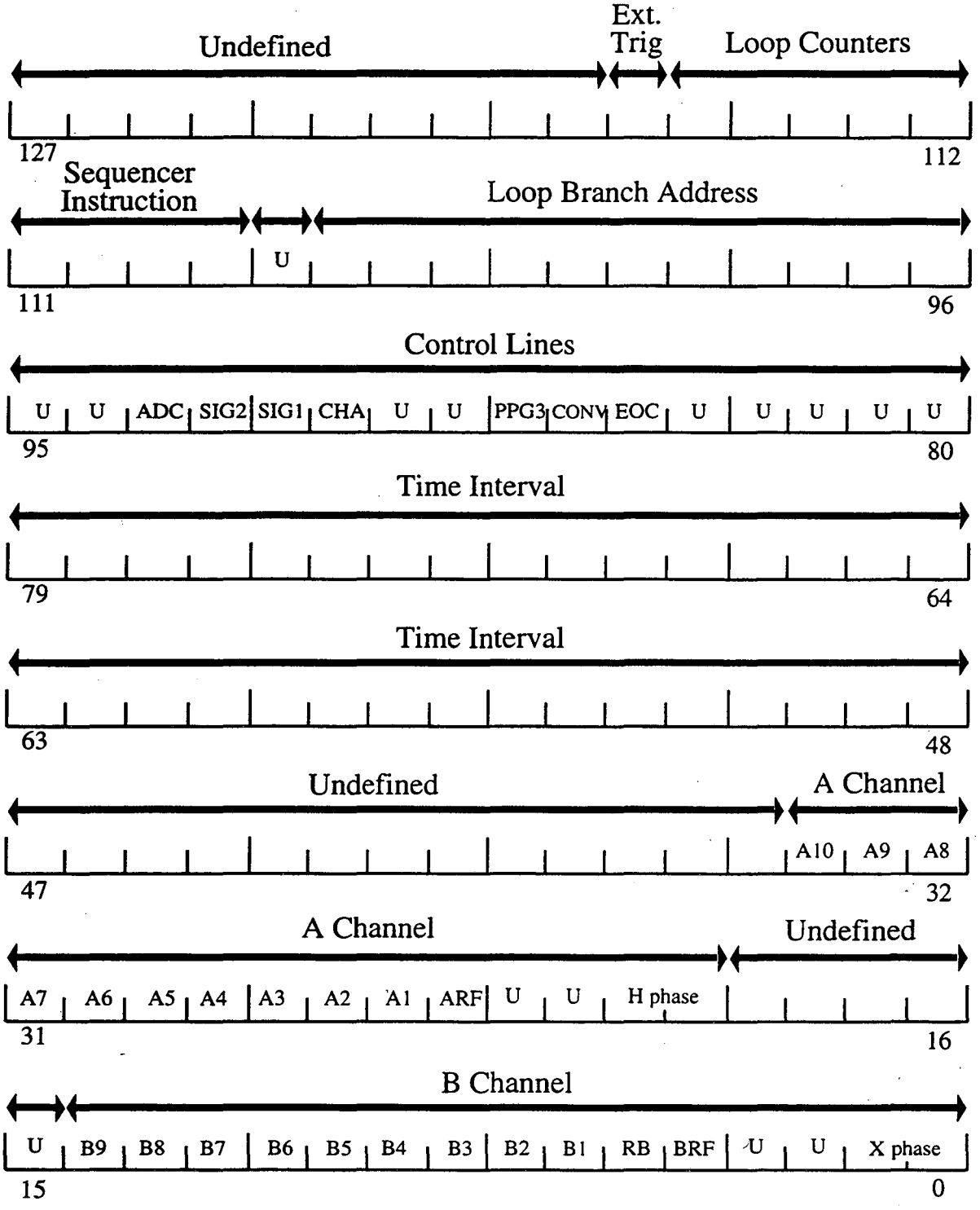

Figure 6.13 Microword bit assignments. Bits assigned in A Channel and B Channel are connected to line drivers and are available for general use. The bits designated as "Undefined" or "U" are user bits that are not currently connected to line drivers.

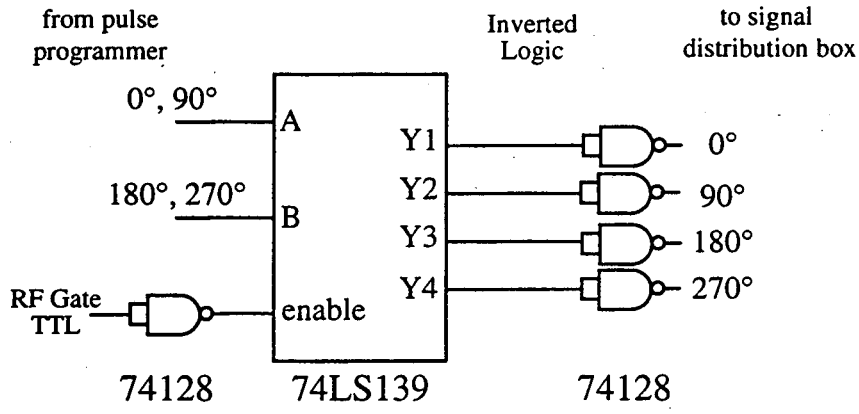

Figure 6.14. Circuit to convert from 2-bit logic to 4-bit logic. The 74128 chip is used to invert the TTL output of the 74LS139.

Enable	B	A	Y1	Y2	Y3	Y4
1	X	X	1	1	1	1
0	0	0	0	1	1	1
0	0	1	1	0	1	1
0	1	0	1	1	0	1
0	1	1	1	1	1	0

Table 6.2. Input and output TTL for the 74LS139.

box, originally built to work with the Micro Vax II, assumes 4 bit logic for the phases (1,2,4,8). Thus a 74LS139 chip (Fig. 6.14 and Table 6.2) is added prior to the line driver circuit to convert from 2 bit logic to 4 bit logic. The bits in the regions labeled as A Channel and B Channel are attached to drivers in the signal distribution box and are available for general purpose use on the spectrometer. The specific labeling of these bits corresponds to the labeling on the outputs of the signal distribution box. The bits labeled

row label	row number	microword starting bit	number of bits	future expansion	icon label	Spectrometer function
H	1	24	1	0000	TX	H transmitter switch
Hph	2	20	2	0000	PH	H quadrature phases
X	3	4	1	0000	TX	X transmitter switch
Xph	4	0	2	0000	PH	X quadrature phases
R	5	5	1	0000	TX	Receiver blanking
A1	6	25	1	0000	TX	High power transmitter blanking
A2	7	26	1	0000	TX	general TTL
A3	8	27	1	0000	TX	general TTL
B1	9	6	1	0000	TX	general TTL
B2	10	7	1	0000	TX	general TTL
RX	11	96	1	0000	RX	Constant receiver phase
SAr	12	87	1	0000	TX	Siganl averager reset
Mot	13	8	5	0000	GR	Stepper motor profile logic
Xtr	14	117	1	0000	TX	external pulse program trigger

Table 6.3. The current Config.con file used to define the microword bits for the Epsilon spectrometer.

"unused" may also be made available by constructing additional drivers for the pulse programmer.

All of the microword bits in current use on the Epsilon spectrometer are defined in the "config.con" file (Table 6.3) which must be contained in the MacNMR folder. The "SAr" row in Table 6.3 corresponds to the "PPG3" bit in Fig. 6.13 and is used to zero the signal averager memory. The "Mot" row corresponds to bits B3-B7 in Fig. 6.13 and are used to specify the motor profiles described below. The "Mot" line can be assigned any value from 0 to 31, and because it is defined by a "GR" (gradient) icon, its assigned value may be read in from a file (for further descriptions see the MacNMR manual).

6.2. Double-Tuned Hopping-Coil Probe

6.2.1 Probe Spinning Assembly

All of the VACSY experiments described in the previous chapters used a double-tuned hopping-coil design.[5] This design allows for higher sensitivity and rf field strength efficiency than the static-coil dynamic-angle-spinning probe design.[6]

The probe head consists of a kel-F stator housing mounted between two supports on glass bearing races. A 7 mm zirconia stator from Doty Scientific is placed inside the housing, as shown in Fig. 6.15. The high pressure air enters the housing from the sides through the supports. The air from one side enters the rotor bearing cavity, while the air from the other side enters the rotor drive cavity. The two cavities are sealed by three o-rings. The rf coil wraps directly around the stator and exits the housing through copper pins which are then sealed by solder. The coil is connected to the rest of the rf circuit by strips of 0.05 mm beryllium copper shims. A pulley on one side of the housing is attached through kevlar strings to an identical pulley connected to a stepper motor mounted on the base of the probe. The watch-spring motion of the beryllium copper leads (Fig. 6.16) allows the rotation axis angle to be changed during the course of the experiment while maintaining a resonant circuit.

6.2.2 Variable Temperature Control

The temperature variability is obtained by heating the bearing and drive air, independently in glass Dewars built into the base of the probe. The air from the heaters is transferred through stainless-steel Dewared lines into the rotor housing. The temperature is monitored by a an Omega programmable temperature controller and a thermocouple placed

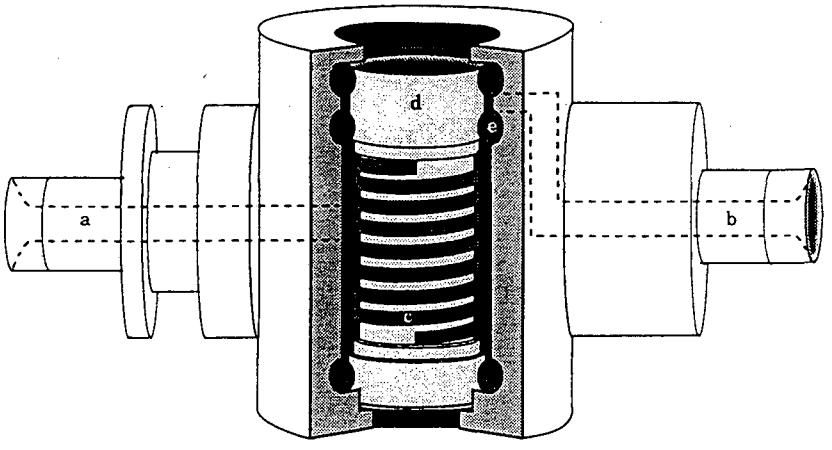

Figure 6.15. Cutaway view of the stator housing. (a) Bearing air channel (dotted hidden lines). (b) Drive air channel (dotted hidden lines). (c) rf coil, in bearing air cavity. (d) Stator. (e) O-rings separating bearing and drive air supplies.

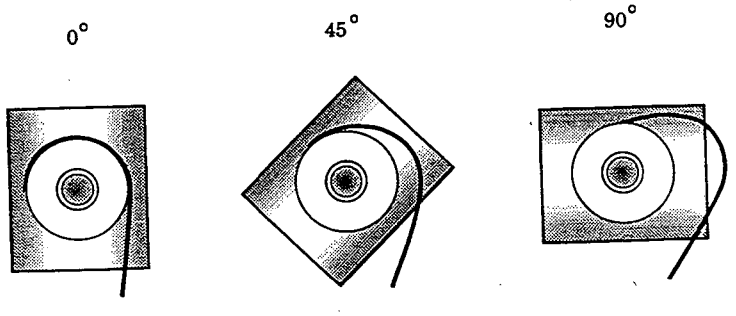

Figure 6.16. End-on view of the stator housing, showing the watch spinning-like motion of the beryllium copper leads when the angle between the spinning axis and the vertical is varied from 0° to 90°.

on the bearing line just before entry into the spinner assembly.

Due to the friction caused by the spinning rotor, the temperature read by the thermocouple is not identical to the sample temperature. The temperature calibration was obtained by recording a series of dimethylsulfone spectra with the sample spinning at 90° with respect to the static $\mathbf{B}_0$ field. Since the motions of dimethylsulfone and their dependence on temperature is well known,[7] comparisons of simulations and experiment allowed the temperature of the sample and the temperature read by the thermocouple to be related in °C as

$$T(\text{of sample}) = 2.5 + 1.20 * T(\text{of thermocouple}). \qquad (6.2)$$

6.2.3 Double Tuned Lumped Element Circuit

The double-tuned circuit used in the probe is based on the design by Doty *et al.*,[8] and is shown in Fig. 6.17. Polyflon NRP-VC-10-12-36A capacitors (10 turn, 1-10 pF, 1600V) are used for the tune and match on both the H and X sides of the circuit. A Voltronics V2102 capacitor is used in the trap circuit to filter out the H frequency signal on the X channel side.

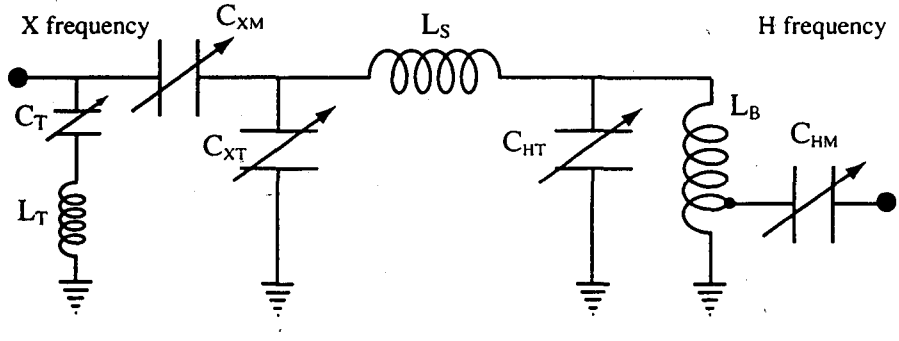

Figure 6.17. RF circuit for the double-tuned hopping-coil probe.

Since the rf coil moves with the stator housing, the rf pulse width scales as

$$p(\theta) = p(90^\circ)/\sin\theta \tag{6.3}$$

where $p(\theta)$ is the pulse width at an angle θ with respect to $\mathbf{B}_0$, and $p(90^\circ)$ is the pulse width at $\theta = 90^\circ$. In addition, the motion of the stator housing causes the beryllium copper leads attached to the capacitors to move which results in a tuning shift of the resonant circuit; however the shift can be reduced to less than ± 200 kHz in the range of $35^\circ \leq \theta \leq 90^\circ$ by adjusting the position of the leads.

6.3 Stepper Motor and Controller

The angle of the spinner axis is controlled by a Whedco stepper motor and computerized controller. A BEI optical encoder is used to feed back the position of the motor and correct for any errors in the motor steps.

The motor controller is operated by the pulse programmer in "stand alone" mode, which is enacted by setting the profile enable toggle to 1 (PE = 1). In this mode, pre-programmed commands contained in the profiles may be executed during the pulse sequence. The profiles may be read and executed in either the "non-encoded" or the "encoded" setting (note that the "encoded" setting is not related to the use of the optical encoder). In the non-encoded setting, one specified profile becomes activated and executed by a TTL pulse. In the encoded setting (used for all the VACSY experiments), up to 31 different profiles may be executed based on a 5 bit TTL input into profile lines 1 through 5. The TTL lines B3-B7 defined in the "Mot" icon line in the config.con file are connected to the profile lines 1-5 as:

Microword Bits	Profile Lines
B3	1
B4	2
B5	3
B6	4
B7	5
A2	6

A number, ranging from 0 to 31, designated in the "Mot" icon (or a gradient file defined for the "Mot" icon) is converted into a 5 bit binary number represented by the TTL lines B3-B7. The TTL lines then enable one of the 31 profiles. When a TTL pulse is sent to A2 (profile line 6), the motor controller executes the specified profile. Typically about 2 ms is required to set the 5 TTL profile lines and another 2 ms is required to execute the specified profile with a pulse on A2. Thus in order to use the motor controller in encoded mode, the pulse program should be written with the sequence of pulse events shown in Fig 6.18.

The resolution of the motor positioning is determined by the number of steps in the motor (typically 400 steps) and the fractional step sizes used by the controller. The fractional step sizes available range from 1 to 1/32 steps and are set by one of the dip switches shown in Table 6.4. The total number of motor steps in one motor revolution is

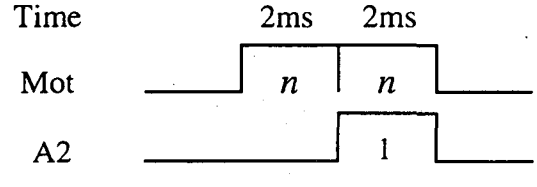

Figure 6.18. Pulse sequence events used to operate the motor controller in the "encoded" profiles mode. *n* is an integer from 0 to 31. The initial "Mot" pulse converts *n* to 5 bit logic and chooses the motor profile to execute. The second pulse executes the pulse with A2 executes the profile.

	switch number	switch setting	Switch Function
SW1	1	R	Fractional motor step sizes set to 1/32.
	2	L	
	3	R	
	4	R	Set to use the optical encoder feedback. In this setting the position of the motor is determined by the number of lines in the encoder and the encoder multiplier (SW2-9,10). This switch has no relation to SW2-8 and "encoded" profiles.
	5	L	Set to use maximum current (5A).
	6	L	
	7	L	
	8	L	
SW2	1	L	Motor unit address labeled as "0". May be set to a different number up to "7" if more than one motor controller is used.
	2	L	
	3	L	
	4	R	Motor controller set as "master".
	5	R	Echo command mode.
	6	L	Baud rate = 1200.
	7	R	Serial port set as RS232C.
	8	R	Controller used in "encoded" profile mode. This switch has no relation to the optical encoder and SW1-4.
	9	L	Optical encoder step multiplier set to 4.
	10	R	

Table 6.4. Dip switch settings for the Whedco motor controller used in the VACSY experiments.

$$\text{Total Motor Steps} = \frac{(\text{number of steps in motor})}{(\text{fractional step size})}. \tag{6.4}$$

For example, a 400 step motor using 1/32 step sizes will give a motor position resolution of 0.0281° per motor step.

When an optical encoder is used, the motor still moves with the defined motor steps in Eq. 6.4, but the controller will determine the motor position by increments of the optical encoder. The resolution of the encoder steps is determined by the number of lines in the encoder (typically 1024) and the encoder multiplier value. The multiplier can take on

motor par.	par. setting	Parameter Function
ER	6400	Ecoder ratio set according to Eq. 4 for a 400 step motor and 1024 line encoder.
PE	1	Profile enable. Allows the motor controller to run in"stand alone" mode.
PC	1	Position correction. Allows motor controller to use encoder feedback to corrects its position.
DF	0	Deadband Fault. Faults the motor on position error. Set to 0 to allow for position correction.
CT	1-10	Correction time. Time delay before each position correction in units of milliseconds.
SS	100	Parameters controlling the motion of the motor: start-stop speed, speed, and acceleration, in units of motor pulses/second. There parameters must be set to higher values for hopping experiments.
SP	500	
AC	100	

Table 6.5. Some of the motor control constants and motor parameters used in the VACSY experiments.

values of 1, 2, and 4 and are set by dip switches shown in Table 6.4. The total number of encoder steps in one motor revolution is

$$\text{Total Encoder Steps} = \begin{pmatrix}\text{number of lines in} \\ \text{the optical encoder}\end{pmatrix} \times (\text{encoder multiplier}) \qquad (6.5)$$

For example, a 1024 line encoder with a multiplier of 4 will have a motor position resolution of 0.0879° per encoder step.

The motor controller requires a parameter, the encoder ratio (ER), to be set in order to determine the relative resolution of the motor and encoder steps. ER is defined as

$$\text{ER} = \frac{\text{Total Motor Steps}}{\text{Total Encoder Steps}} \times 4096. \qquad (6.6)$$

If the optical encoder is used, and $\text{ER} < 4096$, the encoder resolution exceeds the motor position accuracy, and the motor controller will detect errors when an encoder position is called for that is not accessible by the motor. This can be avoided by making sure that the

multipliers and fractional step sizes are set such that $ER \geq 4096$. If the optical encoder is not used, $ER = 4096$.

Typical dip switch settings and the corresponding motor controller parameters are shown in Table 6.4 and 6.5.

References

1. D. N. Shykind, G. C. Chingas, A. Pines, and A. J. Shaka, Rev. Sci. Instrum., **61**, 1474 (1990).

2. U. Haubenreisser, and B. Schnabel, J. Magn. Reson., **35**, 175 (1979).

3. M. E. Rosen, NMR Studies of Molecules in Liquid Crystals and Graphite, University of California, Berkeley, 1992.

4. S. P. Rucker, Two-Dimensional Nuclear Magnetic Resonance Studies of Molecular Structure in Liquid Crystals, University of California, Berkeley, 1991.

5. M. A. Eastman, P. J. Grandinetti, Y. K. Lee, and A. Pines, J. Magn. Reson., **98**, 333 (1992).

6. K. T. Mueller, G. C. Chingas, and A. Pines, Rev. Sci. Instrum., **62**, 1445 (1991).

7. M. S. Solum, K. W. Zilm, J. Michl, and D. M. Grant, J. Phys. Chem., **87**, 2940 (1983).

8. F. D. Doty, R. R. Inners, and P. D. Ellis, J. Magn. Reson., **43**, 399 (1981).

LAWRENCE BERKELEY LABORATORY
UNIVERSITY OF CALIFORNIA
TECHNICAL INFORMATION DEPARTMENT
BERKELEY, CALIFORNIA 94720